Exploring potential of halide perovskite materials in solar cells and thermoelectric devices

プレブオチル, バダムガラブ

2024

Doctoral thesis

Exploring potential of halide perovskite materials in solar cells and thermoelectric devices

Badamgarav Purev–Ochir

Department of Applied Chemistry

Graduate School of Engineering

Kyushu University

Contents

CHAPTER 1

General Introduction

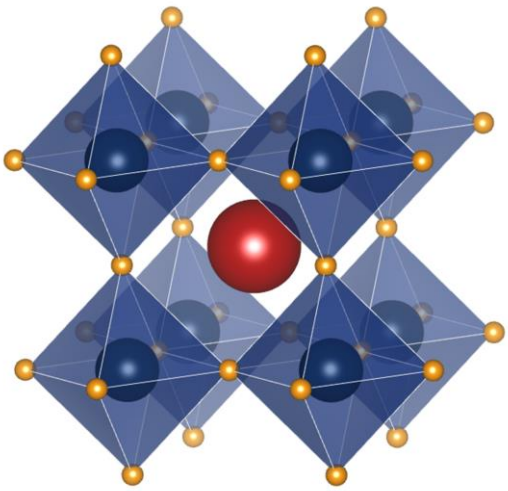

Chapter 1: General Introduction

1.1 Perovskite Materials

1.1.1 Definition and Structure of Perovskite

The perovskite material was first found as a naturally occurring mineral of calcium titanate ($CaTiO_3$) in the Ural Mountains of Russia by Russian mineralogist Count Lev Perovski in the nineteenth century. Following his discovery, German mineralogist Gustav Rose demonstrated that this mineral had a three–dimensional (3D) crystal structure and named it as "perovskite" after the mineralogist Count Lev Perovski.[1] Today the word "perovskite" is a general term to describe a wide variety of materials with a general repeated structure of ABX_3. As for the perovskite materials, the general structure is shown in **Figure 1–1a**, each unit cell consists of five atoms. The metal cation *B* occupies the central position, while cation *A* is situated at the corners. Additionally, six anions *X* shaping the corners of an octahedron are positioned at the center of six planes within the unit cell. Perovskite structures can accommodate various cations and anions, leading to tunable electronic and optical properties crucial for diverse functionalities.[2] In nature, perovskites are mainly oxides, but they can also appear as fluorides, chlorides, hydroxides, arsenides, and intermetallic compounds.[3] Synthetic perovskites cover a wide range of elemental compositions, from metallic to hybrid organic––inorganic, metal–free, and even noble gas–based varieties. This versatility makes perovskite one of the most adaptable crystal lattices.[4] Among the different types of perovskites, halide perovskites (HPs), which consist of heavier halides (I, Br, and Cl), have been identified as one of the most promising materials in high–performance electronic and optoelectronic applications. **Figure 1–1b** shows the typical elements occupying the different positions in the structure of HPs.

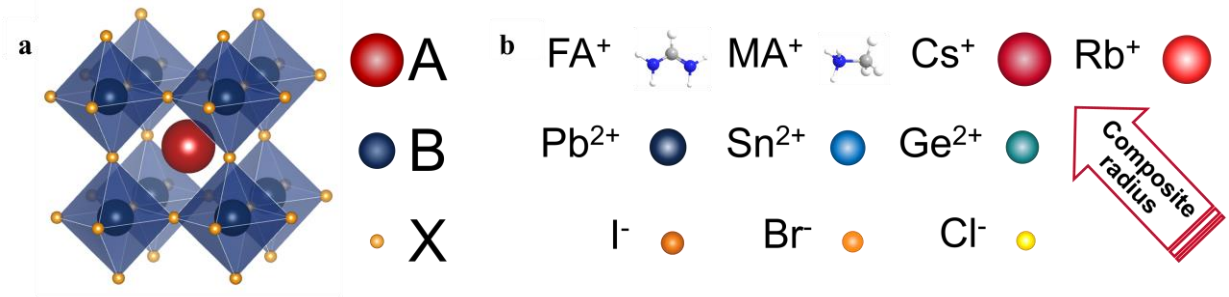

Figure 1-1. (a) The crystalline structure of ABX_3 perovskite and (b) typical elements occupying the different positions in the structure in the structure of HPs. FA and MA stand for formamidinium and methylammonium, respectively.

In organic–inorganic hybrid HPs, the *A*–site is the organic cation (such as $–MA^+$, $–FA^+$); the *B*–site is the metallic cation (such as Pb^{2+}, Sn^{2+}, Ge^{2+}); *X*–site is the halogen (such as $I^–$, $Br^–$, $Cl^–$). Depending on the compositions, properties, and structures of perovskites can be tuned.[2] Moreover, several crystal phases of perovskites, such as tetragonal, orthorhombic, trigonal, and cubic polymorphs, have been discovered. Phase transitions between the polymorphs take place and properties depending on the temperature and environment.[5,6] MA–based lead triiodide ($MAPbI_3$), which is the simplest composition of the organic–inorganic hybrid HPs adopts different structures upon heating (Table 1–1). The $MAPbI_3$ perovskite is orthorhombic below 161 K, tetragonal from 161 to 330 K, and cubic above 330 K.[6] According to Poglitsch and Weber, space groups relevant to perovskite materials include:[7]

- Orthorhombic: *Pbnm*
- Tetragonal: *I4/mcm*
- Cubic: *Pm–3m*

Table 1–1. Structural phase transitions of $MAPbI_3$.[5]

Structural transition	Transition Temperature (K)	
	Heating	Cooling
Pm–3m → I4/mcm	338	338
I4/mcm → Pnma	–	160–165

Substituting MA cations with different cations such as Cs^+, FA^+, or a combination of cations, can lead to different structures and properties. Even a layered structure can be formed instead of the 3D structure with bigger cations (ethylammonium–EA^+, butylammonium–BA^+, guanidinium–GA^+). The size of *A* and *B*–site cations greatly influence the structure of perovskite crystal lattice and their radii correlation is determined by the Goldschmidt tolerance factor (*t*), defined as equation 1–1:

$$t = \frac{r_A r_x}{\sqrt{2(r_B + r_x)}} \qquad (1–1)$$

where r_A and r_B are the ionic radii of the *A* and *B*–site cations respectively and, r_x is the ionic radius of the anion. The *t* value determines if the *A*–site cation fits in the cavities of the BX_3 framework. Perovskites typically exhibit *t* values ranging from 0.8 to 1. This range indicates the degree of distortion from the ideal 3D cubic structure, with values closer to 1 presenting less distortion. The distorted perovskites can be found between 0.8–0.9 due to the tilting of the BX_6 octahedra and resulting reduction in symmetry.[8–10] Deviating below a tolerance factor of 0.8 may lead to

excessive distortion, compromising the perovskite's structural integrity. Conversely, approaching a tolerance factor of 1.1 results in an *A*–site cation that is too large, and thus perovskite structures cannot be formed. On the other hand, 3D perovskite structures are split into lower–dimensional perovskite structures, such as two–dimensional (2D) and quasi–2D perovskites by engineering the composition.

1.1.2 Historical Development in Perovskite Materials

Early investigations of perovskites focused on the understanding of their structural and biaxial optical properties, particularly within titanate–based compounds.[11] Initially, these materials found practical applications as pigments in paints and coatings, serving the needs of various industries.[12] In the 1940s, the urgent military and industrial need for ferroelectrics with high dielectric constants led to the discovery of $BaTiO_3$ ceramics, which sparked widespread interest in the electronic properties of perovskites.[13,14] Shortly thereafter, the introduction of $CsPbX_3$ compounds, renowned for their vibrant colors, marked a significant milestone, enticing investigations into the electronic behaviors of HPs.[15] These studies unveiled intriguing frequency–dependent photoconductive responses, shedding light on the potential of HPs for optoelectronic applications. Concurrently, attention was drawn towards the unique characteristics of 2D variants, encompassing perovskite families such as A_2BX_4, $A_3B_2X_7$, and $A_4B_3X_{10}$.[16] These compounds featured layered inorganic sheets interspersed with monovalent organic or inorganic *A*–site cations, eliciting curiosity due to their compelling ferro– and antiferromagnetic properties. Consequently, significant efforts were dedicated to unraveling the underlying structural intricacies of these 2D perovskites, driving forward the understanding of their potential applications.[17,18]

The early research on ferroelectric ceramics laid the groundwork for a wide array of pioneering perovskite–based technologies and materials, spanning from barrier layer capacitors to high–temperature superconductors, high–response piezo–electrics, proton conductors, fuel cells, memory storage devices, colossal magneto–resistors, and most remarkably, organometal halides for photovoltaic (PV) applications.[19–24]

1.1.3 Properties of Halide Perovskite Materials

HPs constitute a large and complex material system that offers a diverse range of material properties, morphologies, and synthesis methods.[25] This extensive variety enables tailored design and optimization to suit specific applications across multiple fields such as solar cells, light–

emitting diodes, photodetectors, and lasers.[26] In addition to optoelectronic applications, perovskites also show great potential in thermoelectric (TE) applications with ultralow thermal conductivity (κ) and high Seebeck coefficient (S).[27,28]

HP structures can accommodate various cations and anions, leading to tunable electronic and optical properties, which are crucial for diverse functionalities.[29–31] Furthermore, their versatile morphologies, ranging from thin films to nanostructures, offer flexibility in device fabrication and integration.[26] Additionally, perovskite synthesis routes encompass a variety of techniques, including solution processing, vapor deposition, and solid–state reactions, allowing for precise control over material composition, crystallinity, and defect engineering.[32,33]

Properties critical for optoelectronic applications, including excited state lifetime, recombination mechanisms, mobility, and intrinsic carrier concentration, can often be elucidated through comprehension of a material's band structure and density of states (DOS). Fundamentally, the diverse array of HPs provides an advantageous platform for systematically investigating the impacts of dimensionality, composition, and structural disorder on underlying electronic configurations. HPs, particularly those based on Sn and Pb, exhibit a myriad of distinctive electronic characteristics that set them apart from conventional semiconductors.[25,29]

HPs serve as pivotal materials in optoelectronics, being direct gap semiconductors characterized by robust band–edge optical absorption and luminescence. Specifically, their valence band (VB) maximum and conduction band (CB) minimum coincide in reciprocal space (k–space). The electronic structure near the band edge is predominantly determined by the fundamental BX_6 building blocks.[34–36] Therefore, orbital diagrams of isolated $[BX_6]_4^-$ clusters, akin to those found in the 0D perovskite analog $(CH_3NH_3)_4[PbI_6]\cdot 2H_2O$, establish a basis for comprehending more intricate band structures in higher dimensionality structures. Notably, for $[PbI_6]_4^-$ clusters, the VB originates from the σ–antibonding orbital composed of Pb 6s−I 5p, while the CB is formed by π–antibonding and σ–antibonding orbitals of Pb 6p−I 5p and Pb 6p−I 5s, respectively (**Figure 1–2**).[37]

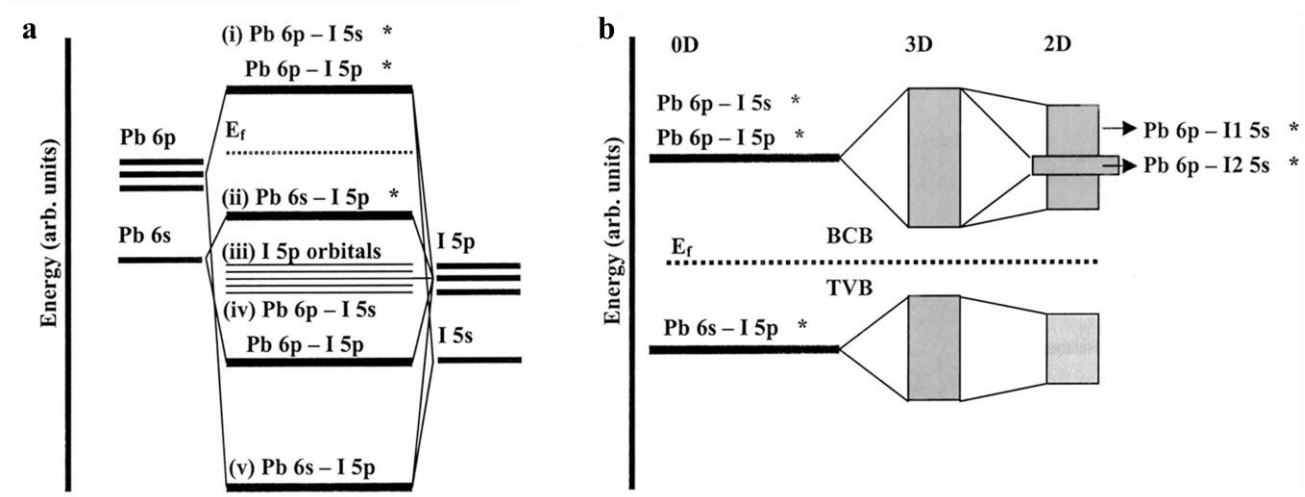

Figure 1–2. Bonding diagram of (a) $[PbI_6]^{-4}$ cluster (0D), (b) 3D crystal $CH_3NH_3PbI_3$, and (b) 2D crystal $(C_4H_9NH_3)_2PbI_4$ at the top of the VB and the bottom of the CB. Reproduced from Ref. [37]

The band gap of HPs is notably influenced by the composition of the anion (*X*–site), whereas the cation at the *A*–site plays no role in dictating the electronic structure. Among a homologous series of compounds, the band gap tends to follow the sequence Cl > Br > I.[29,30] The primary effect of halide substitution lies in modulating the upper VB due to the substantial contribution of halide p orbitals at these energy levels. Conversely, the lower CB remains relatively insensitive to changes in anion chemistry, exhibiting predominantly nonbonding character. $CsSnCl_3$ demonstrates the widest band gap compared to $CsSnBr_3$ and $CsSnI_3$, attributed to the lower–lying halide p orbitals comprising the antibonding upper VB. In contrast, the conduction band exhibits similar characteristics across all three compounds.[29]

A prominent characteristic of 3D HPs is their relatively high absorption coefficient (α), a factor contributing to the efficient generation of photocurrent using thin films of compounds such as $MAPbI_3$ and $FAPbI_3$.[38–40] The intense optical absorption observed in these materials, in addition to their direct gap nature, originates from the halide−−p → metal−−p transition at the band edge. The relatively large joint density of states (JDOS) near the fundamental electronic absorption edge in HPs is attributed to the less dispersive nature of p orbitals compared to s orbitals.[25] Calculations conducted by Yin *et al*. suggest that $MAPbI_3$ and GaAs exhibit similar transition matrices. However, the CB of GaAs comprises cation s orbitals, resulting in a lower DOS compared to $MAPbI_3$ (and $CsSnI_3$) primarily at the CB as shown in **Figure 1–3a**. The full JDOS from this analysis also indicates a significantly higher DOS in the HPs (**Figure 1–3b**).[25] Examining literature reports, the reported band edge α values for $MAPbI_3$ exhibit considerable

variability, ranging over nearly an order of magnitude from ~6 × 10^3 to ~4.5 × 10^5 cm^{-1} over the visible light spectrum.[25,39–42]

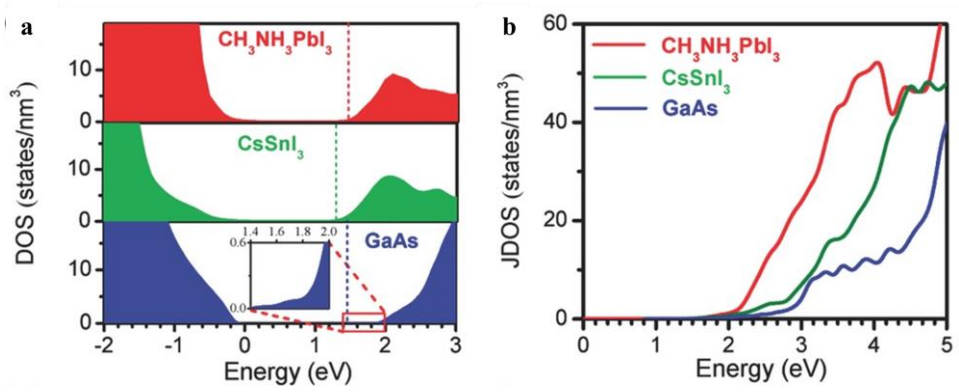

Figure 1–3. (a) Comparison of the DOS and (b) calculated JDOS of $MAPbI_3$, $CsSnI_3$, and GaAs.[25]

HPs showcase remarkable electronic properties despite their solution–based fabrication process; however, ongoing advancements in fabrication techniques continually enhance these properties by altering the synthesis process or through exposure to elevated temperatures.[25,43]

Determining how charge moves in these materials and how changes in material processing and component substitution affect them is important to improving their charge transport properties. Diffusion of charges occurs depending on diffusion length which is related to charge mobility. The long diffusion length is particularly important for PV materials, as it stands as a key parameter for efficient photocarrier collection, essential for maximizing solar energy conversion. The diffusion length can be estimated with a combination of carrier lifetime and mobility.[44] This method is particularly useful when a direct measurement of the diffusion length is difficult. The decay of photoluminescence (PL) is used to determine the carrier lifetime.

The Drude model, simplification of charge transport, posits that high carrier mobility stems from low scattering and low effective masses.[45] However, deviations from this model can occur under conditions such as high charge densities, where electron−hole scattering becomes significant, the presence of strong electron−phonon interactions (small polarons), or charge hopping phenomena, among others.[46] In terms of HPs, these consequences can be manifested in decreased mobility due to doping, which introduces more scattering centers.[47]

Perovskites also exhibit high charge mobility of tens of $cm^2\ V^{-1}\ s^{-1}$ [48], related to the ionicity of the metal–halide bond, enabling carrier diffusion lengths of up to the micrometer range[49]. Moreover, its exciton binding energy is only around 10 meV, facilitating easy separation of excitons into free charges even at room temperature.[50]

The structural qualities of the perovskites are reflected in their charge–transport properties due to the orbital overlap. Especially, the distorted *B*–*X* bond angle plays a crucial role in charge transport, where deviations in octahedral tilting and orbital overlap can lead to decreased conductivity. Yamada *et al*. demonstrated this phenomenon in the series $CsSnBr_3$, $MASnBr_3$, $MASn_{1-x}Pb_xBr_3$, and $MAPbBr_3$, revealing a decrease in conductivity with altered bond angles.[31] Similarly, Hao *et al*. observed a similar trend in $MASn_{1-x}Pb_xI_3$ alloys, with conductivity peaking in pure $MASnI_3$. In $MASnI_3$, the Sn−I−Sn bond approaches the largest tilting angle, but this angle decreases with increasing Pb content, inducing a distortion in the *B*−I−*B* bond and subsequently reducing conductivity as shown in **Figure 1–5**. Furthermore, the conductivity variations during temperature–induced phase changes, as seen in $CsSnI_3$, suggest a close relationship between perovskite phase conductivity and the linear *X*−*B*−*X*−*B* chain. Thus, under equivalent conditions, conductivity is maximized in the cubic ($Pm\bar{3}m$) phase, where the *B*−*X*−*B* bond angle is 180°.[51]

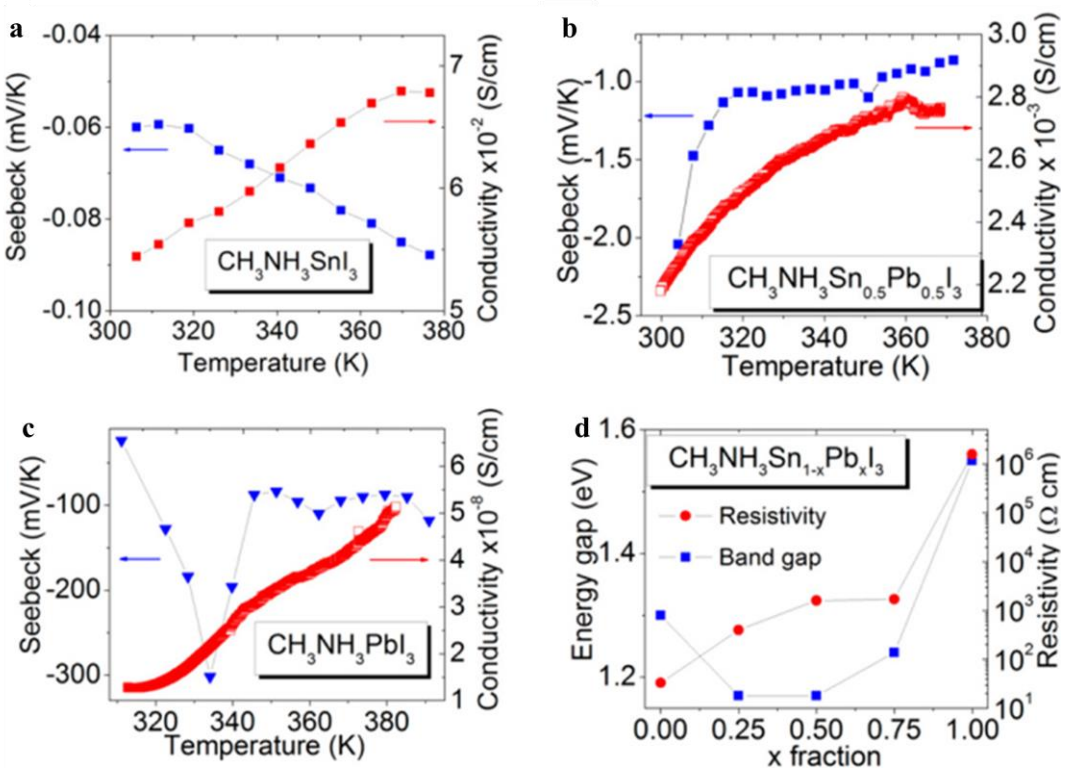

Figure 1–5. Conductivity and Seebeck measurement results as a function of temperature for (a) $MASnI_3$, (b) $MASn_{0.5}Pb_{0.5}I_3$, and (c) $MASnI_3$ samples prepared from solution. (d) Resistivity and optical band gap as a function of composition (*x*) in $MASn_{1-x}Pb_xI_3$ solid solutions.[51]

Furthermore, conductivity increases as HPs more closely resemble a 3D structure, enhancing the mobility of charge carriers. Generally, the electronic properties of organic-inorganic HPs depend largely on the inorganic component, as π–conjugated organic compounds typically exhibit edge–to–face interactions, resulting in limited electronic overlap. HPs with a 0D structure

exhibit noticeably lower conductivity compared to their 1D, 2D, and 3D counterparts, primarily due to the absence of an extended inorganic network. In 1D perovskites, the reduced structure leads to an increase in the density of states at certain energy levels, resulting in improved conductivity.[52] Despite the increased availability of carriers, actual conductivity is hindered by narrow conduction bands, limiting their mobility. Conversely, the structures of 2D and 3D perovskites offer wider bands, thereby enhancing conductivity. Chung *et al*. investigated the electrical conductivity (σ) of $CsSnI_3$, observing the effect of tin vacancies (V_{Sn}) within the crystal structure.[53] Intrinsic defects within the structure of this perovskite enable the generation of holes with high mobility, especially at elevated temperatures, effectively transforming the perovskite into a p–type metal and greatly enhancing σ.

1.2 Perovskite Solar Cells

HP materials were indeed first employed as the light–absorbing layer in solar cells by Professor Tsutomu Miyazaki in 2009, having the power conversion efficiency (PCE) of 3.8 %.[54] This breakthrough marked a significant advancement in PV technology, paving the way for the rapid development and widespread adoption of perovskite solar cells (PSCs). Since then, extensive research efforts have been devoted to enhancing the efficiency, stability, and scalability of PSCs, with notable achievements in improving PCEs. Today, PCSs are emerging as the most promising candidates for next–generation PV technology and have attracted significant interest in both academia and industry.[55,56] In a very short period of time, PSCs have achieved the PCE to the current world record of 26.1 % in 2023 (**Figure 1–6**).[57] Such high PCE from PSCs is due to the combination of their excellent characteristics, such as long charge carrier diffusion length[41,58], high absorption coefficient[59], suitable bandgap[60,61], and low exciton binding energy[42,62]. In addition, the cost of perovskite–based PV technology is believed to be lower than that of silicon solar cells thanks to their solution processability and low–cost starting materials, providing a great capability for commercialization.[63]

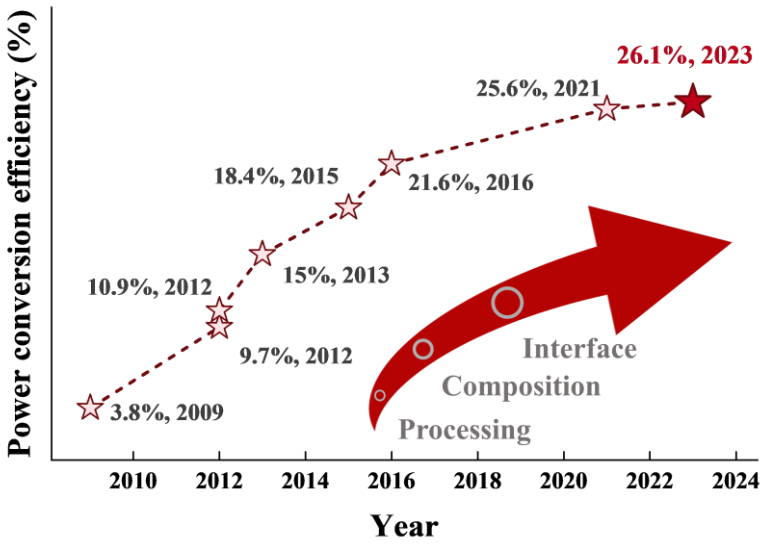

Figure 1–6. Progress of power conversion efficiency in PSCs according to Best Research–Cell Efficiency chart from National Renewable Energy Laboratory.[64]

1.2.1 Working Principles of Perovskite Solar Cells

PSCs operate on the principle of converting sunlight into electricity through the PV effect as shown in **Figure 1–7**. The basic working principle involves the following key steps:

- Light Absorption: Perovskite materials absorb photons from sunlight, exciting electrons from the VB to the CB, creating electron–hole pairs (excitons).
- Charge Separation: Once generated, the electron–hole pairs separate due to the built–in electric field within the device structure and very low exciton binding energy. Electrons move toward the electron transport layer (ETL), while holes migrate to the hole transport layer (HTL).
- Charge Collection: Electrons are collected at the ETL, typically made of materials like titanium dioxide (TiO_2) or metal oxides, and transported through an external circuit to generate electrical current. Meanwhile, holes are collected at the HTL and transported to complete the circuit.
- Charge Recombination: To maintain high efficiency, minimizing electron–hole recombination is crucial. Surface passivation layers and interfacial engineering techniques are employed to reduce recombination losses.

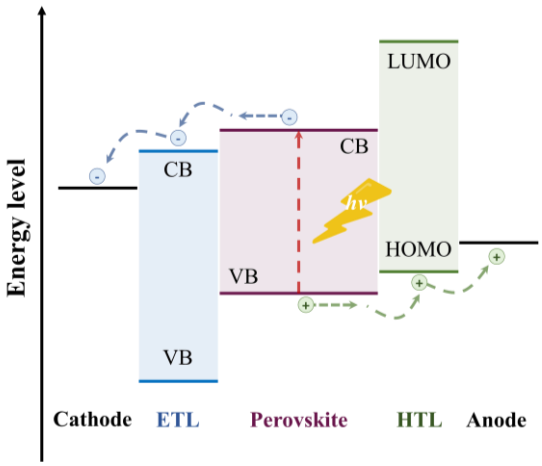

Figure 1–7. Scheme of the basic mechanism in a PSC. HOMO and LUMO stand for highest occupied molecular orbital and lowest unoccupied molecular orbital, respectively.

To ensure efficient power output, it is crucial for the band gap of the perovskite absorber to effectively absorb visible light. Ideally, the optimal band gap for a single junction solar cell is within the range of 1.1–1.4 eV. Moreover, the CB of the perovskite absorber should be slightly shallower than the CB of the ETL, facilitating the favorable transfer of photoexcited electrons. Similarly, maintaining the VB of the perovskite layer slightly deeper than that of the hole conductor promotes efficient hopping of holes.

To assess the efficiency of PSCs, a standardized light source is employed for irradiating the solar cell. The light source is typically calibrated to simulate the air mass 1.5 global (AM1.5G) condition, featuring an intensity of 100 mW cm^{-2}. The AM1.5G spectrum is defined as light reaching the surface of the earth at a zenith angle of 48.2°C and it encompasses direct and diffuse light components only. When scanning the voltage under illumination with the solar simulator, a plot of the current density–voltage (*J–V)* is obtained as in **Figure 1–8**. The output powers (*P*) of PSCs can be calculated from the *J–V* measurement (**Figure 1–8**).

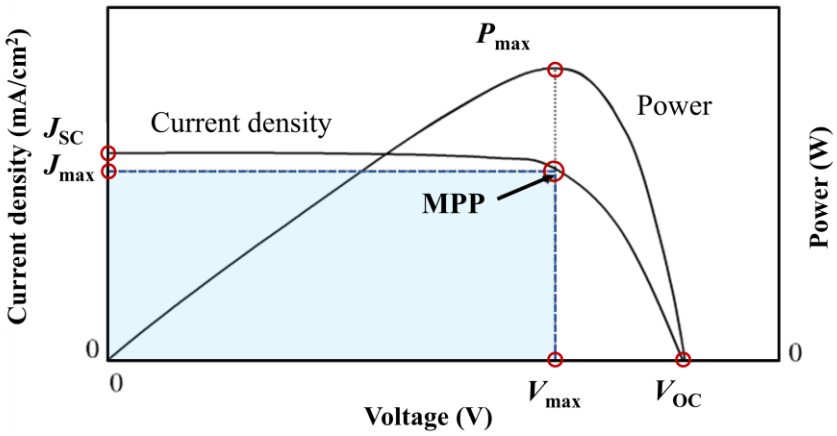

Figure 1–8. *J–V* and *P–V* curves of PSCs.

The short–circuit current density (J_{SC}) is the maximum photo–generated current that can be achieved. It is the point where no voltage is applied between the anode and the cathode. The open-circuit voltage (V_{OC}) indicates the generated voltage at the open-circuit condition (zero current). At a defined point known as the maximum power point (MPP), a solar cell reaches its maximum output power (P_{max}). This occurs at the position on the *J–V* curve where the product of current density (J_{max}) and voltage (V_{max}) is maximized. The fill factor (FF) describes the ideality of a solar cell, indicating how closely the *J–V* curve resembles a rectangle, as illustrated in **Figure 1–8**. This parameter can be expressed by **Equation 1–2**:

$$\mathrm{FF} = \frac{J_{\mathrm{max}}\, V_{\mathrm{max}}}{J_{\mathrm{SC}}\, V_{\mathrm{OC}}} \tag{1–2}$$

The PCE determines the performance of a solar cell, which is the ratio between the output and input power, P_{out} and P_{in} respectively. It can be calculated by Equation 1–3

$$\mathrm{PCE} = \frac{P_{\mathrm{max}}}{P_{\mathrm{in}}} = \frac{J_{\mathrm{max}}\, V_{\mathrm{max}}}{P_{\mathrm{in}}} = \frac{J_{\mathrm{SC}}\, V_{\mathrm{OC}}\, \mathrm{FF}}{P_{\mathrm{in}}} \tag{1–3}$$

1.2.2 Device Architecture

In general terms, the perovskite material is sandwiched between two electrodes, one of which is transparent, to allow the light to pass through and reach the perovskite absorber layer. The HTL and ETL are commonly introduced between the perovskite layer and the electrodes. The device architecture of PSCs can be divided into three major groups (see **Figure 1-9**):

i. Mesoporous n-i-p heterojunction (hereafter abbreviated as “meso”), where the perovskite layer is deposited on top of the mesoporous oxide ETL.
ii. Planar n-i-p heterojunction (hereafter abbreviated as “planar”), where the perovskite layer is deposited on top of the compact oxide ETL.
iii. p-i-n heterojunction (hereafter abbreviated as “inverted”), where the perovskite layer is deposited on top of the HTL.

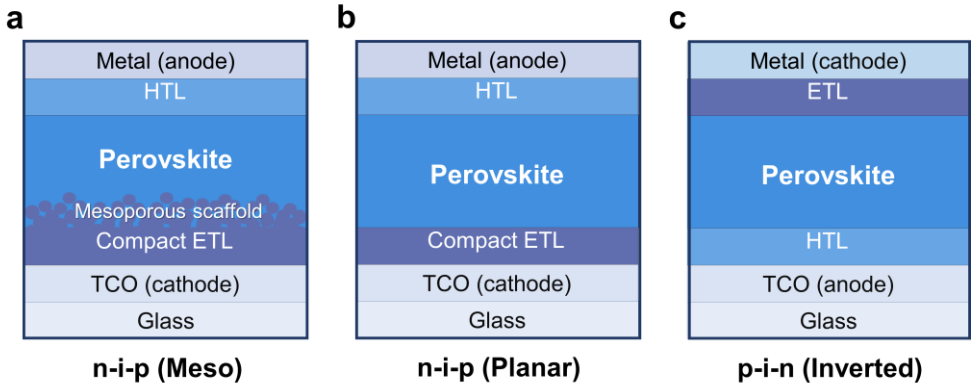

Figure 1–9. PSCs with (a) meso, (b) planar, and (c) inverted structures.

The mesostructure was one of the early structure types developed for PSCs (see **Figure 1–9a**). It adapted the architecture of dye–sensitized solar cells (DSSCs) by replacing the light–harvesting dye with lead halide perovskite semiconductors.[54] The mesoporous scaffold plays a pivotal role in this structure by providing a large surface area for the deposition of the perovskite absorber layer. This configuration facilitates efficient electron extraction and transport, contributing to enhanced device performance. In PV materials, a long diffusion length is critical for effective photocarrier collection. Additionally, a sufficiently thick (>300 nm) absorber layer is necessary to effectively absorb incoming light.[65] While the diffusion length of typical perovskite materials was around 100 nm[62], the mesostructure demonstrated sufficient electron extraction even with a relatively short diffusion length compared to the film thickness. However, subsequent advancements in PSCs have led to the development of alternative structures without the need for a mesoporous scaffold.

The planar architecture is an evolution of the mesoscopic structure, featuring the perovskite layer sandwiched between the ETL and the HTL (see **Figure 1-9b**). This structure could be fabricated with a low–temperature process, unlike the mesoporous structure which requires high–temperature sintering processing at ~500˚C for TiO_2, resulting in a simpler overall configuration.[66] The high efficiency can still be achieved without the mesoporous layer through precise control of the interfaces between the different layers constituting the PSCs. By optimizing these interfaces, efficient charge extraction and transport can be realized.[67] Furthermore, advancements in compositional engineering have enabled perovskite materials to achieve longer carrier diffusion lengths, reaching up to 1 μm.[58] This extended diffusion length enhances the ability of charge carriers to travel through the material without recombination, thereby improving overall device efficiency and performance.

The inverted structure originated from the organic solar cell, where the HTL is deposited first followed by the perovskite layer and the ETL (see **Figure 1-9c**).[68] In this structure, the traditional organic transport layers such as poly(3,4–ethylenedioxythiophene):poly(styrenesulfonic acid) (PEDOT:PSS) and fullerene derivative were directly adopted as the HTL and ETL, respectively.[69] A significant discovery in perovskite research revealed that perovskite materials are proficient in transporting holes themselves. Jeng *et al*. developed the first planar heterojunction PSC with an inverted structural design.[70] This breakthrough led to the adoption of the inverted p–i–n configuration, expanding the range of options for selective layers from organic to inorganic materials.[71] Furthermore, the utilization of oxide HTLs enabled the construction of mesoscopic p–i–n device architectures, further diversifying the design possibilities.

1.2.3 Development of Perovskite Solar Cells

Since the inception of PSCs, various methods have been explored to enhance their performance and stability. The first PSCs perovskite-sensitized TiO_2 solar cells were fabricated using liquid electrolytes based on iodide or bromide solutions ($MAPbBr_3$ and $MAPbI_3$), resulting in a very low efficiency of 3.8 %.[54] In a later study, the electrolyte-based HTL was replaced by a solid-state material of 2,2′,7,7′-tetrakis(*N*,*N*-di-*p*-methoxyphenylamine)-9,9′-spirobi-fluorene (spiro–MeOTAD), leading to a PCE of 10 %.[72] Moreover, substituting the conducting material (TiO_2) with nonconducting material (Al_2O_3) in the nanoporous layer led to an enhancement in the open-circuit voltage of PSCs, resulting in an increased PCE.[73] Furthermore, the performance of PSC devices was improved with $MAPbI_{3-x}Br_x$ mixed halide perovskites. Specifically, efficiency increased with lower concentrations of Br, while higher concentrations resulted in perovskite films exhibiting improved stability against humidity.[74] Furthermore, in pursuit of the ideal bandgap of 1.34 eV according to the Shockley–Queisser limit, perovskite compositions have evolved from the initial $MAPbI_3$ to double-cation FAMA or FACs and triple-cation CsMAFA–based perovskites. Among them, $Cs_{0.05}(FA_{1-x}MA_x)_{0.95}Pb(I_{1-y}Br_y)_3$ have shown to have excellent PCEs with high reproducibility.[75] Therefore, I used the CsMAFA–based perovskite for the fabrication of PSCs in this study.

Besides designing the composition of perovskite material, enhancing the conductivity and hole mobility of the pristine spiro–OMeTAD HTL has proven pivotal in improving the performance of PSCs. Chemical dopants or additives, such as bis(trifluoromethane)–sulfonimide

lithium (LiTFSI) and 4–tert–butylpyridine (4–tBP), are commonly employed to boost hole conductivity and induce an energy level shift in the spiro–OMeTAD HTL, consequently leading to enhanced efficiency of PSCs. [76–78]

Furthermore, interface engineering methods have emerged as one of the most important strategies for pushing PSC performance to its limit. Various types of interlayers have been introduced at the interface of electrode/ETL, ETL/perovskite, perovskite/HTL, or HTL/electrode to improve the device's performance.[79] For example, Cr or Al_2O_3 has been used as the interlayer between the HTL and the back electrode to enhance the performance of PSCs.[80,81] Moreover, optimizing interfacial contacts by employing ionic liquids to lower roughness or align the surface work function[82,83] and improving the adhesion of functional layers[84] are important ways to promote charge extraction. Generally, it is common to accelerate the interface carrier injection and transportation by passivating the surface defects to minimize carrier recombination or tailoring the Fermi level (E_F) to shift the HOMO of the HTL or the conduction band of the ETL.[84,85]

1.2.4 Challenges of Perovskite Solar Cells

Over the last decade, improving both the efficiency and durability of PSCs has been achieved by optimizing fabrication processes and device architectures of PSCs; improving compositions of the perovskite absorber and charge transport layers, and modifying the interfaces.[67,86–89] However, despite the rapid development of PSCs, some serious obstacles still limit their commercialization.[90,91] PCEs and the operational durability of PSCs are significantly influenced by conditions of the perovskite layer, ETL, HTL, electrodes, and their interfaces.

The instability of PSCs is influenced by numerous conditions: illumination[92,93], heat[94], moisture[95,96], oxygen[97–99], and electrical biasing[100]. In particular, numerous studies have highlighted that perovskites decompose under operational conditions, especially for long-duration use in air, resulting in decreased performance of PSCs.[101].[91,102] The degradation of a perovskite material is initiated by the generation of gaseous and solid byproducts when devices are exposed to ambient conditions. The MA–based perovskite decomposes in the presence of water molecules, causing the formation of methylamine and hydroiodic acid, which further decompose into gaseous products, such as H_2 and I_2.[103–105]. Additionally, degradation associated with oxygen in air has been reported in PSCs with the spiro-OMeTAD HTL, attributed to factors such as the oxidation of spiro-OMeTAD, as well as the presence of pinholes in the spin-coated spiro-OMeTAD layer.[76–78] The combination of LiTFSI and molecular oxygen in air, which is used to induce the oxidation

of spiro–OMeTAD, leads to a negative impact on the long–term durability of PSCs.[106] Additionally, the doped spiro–OMeTAD film prepared by a standard spin–coating method has a high density of pinholes, forming channels for the diffusion of gas molecules from ambient air (e.g., H_2O and O_2) into the perovskite layer.[107] Therefore, the formation of pinholes in the spiro–OMeTAD HTL is also a possible reason for the degradation of the perovskite material.[108,109] However, an understanding of the fundamental reasons behind degradation is still required to be clarified in the spiro-OMeTAD HTL and the perovskite light absorber.

Moreover, there are a number of unknown challenges impeding PCEs, posing obstacles before PSC products are ready to launch. For metal oxide charge transport and perovskite layers, the ion vacancies are easily formed at their surfaces, resulting in defect accumulation at the interfaces with the contacts. These interface defects induce the formation of trap states inside the bandgap of materials, which causes severe nonradiative recombination of photo–generated charge carriers, limiting overall PV performance.[110–112] Additionally, energy–level mismatch and accumulated charges at interfaces influence PCEs of PSCs, and the migration of ionic species from decomposed perovskites into other layers is a major hindrance.[85,112,113] Furthermore, metal migrating into the perovskite layer has been observed previously in aged PSCs at an elevated temperature condition.[114,115] Moreover, the migration of Au into the perovskite layer occurs even in PSCs aged at room temperature under light illumination, leading to electronic shunts.[81] Therefore, interfacial design and modification are necessary to effectually reduce the trap states, the interfacial carrier recombination, and the ion and metal migrations. [67,82,84,85,116]

1.3 Potential of Halide Perovskite Materials in Thermoelectric Application

The rising energy consumption and growing climate concerns have prompted significant attention worldwide in recent years. To address global energy needs while mitigating the impact of fossil fuels, which contribute to global warming, alternative energy sources are being explored. TE generators offer a promising solution by harnessing heat from various sources such as home heating, automotive exhausts, and industrial processes, and directly converting it into electricity. Consequently, there is a global pursuit for TE materials that exhibit high performance, cost–effectiveness, environmental friendliness, and versatility across a wide temperature range.

HPs, including hybrid organic-inorganic and all inorganic variants, offer advantages over traditional TE materials like metal chalcogenides such as Bi_2Te_3 and PbTe. They are less expensive to produce, can be processed using low-energy methods, and are suitable for flexible device fabrication. These attributes make HP materials promising for a range of TE applications. Moreover, the unique properties of HPs, including their tunable bandgap, high charge carrier mobility, and excellent optoelectronic properties, make them highly desirable. Moreover, HPs have ultralow κ (less than 1 W m^{-1} K^{-1}), which has sparked interest in their potential as TE materials.[117] HPs are intriguingly classified as having a "phonon glass, electron crystal" structure, characterized by efficient charge transport akin to a good semiconductor, while heat transport is impeded, resembling a behavior observed in glass materials.[118,119] Additionally, HPs generally exhibit a superior room temperature S compared to other solution–processed materials, such as organics.[120,121]

Their ultralow κ coupled with optimization of other relevant TE parameters, such as the S and σ, has led to significant improvements in the performance of perovskite-based TE devices. As TE materials, HPs can offer high TE efficiency, particularly close to room temperature. Researchers have been aiming at enhancing the TE properties of HPs with various approaches including structure engineering, nanostructuring, alloying, doping, and interface engineering.

1.3.1 Introduction to Thermoelectric Phenomenon

Working principles

The TE effect encompasses both the Seebeck effect and the Peltier effect. The Seebeck effect involves the direct conversion of a temperature gradient into electricity. The Peltier effect is

the reverse of the Seebeck effect, where an electric current is used to create a temperature difference, leading to the cooling or heating of the junctions.

The Seebeck effect is the fundamental principle underlying the thermoelectric generator. In a TE generator, a temperature difference across the junctions of two different materials (or semiconductors) generates an electric current due to the Seebeck effect. This effect was discovered by German scientist Thomas Johann Seebeck in 1821. The Seebeck effect arises due to the diffusion of charge carriers from the hot side to the cold side, driven by the temperature gradient in both conductors and semiconductors (**Figure 1–10a**).

The magnitude of the Seebeck effect is quantified by the *S* which is defined as the TE voltage generated per unit temperature difference. For semiconductors, the sign of the *S* is related to the majority carrier type. Specifically, it is positive for p–type semiconductors and negative for n–type semiconductors. This distinction in sign arises from the dominant charge carriers in the semiconductor material.

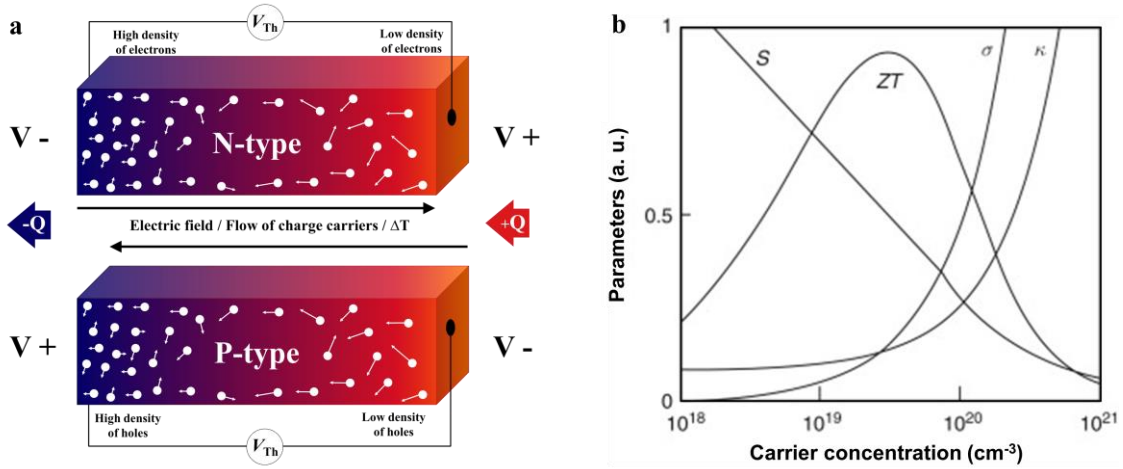

Figure 1–10. (a) Schematic representation of the charge carrier diffusion process in n– and p–type semiconductors under a temperature gradient. (b) Dependence of ZT, *S*, σ, and κ on carrier concentration.

The thermoelectric energy conversion efficiency is dependent on the dimensionless figure of merit (ZT) of thermoelectric materials which is evaluated by the Equation 1–4:

$$ZT = \frac{S^2 \sigma}{\kappa} T \qquad (1–4)$$

where σ is electrical conductivity, κ is thermal conductivity, and T is absolute temperature. $S^2 \sigma$ is defined as the TE power factor (PF).

According to the ZT equation, optimal thermoelectric materials require a substantial *S* to facilitate a significant thermoelectric effect, along with sufficient σ to minimize joule heat loss. Additionally, a low κ is essential to maintain a substantial temperature gradient. These TE parameters are influenced by various factors such as band structure, carrier concentration, phonon behavior, and others, making them interrelated and not independently controllable.[122] The interdependent relationship of σ, *S* and κ is shown in **Figure 1–10b.**

1.3.2 Overview of Halide Perovskites as a Promising Thermoelectric Material

HP materials, including hybrid organic–inorganic and all inorganic variants, offer advantages over traditional thermoelectric materials like metal chalcogenides such as Bi_2Te_3 and PbTe. They are less expensive to produce, can be processed using lower–energy methods, and are suitable for flexible device fabrication. These attributes make perovskite materials promising for a range of thermoelectric applications. Significantly, perovskites have garnered attention due to their ultralow κ, a property observed across various compositions and dimensions of perovskite structures.

Early studies focus on the thermoelectric properties of organic–inorganic hybrid HP like $MAPbI_3$. For instance, Pisoni *et al*. conducted experiments to measure the room–temperature κ of $MAPbI_3$ perovskite samples. They observed ultralow thermal conductivities of 0.5 W m^{-1} K^{-1} for single–crystalline samples and 0.3 W m^{-1} K^{-1} for polycrystalline samples.[117] Moreover, equilibrium molecular dynamics simulations have been used to investigate the thermal conductivities of different phases (cubic, tetragonal, and orthorhombic) of $MAPbI_3$ perovskites. It revealed that all phases exhibited thermal conductivities of less than 1 W m^{-1} K^{-1} at room temperature, with some values as low as 0.31 W m^{-1} K^{-1}. This ultralow κ is attributed to low phonon group velocities due to their intrinsic "soft" nature, particularly evident in organic-inorganic HPs, and their effective phonon scattering.[123,124] This intrinsic softness manifests as a liquid–like phonon transport behavior, wherein phonon transport is diffusive and impeded by effective phonon scattering.[117] Furthermore, the translation and rotational motions of methylammonium cations (MA^+) interact with the lead–iodide cages, coupling with isolated inorganic lattice vibrations. This interaction suppresses phonon transport in $MAPbI_3$, further reducing the phonon group velocity.[125] The combination of the phonon glass thermal transport behavior in the $MAPbI_3$ perovskite and slowly rotating MA^+ cation contributes to the ultralow κ.

The phenomenon of ultralow κ extends to all–inorganic HPs, which are thermally stable compared to perovskites with organic cations. The lattice thermal conductivities of $CsPbI_3$ and $CsSnI_3$ are estimated theoretically as 0.54 W m^{-1} K^{-1} and 0.25 W m^{-1} K^{-1}, respectively, at room temperature.[126] The temperature–dependent κ of $CsPbI_3$ has been observed in experimental measurements, showing changes similar to those seen in $MAPbI_3$, particularly at phase transition temperatures.[127] Yang *et al*. experimentally determined that $CsPbI_3$, $CsPbBr_3$, and $CsSnI_3$ nanowires have thermal conductivities of 0.45 ± 0.05 W m^{-1} K^{-1}, 0.42 ± 0.04 W m^{-1} K^{-1}, and 0.38 ± 0.04 W m^{-1} K^{-1}, respectively. The reason for this ultralow κ was the strong optical–acoustic phonon scatterings induced by collective motions across various dimensions, referred to as the cluster rattling mechanism.[128] A κ of 0.32 W m^{-1} K^{-1} has been reported in $CsSnBr_{3-x}I_x$ perovskites. This low κ is attributed to the off–centered Cs atom and distortion of the Sn—*X* (*X* = Br or I) octahedral, resulting in a highly dynamic and disordered structure that induces phonon resonance scattering. With this low κ, $CsSnBr_{3-x}I_x$ perovskites showed a ZT value close to 0.15.[28]

HPs have a relatively high *S*. For example, the *S* of $MAPbI_3$ has been measured at 700 μV K^{-1} at 295 K.[27] Moreover, an exceptionally high *S* of 920 μV K^{-1} at room temperature was observed for the high–quality single crystal prepared with inverted temperature crystallization.[129]

Moreover, it has been reported that it was possible to switch between n-type and p-type conduction in HPs by altering the composition of $MAPbI_3$ perovskite (**Figure 1-11**).[130] Liu *et al*. partially substituted I with Cl to induce n-type conduction. The shift occurs due to the vacancy of MA (V_{MA}), serving as a p-type dopant, primarily observed in single-halide $MAPbI_3$. However, the introduction of Cl suppresses the defect density of V_{MA}, leading to the domination of n-type doping.

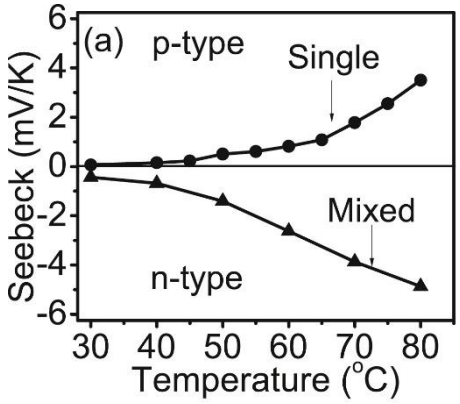

Figure 1-11. The Seebeck effects for single halide and mixed halide perovskite.[130]

With their combination of ultralow κ and high *S*, perovskite materials are expected to have a ZT value over 1 (**Figure 1-12**).[131] However, perovskite materials face limitations due to their

relatively low intrinsic σ. This restriction hampers the PF and ZT value of perovskite materials, which remains still much lower compared to conventional thermoelectric materials.[132,133] Therefore, it is possible to obtain a desirable ZT value by tuning the σ.

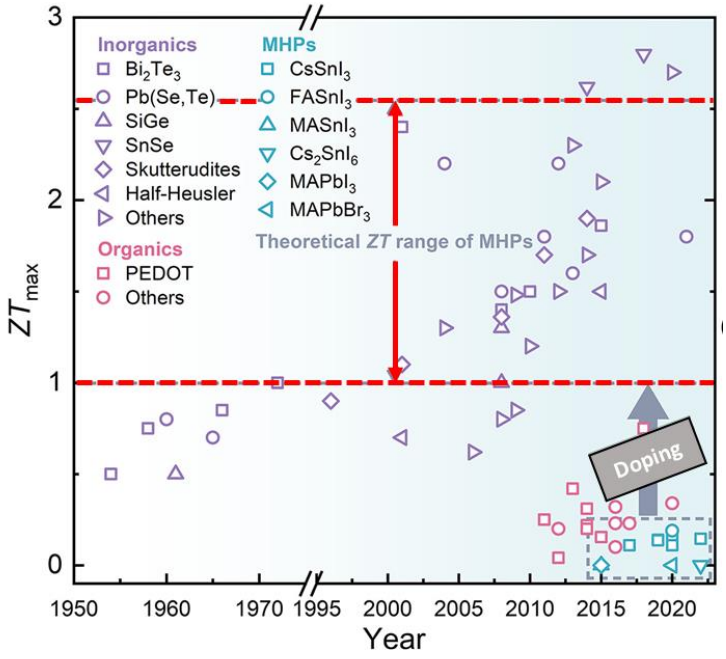

Figure 1-12. Timeline and progress in thermoelectric conversion efficiency represented for different types of materials. The red dashed line represents the theoretical ZT range of HPs, and the gray dashed box in the bottom right corner indicates the experimental values obtained for HPs. Reproduced from Ref.[131]

1.3.3 Recent Advances in Enhancing Thermoelectric Properties of Halide Perovskites

Improving carrier transport

Optimization of thin film fabrication:

In HP thin films, the presence of deep–level traps at grain boundaries poses challenges by creating potential barriers, increasing charge scattering, and reducing σ. Therefore, precise control over grain size and grain boundary area is critical for effective TE applications. Optimizing various film processing parameters, such as precursor components, solvents, annealing temperatures, and substrate temperature during thermal annealing, can influence the nucleation process and grain size of the thin films, enabling enhanced thermoelectric performance.

For example, Saini *et al*. aimed at increasing grain sizes and reducing visible grain boundaries by optimizing the thermal annealing temperature of the solution–processed $CsSnI_3$ thin film. As a result, the σ of the optimized film significantly increased from 11 S cm^{-1} to 124 S cm^{-1}

due to improved film morphology. Furthermore, they reported a ZT value of 0.137, one of the highest reported values for HP–based thermoelectric applications.[134] Additionally, they optimized the annealing duration for $MASnI_3$ films at 100°C, achieving the best σ of 3.56 S cm^{-1} and PF of 1.55 μW m^{-1} K^{-2}.[135] On the other hand, Liu *et al*. demonstrated that thermoelectric properties and stability of vapor–deposited thin films are influenced by the deposition procedure. They achieved high conductivity and better stability in Sn oxidized $CsSnI_3$ thin film fabricated using co–evaporation, sequential deposition, and seed layer plus sequential deposition (SLS) methods.[136]

Introducing interlayer:

Besides modifying the sample preparation process, introducing an interlayer improved the TE performance of HPs, resulting in reduced surface defects of the perovskite layer. For instance, a p–type semiconducting organic layer can neutralize the n–type surface defects of the perovskite layer, while a metal surface layer infiltrates into the crystal structure, diminishing defects, and inhibiting lattice expansion. As a result, a *S* as high as 1120 μV K^{-1} has been achieved.[137]

Modification of the substrate surface can also influence the crystallization of a perovskite film and result in better morphology. An additional Y_2O_3 scaffold layer influences the $CsSnI_3$ crystal growth and favors more conducting behavior with intrinsic defects (Sn^{4+}) formation, and the σ significantly improves from ~98 S cm^{-1} to ~310 S cm^{-1}. The phonon scattering path was also enhanced significantly with this additional layer due to formed defects/vacancy and reduced $CsSnI_3$ crystal size, which showed a reduction in κ from 0.74 W m^{-1} K^{-1} to 0. 28 W m^{-1} K^{-1}. With the combination of improved σ and reduced κ, a 0.11 ZT value was achieved.[138]

Improving carrier concentration

Despite potential improvements in charge transport through modifications in fabrication methods, low intrinsic carrier concentration limits σ and ZT value of HPs. For thermoelectric applications, the charge carrier concentration needs to be higher than 10^{19} cm^{-3}.[139] The carrier concentration can be improved through various doping strategies. Possible doping for perovskites can be either atomistic substitutional or molecular doping as well as photo–doping.

Self–doping

Point defects play a crucial role in self–doping within HPs, largely controlled by manipulating precursor ratios. For example, MAI–rich and PbI_2–rich $MAPbI_3$ can induce p– and n–type self–doping, respectively. Additionally, it was observed that varying the concentration of

chloride ions between pure $MAPbI_3$ and mixed $MAPbI_xCl_{3-x}$ could adjust the carrier type from p– to n–type, consequently influencing the *S*.[140,141] The composition–dependent transition of $MAPbI_3$ carrier types enables the fabrication of efficient thermoelectric devices with different charge carrier characteristics.

Generally, Sn–based perovskites have higher σ compared to Pb–based perovskites. $MASnI_3$ single crystals show metallic charge transport behavior attributed to a low level of hole doping.[142] This behavior arises from the self p–doping nature originating from the facile oxidation of Sn^{2+} and the high stability of V_{Sn}. The oxidization from Sn^{2+} to Sn^{4+} leads to the formation of V_{Sn}, accompanied by the release of two holes to achieve charge neutrality and act as p–doping.[143,144] In addition, Sn(IV) defects are thermodynamically metastable and thus they will spontaneously transform into Sn(II) defects with the release of additional holes in the VB.[144]

This high level of p–doping can effectively enhance the σ and lead to an efficient thermoelectric performance of Sn–based perovskites. Haque *et al*. applied air treatment in $MASnI_3$ thin films for a few minutes to induce self–doping and thus enhanced the σ.[145] Similarly, Sn^{4+} was introduced before $CsSnI_3$ nucleation by aging the precursor solution for several hours, resulting in an improvement of the σ from 88.83 S cm^{-1} to 244.5 S cm^{-1}. Consequently, a room–temperature ZT of 0.12 was achieved.[146]

Extrinsic doping

HPs are known to be highly sensitive to synthesis conditions, potentially leading to poor reproducibility with the self–doping approach. Additionally, non–stoichiometric perovskites may exhibit faster degradation, depending on the sample composition. Therefore, extrinsic dopants are of interest for improving the thermoelectric performance of HPs,

The use of atomistic dopants would include replacing the divalent metal cation with a different heterovalent ion. Among the different possibilities, a Bi^{3+} dopant emerges as the most promising, as it has demonstrated a substantial increase in σ from 1.5×10^{-8} S cm^{-1} to 1.5×10^{-4} S cm^{-1}.[147] Besides, it retained ultralow κ of 0.33 ± 0.04 W m^{-1} K^{-1} and large S of –378 μV K^{-1}. Ge^{2+} has also been substituted partially in $CsSnI_3$ perovskite, where the perovskite phase becomes more stable with the substitution and ultrafast GeI_2 oxidation. Consequently, reduced defects and traps and increased carrier concentration with Ge^{2+} substitution improved σ from 86.4 S cm^{-1} to 190.1 S cm^{-1}.[148]

While atomistic substitutional doping and self–doping increase the carrier concentration with intrinsic and extrinsic charged defects introduced into the perovskite lattice, molecular doping

facilitates charge transfer between the molecular dopant and the perovskite host.[149] Doping through charge transfer requires an appropriate selection of the molecular dopant. For p–type doping, the LUMO of the molecular dopant lies near or below the VBM of the perovskite host. The different molecules such as tetracyanoquinodimethane (TCNQ), 2,3,5,6–tetrafluorotetracyanoquinodimethane (F_4–TCNQ), benzoquinone (BQ), hydroquinone, and cobaltocene has been used for HPs. Among them, F_4–TCNQ has already resulted in the highest reported ZT value (0.19) for $FASnI_3$ perovskite by increasing the σ.[120] This improvement is attributed to the increased charge carrier concentrations and mobilities as well as superior film morphologies. Although F_4–TCNQ molecules are too big to enter the lattice sites of perovskites, doping at the grain boundaries of polycrystalline films also affects the morphology of the films.

1.3.4 Challenges of Perovskite Materials in Thermoelectric

HP materials are expected to have a ZT value over 1 with the combination of their ultralow κ and high S.[131] However, the low intrinsic σ, and therefore a low PF of HPs has been one of the main challenges for realizing a high ZT value, which remain still much lower compared to conventional TE materials.[132,133] In HP thin films, the presence of deep-level traps at grain boundaries poses challenges by creating potential barriers, increasing charge scattering, and reducing σ. Despite these issues with charge transport, the low intrinsic carrier concentration ultimately limits σ. However, efficient doping methods for controlling their carrier concentration have been lacking while most of the previous studies have focused on improving their optical properties or film quality and stability. Furthermore, prior studies have predominantly focused on investigating the general TE and thermal transport properties of HPs. Consequently, a noticeable gap remains in directly examining doping strategies for HP TEs and their consequent impact on charge transport.

1.4 Overview of the Thesis

This thesis focuses on exploring the potential of perovskite materials for next–generation energy conversion devices, including perovskite solar cells and thermoelectric devices. As mentioned earlier, although perovskite material–based solar cells have been developed significantly, there are still unknown challenges that limit long–term durability and initial PCE. Further clarification of the underlying reasons and mechanisms behind these challenges is imperative. On the other hand, despite their ultralow κ and high S, perovskite materials face limitations in overall TE performance due to their relatively low σ. Therefore, it is necessary to increase the electrical conductivity of HPs to achieve a higher ZT value, consequently enhancing its overall TE performance.

The primary objective of Chapter 2 is to conduct an in–depth investigation into the degradation mechanisms of PSCs. Particularly, the oxidation of the spiro–OMeTAD HTL could be the reason for the decreased performance of PSCs under operational conditions, especially for long–duration use in air even though the decomposition of perovskites has been reported as a reason.[80,91,101] While previous studies have suggested that the perovskites decompose under operational conditions, especially for long–duration use in air, the oxidation of the spiro–OMeTAD HTL could be a contributing factor to decreased performance. Therefore, this research aims at elucidating the underlying mechanisms regarding oxygen–induced degradation in PSCs by systematically studying the influence of oxygen on the performances of PSCs, including PCEs, long–term durability, and charge extraction and recombination properties. Through detailed experimentation and analysis, I aim at providing valuable insights into the complex interplay between oxygen exposure and PSC performance, ultimately paving the way for the development of strategies to enhance the long–term durability of PSC devices.

In Chapter 3, my focus is on addressing the challenges impeding the PCEs of PSCs through interfacial modification. Building upon the identified issues such as energy–level mismatch, and ion and metal migration, this research aims to develop an effective strategy to overcome these hindrances. Specifically, by introducing a robust molybdenum oxide (MoO_x) interlayer between the spiro–OMeTAD HTL and the Au electrode, this study aims to prevent the penetration of gold (Au) into the perovskite layer, which is a limiting factor in PCEs due to detrimental carrier recombination. I seek to clarify the underlying mechanisms and demonstrate the effectiveness of the MoO_x interlayer in improving both initial PCE and the long–term durability of PSCs.

In Chapter 4, I attempt to address the significance of developing effective doping methods for HP TEs. The primary objective is to enhance the electrical conductivity of HP material by boosting its intrinsic carrier concentration to achieve high TE performance. Therefore, the molecular doping into solution-processed $CsSnI_3$ thin film is proposed to increase the carrier concentration.

Chapter 5 provides a summary of the results obtained in this thesis, accompanied by an exploration of future perspectives.

References

[1] H. Tanaka, M. Misono, *Curr. Opin. Solid State Mater. Sci.* **2001**, *5*, 381.

[2] D. G. Schlom, L. Q. Chen, X. Pan, A. Schmehl, M. A. Zurbuchen, *J. Am. Ceram. Soc.* **2008**, *91*, 2429.

[3] R. H. Mitchell, M. D. Welch, A. R. Chakhmouradian, *Mineral. Mag.* **2017**, *81*, 411.

[4] Q. A. Akkerman, L. Manna, *ACS Energy Lett.* **2020**, *5*, 604.

[5] P. S. Whitfield, N. Herron, W. E. Guise, K. Page, Y. Q. Cheng, I. Milas, M. K. Crawford, *Sci. Rep.* **2016**, *6*, 1.

[6] N. Onoda-Yamamuro, T. Matsuo, H. Suga, *J. Phys. Chem. Solids* **1990**, *51*, 1383.

[7] A. Poglitsch, D. Weber, *J. Chem. Phys.* **1987**, *87*, 6373.

[8] A. M. Glazer, *Acta Crystallogr. Sect. B Struct. Crystallogr. Cryst. Chem.* **1972**, *28*, 3384.

[9] M. W. Lufaso, P. M. Woodward, *Acta Crystallogr. Sect. B Struct. Sci.* **2001**, *57*, 725.

[10] H. T. Stokes, E. H. Kisi, D. M. Hatch, C. J. Howard, *Acta Crystallogr. Sect. B Struct. Sci.* **2002**, *58*, 934.

[11] H. L. Bowman, *Mineral. Mag. J. Mineral. Soc.* **1908**, *15*, 156.

[12] V. M. Goldschmidt, *Titanium pigment and process of producing the same*, US patent office, USA, **1922**.

[13] B. M. Vul, I. M. Goldman, In *Dokl aN SSSr*, **1945**, pp. 154–157.

[14] A. von Hippel, R. G. Breckenridge, F. G. Chesley, L. Tisza, *Ind. Eng. Chem.* **1946**, *38*, 1097.

[15] C. K. Møller, *Nature* **1958**, *182*, 1436.

[16] D. Balz, *Naturwissenschaften* **1953**, *40*, 241.

[17] R. Willett, H. Place, M. Middleton, *J. Am. Chem. Soc.* **1988**, *110*, 8639.

[18] R Geick, K Strobel, *J. Phys. C Solid State Phys.* **1979**, *12*, 27.

[19] G. FS, *Perovskites and High Tc Superconductors*, Gordon and Breach Science Publishers, New York, **1990**.

[20] L. G. Tejuca, J. L. G. Fierro, *Properties and applications of perovskite-type oxides*, CRC Press, **1992**.

[21] K.-D. Kreuer, *Annu. Rev. Mater. Res.* **2003**, *33*, 333.

[22] T. Ishihara, *Perovskite oxide for solid oxide fuel cells*, Springer Science & Business Media, **2009**.

[23] T. Qi, I. Grinberg, J. W. Bennett, Y.-H. Shin, A. M. Rappe, K.-L. Yeh, K. A. Nelson, In *2010 DoD High Performance Computing Modernization Program Users Group Conference*, IEEE, **2010**, pp. 249–258.

[24] M. Liu, M. B. Johnston, H. J. Snaith, *Nature* **2013**, *501*, 395.

[25] W. J. Yin, T. Shi, Y. Yan, *Adv. Mater.* **2014**, *26*, 4653.

[26] K. Wang, D. Yang, C. Wu, M. Sanghadasa, S. Priya, *Prog. Mater. Sci.* **2019**, *106*, 100580.

[27] X. Mettan, R. Pisoni, P. Matus, A. Pisoni, J. Jaćimović, B. Náfrádi, M. Spina, D. Pavuna, L. Forró, E. Horváth, *J. Phys. Chem. C* **2015**, *119*, 11506.

[28] H. Xie, S. Hao, J. Bao, T. J. Slade, G. J. Snyder, C. Wolverton, M. G. Kanatzidis, *J. Am. Chem. Soc.* **2020**, *142*, 9553.

[29] G. C. Papavassiliou, I. B. Koutselas, *Synth. Met.* **1995**, *71*, 1713.

[30] L. Y. Huang, W. R. L. Lambrecht, *Phys. Rev. B - Condens. Matter Mater. Phys.* **2013**, *88*, 1.

[31] K. Yamada, H. Kawaguchi, T. Matsui, T. Okuda, S. Ichiba, *Bull. Chem. Soc. Jpn.* **1990**, *63*, 2521.

[32] C. Liu, Y. B. Cheng, Z. Ge, *Chem. Soc. Rev.* **2020**, *49*, 1653.

[33] Q. Ma, S. Huang, X. Wen, M. A. Green, A. W. Y. Ho-Baillie, *Adv. energy Mater.* **2016**, *6*.

[34] I. B. Koutselas, L. Ducasse, G. C. Papavassiliou, *J. Phys. Condens. Matter* **1996**, *8*, 1217.

[35] F. Chiarella, A. Zappettini, F. Licci, I. Borriello, G. Cantele, D. Ninno, A. Cassinese, R. Vaglio, *Phys. Rev. B* **2008**, *77*, 45129.

[36] F. Brivio, A. B. Walker, A. Walsh, *Apl Mater.* **2013**, *1*.

[37] T. Umebayashi, K. Asai, T. Kondo, A. Nakao, *Phys. Rev. B* **2003**, *67*, 155405.

[38] Q. Lin, A. Armin, R. Chandra, R. Nagiri, P. L. Burn, P. Meredith, **2015**.

[39] S. Sun, T. Salim, N. Mathews, M. Duchamp, C. Boothroyd, G. Xing, T. C. Sum, Y. M. Lam, *Energy Environ. Sci.* **2014**, *7*, 399.

[40] M. Shirayama, H. Kadowaki, T. Miyadera, T. Sugita, M. Tamakoshi, M. Kato, T. Fujiseki, D. Murata, S. Hara, T. N. Murakami, S. Fujimoto, M. Chikamatsu, H. Fujiwara, *Phys. Rev. Appl.* **2016**, *5*, 1.

[41] G. Xing, N. Mathews, S. S. Lim, Y. M. Lam, S. Mhaisalkar, T. C. Sum, *Science (80-.).* **2013**, *342*, 344.

[42] Q. Lin, A. Armin, R. C. R. Nagiri, P. L. Burn, P. Meredith, *Nat. Photonics* **2015**, *9*, 106.

[43] A. Soultati, M. Tountas, K. K. Armadorou, A. R. bin M. Yusoff, M. Vasilopoulou, M. K. Nazeeruddin, *Energy Adv.* **2023**, *2*, 1075.

[44] D. Shi, V. Adinolfi, R. Comin, M. Yuan, E. Alarousu, A. Buin, Y. Chen, S. Hoogland, A. Rothenberger, K. Katsiev, *Science (80-.).* **2015**, *347*, 519.

[45] K. K. Ng, *Physics of semiconductor devices [electronic book].*, Wiley-interscience, **2007**.

[46] R. Ulbricht, E. Hendry, J. Shan, T. F. Heinz, M. Bonn, *Rev. Mod. Phys.* **2011**, *83*, 543.

[47] G. Masetti, M. Severi, S. Solmi, *IEEE Trans. Electron Devices* **1983**, *30*, 764.

[48] Q. Jiang, Z. Chu, P. Wang, X. Yang, H. Liu, Y. Wang, Z. Yin, J. Wu, X. Zhang, J. You, *Adv. Mater.* **2017**, *29*, 1703852.

[49] Q. Jiang, L. Zhang, H. Wang, X. Yang, J. Meng, H. Liu, Z. Yin, J. Wu, X. Zhang, J. You, *Nat. Energy* **2016**, *2*, 16177.

[50] F. Liu, Q. Dong, M. K. Wong, A. B. Djurišić, A. Ng, Z. Ren, Q. Shen, C. Surya, W. K. Chan, J. Wang, *Adv. Energy Mater.* **2016**, *6*, 1502206.

[51] F. Hao, C. C. Stoumpos, R. P. H. Chang, M. G. Kanatzidis, *J. Am. Chem. Soc.* **2014**, *136*, 8094.

[52] A. Bianconi, N. Saini, T. Rossetti, A. Lanzara, A. Perali, M. Missori, H. Oyanagi, H. Yamaguchi, Y. Nishihara, *Phys. Rev. B - Condens. Matter Mater. Phys.* **1996**, *54*, 12018.

[53] I. Chung, J. H. Song, J. Im, J. Androulakis, C. D. Malliakas, H. Li, A. J. Freeman, J. T. Kenney, M. G. Kanatzidis, *J. Am. Chem. Soc.* **2012**, *134*, 8579.

[54] A. Kojima, K. Teshima, Y. Shirai, T. Miyasaka, *J. Am. Chem. Soc.* **2009**, *131*, 6050.

[55] S. Ma, G. Yuan, Y. Zhang, N. Yang, Y. Li, Q. Chen, *Energy Environ. Sci* **2022**, *15*, 13.

[56] J. J. Yoo, G. Seo, M. R. Chua, T. Gwan Park, Y. Lu, F. Rotermund, Y. K. Kim, C. Su Moon, N. Joong Jeon, J. P. Correa Baena, V. Bulović, S. Sik Shin, M. G. Bawendi, J. Seo, *Nature* **2021**, *590*, 587.

[57] W. Feng, J. Tao, G. Liu, G. Yang, J. Zhong, Y. Fang, L. Gong, S. Yang, W. Wu, *Angew. Chemie*

2023, *135*, e202300265.

[58] S. D. Stranks, G. E. Eperon, G. Grancini, C. Menelaou, M. J. P. Alcocer, T. Leijtens, L. M. Herz, A. Petrozza, H. J. Snaith, *Science (80-.).* **2013**, *342*, 341.

[59] M. A. Green, A. Ho-Baillie, H. J. Snaith, *Nat. Photonics* **2014**, *8*, 506.

[60] N. Pellet, P. Gao, G. Gregori, T.-Y. Yang, M. K. Nazeeruddin, J. Maier, M. Grätzel, .

[61] W. S. Yang, J. H. Noh, N. J. Jeon, Y. C. Kim, S. Ryu, J. Seo, S. Seok, *Science (80-.).* **2015**, *348*, 1234.

[62] A. Miyata, A. Mitioglu, P. Plochocka, O. Portugall, J. T. W. Wang, S. D. Stranks, H. J. Snaith, R. J. Nicholas, *Nat. Phys.* **2015**, *11*, 582.

[63] Z. Li, Y. Zhao, X. Wang, Y. Sun, Z. Zhao, Y. Li, H. Zhou, Q. Chen, *Joule* **2018**, *2*, 1559.

[64] NREL, *Best research cell efficiency chart*, **2022**.

[65] Y. Liu, B. Jin, H. Zhang, Y. Zhang, Y. Kim, C. Wang, S. Wen, B. Xu, C. Im, W. Tian, *ACS Appl. Mater. Interfaces* **2019**, *11*, 14810.

[66] Z. Shi, A. H. Jayatissa, *Perovskites-Based Solar Cells: A Review of Recent Progress, Materials and Processing Methods*, Vol. 11, **2018**.

[67] H. Zhou, Q. Chen, G. Li, S. Luo, T. B. Song, H. S. Duan, Z. Hong, J. You, Y. Liu, Y. Yang, *Science* **2014**, *345*, 542.

[68] L. Meng, J. You, T.-F. Guo, Y. Yang, *Acc. Chem. Res.* **2016**, *49*, 155.

[69] J. Y. Jeng, Y. F. Chiang, M. H. Lee, S. R. Peng, T. F. Guo, P. Chen, T. C. Wen, *Adv. Mater.* **2013**, *25*, 3727.

[70] L. Hu, K. Sun, M. Wang, W. Chen, B. Yang, J. Fu, Z. Xiong, X. Li, X. Tang, Z. Zang, S. Zhang, L. Sun, M. Li, *ACS Appl. Mater. Interfaces* **2017**, *9*, 43902.

[71] J. Chen, N.-G. Park, *J. Phys. Chem. C* **2018**, *122*, 14039.

[72] H.-S. Kim, C.-R. Lee, J.-H. Im, K.-B. Lee, T. Moehl, A. Marchioro, S.-J. Moon, R. Humphry-Baker, J.-H. Yum, J. E. Moser, M. Grätzel, N.-G. Park, *Sci. Rep.* **2012**, *2*, 591.

[73] J. M. Ball, M. M. Lee, A. Hey, H. J. Snaith, *Energy Environ. Sci.* **2013**, *6*, 1739.

[74] L. K. Ono, E. J. Juarez-Perez, Y. Qi, *ACS Appl. Mater. Interfaces* **2017**, *9*, 30197.

[75] M. Saliba, J. P. Correa-Baena, C. M. Wolff, M. Stolterfoht, N. Phung, S. Albrecht, D. Neher, A. Abate, *Chem. Mater.* **2018**, *30*, 4193.

[76] A. Abate, T. Leijtens, S. Pathak, J. Teuscher, R. Avolio, M. E. Errico, J. Kirkpatrik, J. M. Ball, P. Docampo, I. Mcpherson, H. J. Snaith, *Phys. Chem. Chem. Phys* **2013**, *15*, 2572.

[77] H. J. Snaith, M. Grätzel, *Appl. Phys. Lett* **2006**, *89*, 262114.

[78] D. Poplavskyy, J. Nelson, *J. Appl. Phys.* **2003**, *93*, 341.

[79] X. Yang, D. Luo, Y. Xiang, L. Zhao, M. Anaya, Y. Shen, J. Wu, W. Yang, Y. H. Chiang, Y. Tu, R. Su, Q. Hu, H. Yu, G. Shao, W. Huang, T. P. Russell, Q. Gong, S. D. Stranks, W. Zhang, R. Zhu, *Adv. Mater.* **2021**, *33*, 2006435.

[80] K. Domanski, J.-P. Correa-Baena, N. Mine, M. K. Nazeeruddin, A. Abate, M. Saliba, W. Tress, A. Hagfeldt, M. Grätzel, *ACS Nano* **2016**, *10*, 6306.

[81] S. Guarnera, A. Abate, W. Zhang, J. M. Foster, G. Richardson, A. Petrozza, H. J. Snaith, *J. Phys. Chem. Lett.* **2015**, *6*, 432.

[82] D. Yang, X. Zhou, R. Yang, Z. Yang, W. Yu, X. Wang, C. Li, S. Liu, R. P. H. Chang, *Energy Environ. Sci.* **2016**, *9*, 3071.

[83] N. K. Noel, S. N. Habisreutinger, B. Wenger, Y. H. Lin, F. Zhang, J. B. Patel, A. Kahn, M. B. Johnston, H. J. Snaith, *Adv. Energy Mater.* **2020**, *10*, 1903231.

[84] S. Sonmezoglu, S. Akin, *Nano Energy* **2020**, *76*, 105127.

[85] J. Xia, M. Sohail, M. K. Nazeeruddin, *Adv. Mater.* **2023**, *35*, 2211324.

[86] G. Grancini, M. K. Nazeeruddin, *Nat. Rev. Mater.* **2019**, *4*, 4.

[87] P. Gao, A. R. Bin Mohd Yusoff, M. K. Nazeeruddin, *Nat. Commun.* **2018**, *9*, 5028.

[88] N. J. Jeon, J. H. Noh, W. S. Yang, Y. C. Kim, S. Ryu, J. Seo, S. Il Seok, *Nature* **2015**, *517*, 476.

[89] M. Saliba, T. Matsui, J. Y. Seo, K. Domanski, J. P. Correa-Baena, M. K. Nazeeruddin, S. M. Zakeeruddin, W. Tress, A. Abate, A. Hagfeldt, M. Grätzel, *Energy Environ. Sci.* **2016**, *9*, 1989.

[90] S. Tan, I. Yavuz, N. De Marco, T. Huang, S. J. Lee, C. S. Choi, M. Wang, S. Nuryyeva, R. Wang, Y. Zhao, H. C. Wang, T. H. Han, B. Dunn, Y. Huang, J. W. Lee, Y. Yang, *Adv. Mater.* **2020**, *32*, 1906995.

[91] T. A. Berhe, W. N. Su, C. H. Chen, C. J. Pan, J. H. Cheng, H. M. Chen, M. C. Tsai, L. Y. Chen, A. A. Dubale, B. J. Hwang, *Energy Environ. Sci.* **2016**, *9*, 323.

[92] E. T. Hoke, D. J. Slotcavage, E. R. Dohner, A. R. Bowring, H. I. Karunadasa, M. D. McGehee, *Chem. Sci.* **2015**, *6*, 613.

[93] D. Wei, T. Wang, J. Ji, M. Li, P. Cui, Y. Li, G. Li, J. M. Mbengue, D. Song, *J. Mater. Chem. A* **2016**, *4*, 1991.

[94] B. Conings, J. Drijkoningen, N. Gauquelin, A. Babayigit, J. D'Haen, L. D'Olieslaeger, A. Ethirajan, J. Verbeeck, J. Manca, E. Mosconi, F. De Angelis, H. G. Boyen, *Adv. Energy Mater.* **2015**, *5*, 1500477.

[95] J. A. Christians, P. A. Miranda Herrera, P. V. Kamat, *J. Am. Chem. Soc.* **2015**, *137*, 1530.

[96] J. Yang, B. D. Siempelkamp, D. Liu, T. L. Kelly, *ACS Nano* **2015**, *9*, 1955.

[97] A. J. Pearson, G. E. Eperon, P. E. Hopkinson, S. N. Habisreutinger, J. T. W. Wang, H. J. Snaith, N. C. Greenham, *Adv. Energy Mater.* **2016**, *6*, 1600014.

[98] N. Aristidou, C. Eames, I. Sanchez-Molina, X. Bu, J. Kosco, M. Saiful Islam, S. A. Haque, *Nat. Commun.* **2017**, *8*, 15218.

[99] A. D. Sheikh, A. Bera, M. A. Haque, R. B. Rakhi, S. Del Gobbo, H. N. Alshareef, T. Wu, *Sol. Energy Mater. Sol. Cells* **2015**, *137*, 6.

[100] T. Leijtens, G. E. Eperon, N. K. Noel, S. N. Habisreutinger, A. Petrozza, H. J. Snaith, *Adv. Energy Mater.* **2015**, *5*, 1500963.

[101] S. Mazumdar, Y. Zhao, X. Zhang, *Front. Electron.* **2021**, *2*, 712785.

[102] K. Domanski, E. A. Alharbi, A. Hagfeldt, M. Grätzel, W. Tress, *Nat. Energy* **2018**, *3*, 61.

[103] Y. Han, S. Meyer, Y. Dkhissi, K. Weber, J. M. Pringle, U. Bach, L. Spiccia, Y. B. Cheng, *J. Mater. Chem. A* **2015**, *3*, 8139.

[104] G. Niu, W. Li, F. Meng, L. Wang, H. Dong, Y. Qiu, *J. Mater. Chem. A* **2014**, *2*, 705.

[105] J. M. Frost, K. T. Butler, F. Brivio, C. H. Hendon, M. Van Schilfgaarde, A. Walsh, *Nano Lett.* **2014**, *14*, 2584.

[106] B. Tan, S. R. Raga, A. S. R. Chesman, S. O. Fürer, F. Zheng, D. P. McMeekin, L. Jiang, W. Mao, X. Lin, X. Wen, J. Lu, Y. B. Cheng, U. Bach, *Adv. Energy Mater.* **2019**, *9*, 1901519.

[107] Z. Hawash, L. K. Ono, Y. Qi, *Adv. Mater. Interfaces* **2016**, *3*, 1600117.

[108] Z. Song, A. Abate, S. C. Watthage, G. K. Liyanage, A. B. Phillips, U. Steiner, M. Graetzel, M. J. Heben, *Adv. Energy Mater.* **2016**, *6*, 1600846.

[109] Z. Hawash, L. K. Ono, S. R. Raga, M. V. Lee, Y. Qi, *Chem. Mater.* **2015**, *27*, 562.

[110] X. Zhou, W. Qi, J. Li, J. Cheng, Y. Li, J. Luo, M. J. Ko, Y. Li, Y. Zhao, X. Zhang, *Sol. RRL* **2020**, *4*, 2000308.

[111] E. Aydin, M. De Bastiani, S. De Wolf, *Adv. Mater.* **2019**, *31*, 1900428.

[112] H. Tan, A. Jain, O. Voznyy, X. Lan, F. P. G. De Arquer, J. Z. Fan, R. Quintero-Bermudez, M. Yuan, B. Zhang, Y. Zhao, F. Fan, P. Li, L. N. Quan, Y. Zhao, Z. H. Lu, Z. Yang, S. Hoogland, E. H. Sargent, *Science* **2017**, *355*, 722.

[113] Z. Lin, J. Chang, J. Xiao, H. Zhu, Q. H. Xu, C. Zhang, J. Ouyang, Y. Hao, *Sol. Energy Mater. Sol. Cells* **2016**, *157*, 783.

[114] K. Domanski, N. Mine, M. G. Nazeeruddin, Mohammad Khaja Nazeeruddin, Antonio abate, Michael Saliba, Wolfgang Tress, Anders Hagfeldt, **2016**, *10*, 6306.

[115] S. Wu, R. Chen, S. Zhang, B. H. Babu, Y. Yue, H. Zhu, Z. Yang, C. Chen, W. Chen, Y. Huang, S. Fang, T. Liu, L. Han, W. Chen, *Nat. Commun.* **2019**, *10*, 1161.

[116] X. Chang, J. X. Zhong, S. Li, Q. Yao, Y. Fang, G. Yang, Y. Tan, Q. Xue, L. Qiu, Q. Wang, Y. Peng, W. Q. Wu, *Angew. Chemie - Int. Ed.* **2023**, *62*, e202309292.

[117] C. Lee, J. Hong, A. Stroppa, M. H. Whangbo, J. H. Shim, *RSC Adv.* **2015**, *5*, 78701.

[118] K. Miyata, T. L. Atallah, X. Y. Zhu, *Sci. Adv.* **2017**, *3*.

[119] M. Beekman, D. T. Morelli, G. S. Nolas, *Nat. Mater.* **2015**, *14*, 1182.

[120] B. Russ, A. Glaudell, J. J. Urban, M. L. Chabinyc, R. A. Segalman, *Nat. Rev. Mater.* **2016**, *1*, 1.

[121] C. C. Stoumpos, C. D. Malliakas, M. G. Kanatzidis, *Inorg. Chem.* **2013**, *52*, 9019.

[122] M. Hamid Elsheikh, D. A. Shnawah, M. F. M. Sabri, S. B. M. Said, M. Haji Hassan, M. B. Ali Bashir, M. Mohamad, *Renew. Sustain. Energy Rev.* **2014**, *30*, 337.

[123] Z. Guo, S. J. Yoon, J. S. Manser, P. V. Kamat, T. Luo, *J. Phys. Chem. C* **2016**, *120*, 6394.

[124] T. Baikie, Y. Fang, J. M. Kadro, M. Schreyer, F. Wei, S. G. Mhaisalkar, M. Graetzel, T. J. White, *J. Mater. Chem. A* **2013**, *1*, 5628.

[125] T. Hata, G. Giorgi, K. Yamashita, *Nano Lett.* **2016**, *16*, 2749.

[126] S. D. Guo, J. L. Wang, *RSC Adv.* **2016**, *6*, 101552.

[127] A. Kovalsky, L. Wang, G. T. Marek, C. Burda, J. S. Dyck, *J. Phys. Chem. C* **2017**, *121*, 3228.

[128] W. Lee, H. Li, A. B. Wong, D. Zhang, M. Lai, Y. Yu, Q. Kong, E. Lin, J. J. Urban, J. C. Grossman, P. Yang, *Proc. Natl. Acad. Sci. U. S. A.* **2017**, *114*, 8693.

[129] T. Ye, X. Wang, X. Li, A. Q. Yan, S. Ramakrishna, J. Xu, *J. Mater. Chem. C* **2017**, *5*, 1255.

[130] Q. Liu, Y. C. Hsiao, M. Ahmadi, T. Wu, L. Liu, S. Haacke, H. Wang, B. Hu, *Org. Electron.* **2016**, *35*, 216.

[131] Y. Kim, H. Choi, J. Lee, Y. K. Jung, J. Jung, J. Cho, T. Lee, K. Kang, *EcoMat* **2023**, *5*, 1.

[132] A. T. Duong, V. Q. Nguyen, G. Duvjir, V. T. Duong, S. Kwon, J. Y. Song, J. K. Lee, J. E. Lee, S. Park, T. Min, J. Lee, J. Kim, S. Cho, *Nat. Commun.* **2016**, *7*, 1.

[133] B. Qin, Y. Zhang, D. Wang, Q. Zhao, B. Gu, H. Wu, H. Zhang, B. Ye, S. J. Pennycook, L.-D. Zhao, *J. Am. Chem. Soc.* **2020**, *142*, 5901.

[134] S. Saini, A. K. Baranwal, T. Yabuki, S. Hayase, K. Miyazaki, *MRS Adv.* **2019**, *4*, 1719.

[135] S. Saini, A. K. Baranwal, T. Yabuki, S. Hayase, K. Miyazaki, *J. Electron. Mater.* **2020**, *49*, 2890.

[136] T. Liu, X. Zhao, J. Li, Z. Liu, F. Liscio, S. Milita, B. C. Schroeder, O. Fenwick, *Nat. Commun.* **2019**, *10*, 1.

[137] L. Sun, L. Xu, Y. Xiong, P. Wu, G. Xie, B. Hu, *Adv. Electron. Mater.* **2019**, *5*, 3.

[138] A. K. Baranwal, S. Saini, Z. Wang, D. Hirotani, T. Yabuki, S. Iikubo, K. Miyazaki, S. Hayase, *Org. Electron.* **2020**, *76*, 105488.

[139] D. M. Rowe, *CRC handbook of thermoelectrics*, CRC press, **2018**.

[140] Q. Wang, Y. Shao, H. Xie, L. Lyu, X. Liu, Y. Gao, J. Huang, *Appl. Phys. Lett.* **2014**, *105*.

[141] B. Danekamp, C. Müller, M. Sendner, P. P. Boix, M. Sessolo, R. Lovrincic, H. J. Bolink, *J. Phys. Chem. Lett.* **2018**, *9*, 2770.

[142] Y. Takahashi, R. Obara, Z. Z. Lin, Y. Takahashi, T. Naito, T. Inabe, S. Ishibashi, K. Terakura, *Dalt. Trans.* **2011**, *40*, 5563.

[143] S. Gupta, D. Cahen, G. Hodes, *J. Phys. Chem. C* **2018**, *122*, 13926.

[144] D. Ricciarelli, D. Meggiolaro, F. Ambrosio, F. De Angelis, *ACS Energy Lett.* **2020**, *5*, 2787.

[145] M. A. Haque, L. H. Hernandez, B. Davaasuren, D. R. Villalva, J. Troughton, D. Baran, *Adv. Energy Sustain. Res.* **2020**, *1*, 1.

[146] A. K. Baranwal, S. Saini, Z. Wang, K. Hamada, D. Hirotani, K. Nishimura, M. A. Kamarudin, G. Kapil, T. Yabuki, S. Iikubo, Q. Shen, K. Miyazaki, S. Hayase, *J. Electron. Mater.* **2020**, *49*, 2698.

[147] A. L. Abdelhady, M. I. Saidaminov, B. Murali, V. Adinolfi, O. Voznyy, K. Katsiev, E. Alarousu, R. Comin, I. Dursun, L. Sinatra, E. H. Sargent, O. F. Mohammed, O. M. Bakr, *J. Phys. Chem. Lett.* **2016**, *7*, 295.

[148] F. Qian, M. Hu, J. Gong, C. Ge, Y. Zhou, J. Guo, M. Chen, Z. Ge, N. P. Padture, Y. Zhou, J. Feng, *J. Phys. Chem. C* **2020**, *124*, 11749.

[149] J. Euvrard, Y. Yan, D. B. Mitzi, *Nat. Rev. Mater.* **2021**, *6*, 531.

CHAPTER 2

Oxygen–Induced Degradation of Perovskite Solar Cells

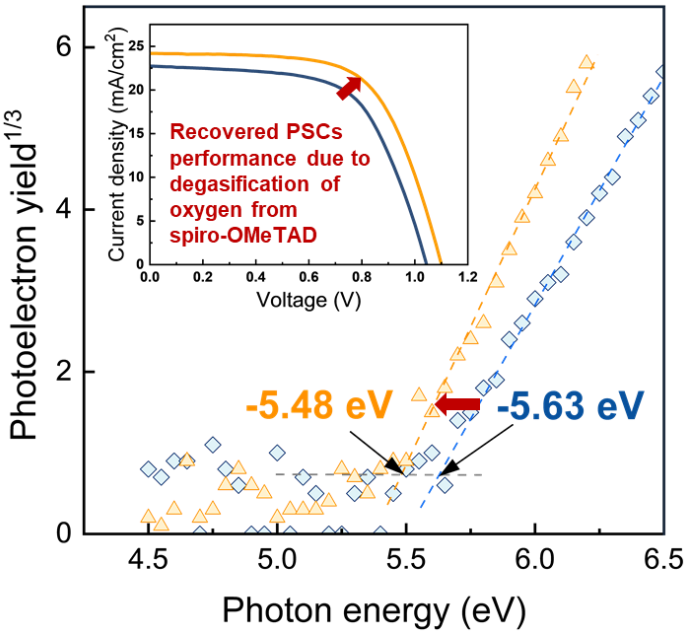

Chapter 2: Oxygen–Induced Degradation of Perovskite Solar Cells

2.1 Introduction

One of the leading improvements for PSCs is to replace a liquid electrolyte material with a solid HTL of spiro–OMeTAD.[1,2] Spiro–OMeTAD can work well for current high–performance PSCs because of its high glass transition temperature (T_g = 121 °C), high solubility, and smooth film formation associated with the amorphous nature.[3] Unfortunately, its chemical additives, which are used to enhance σ, cause degradation in PSCs by the combination of LiTFSI and molecular oxygen or the migration of LiTFSI through pinholes in the doped spiro–OMeTAD HTL under air exposure.[4][5] Moreover, the degradation of a perovskite material is initiated when devices are exposed to ambient conditions.[6,7] It has been reported that the co–presence of light and oxygen induces a deprotonation reaction of the methylammonium cation, leading to the formation of gaseous methylamine, and superoxide species with byproducts including PbI_2, PbO_x, I_2, etc.[8–10] However, the precise reasons for oxygen–induced degradation in PSCs remain undetermined.

In this chapter, I focused on investigating the impact of ambient air exposure on long–term device durability to elucidate the details of PSC degradation mechanisms. It was found that the hole–transport energy level deepening in the spiro–OMeTAD HTL under air exposure accelerated the degradation of PSCs because of the formation of a hole extraction barrier at the perovskite / spiro–OMeTAD interface. The oxygen–induced increase in the hole extraction barrier has not clearly been discussed to date while chemical doping with LiTFSI or other dopants reportedly causes the hole transport level of the HTL to modulate.[11–13] Additionally, no detectable change was observed in perovskite film quality after ~600 h of air exposure, indicating that there was no serious degradation of the perovskite absorber, although self–improvement of performances of PSCs has been observed due to an intrinsic change of perovskite materials after aging in the absence of oxygen in the environment.[14,15] In this work, oxygen–induced degradation of PSCs was reversed by storing PSCs in a vacuum overnight because of the oxygen removal from the spiro–OMeTAD HTL. These findings are crucial for a better understanding of PSC degradation in air, as well as for developing more air–stable PSCs in the future.

2.2 Results and Discussion

PSCs with the cesium–containing triple cation mixed perovskite layer, which is known to have high PCE and reproducibility, were prepared to study their air durability. The perovskite composition was $Cs_{0.05}(FA_{0.85}MA_{0.15})_{0.95}Pb(I_{0.85}Br_{0.15})_3$. The planar PSC architecture was chosen in this study as shown in **Figure 2–1a**, which was glass substrate / indium tin oxide (ITO; ~100 nm) / SnO_2 (~30 nm) / perovskite (~650 nm) / chemically doped spiro–OMeTAD (~150 nm) / Au (~70 nm). The spiro–OMeTAD HTL was chemically doped with LiTFSI, 4–tBP, and FK–209. The detailed PSC fabrication conditions are described in the experimental section. A cross–sectional scanning electron microscope (SEM) image of PSCs is shown in **Figure 2–1b**, showing that the individual layers were properly stacked to form PSCs.

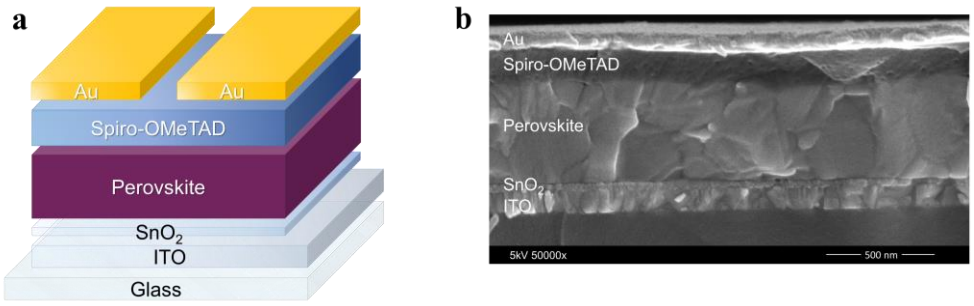

Figure 2–1. (a) Architecture scheme and (b) cross–sectional SEM image of PSCs used in this study.

To evaluate the performance of the fabricated PSCs, current density–voltage (*J*–*V*) characteristics were measured under the AM1.5G simulated solar illumination (1 sun). *J*–*V* curves of fresh PSCs, which were measured in the consecutive forward (negative to positive) and reverse (positive to negative) voltage scans, are shown in **Figure 2–2a**. In the forward scan, the J_{SC} was 24.3 mA cm^{-2}, the V_{OC} was 1.11 V, the FF was 0.67, and the PCE was 18.1%. In the reverse scan, the J_{SC} was 24.2 mA cm^{-2}, the V_{OC} 1.10 V, the FF was 0.65, and the PCE was 17.4%. All the parameters are summarized in **Table 2–1**. The forward scan was slightly better than the reverse scan in terms of the device performance. A maximum power point tracking method was used to obtain temporal PCE evolution (**Figure 2–2b**). PCEs became constant and stabilized at ~18 % within several seconds immediately after the illumination began. This stabilized PCE value was in good agreement with that measured from the *J*–*V* curves. Additionally, the short–circuit current density (J_{SC}) value was calculated as 24.0 mA cm^{-2} from the integration of an incident–photon–to–current efficiency (IPCE) curve (**Figure 2–2c**), which is not largely different from that

estimated from the *J*–*V* curve. The bandgap calculated from the IPCE onset shown in the inset of **Figure 2–2c** was ~1.56 eV, which agrees with the literature.[16]

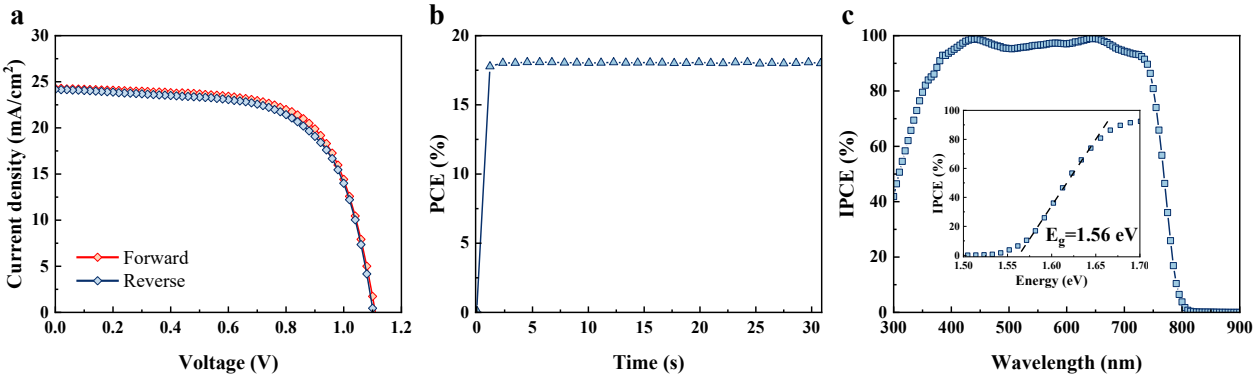

Figure 2–2. (a) *J*–*V* curves, (b) PCE evolution, and (c) IPCE curve of PSCs. The bandgap calculated from the IPCE onset was ~1.56 eV [see the inset of (c)].

Table 2–1. Summary of device parameters measured in the forward and reverse voltage scans.

Scan direction	J_{SC} (mA cm^{-2})	V_{OC} (V)	FF	PCE (%)
Forward	24.3	1.11	0.67	18.1
Reverse	24.2	1.10	0.65	17.4

After *J*–*V* measurement, the devices were kept without encapsulation in ambient air with a relative humidity of 25% at room temperature (15–20 ºC) in the dark (without illumination). *J*–*V* measurements were periodically conducted on the PSCs for over 600 h to evaluate their air durability. **Figure 2–3** shows the *J*–*V* curves of PSCs operating under the 1 sun condition. As shown in **Figure 2–3b**, J_{SC}, V_{OC}, and FF of PSCs gradually decreased over time under the ambient air. Thus, overall PCEs decreased from ~18.25% to ~15.28% by about 20% after 600 h of air exposure. The decrease in J_{SC}, V_{OC}, and FF is partly related to the hole extraction barrier increasing with oxygen doping into spiro–OMeTAD, which will be discussed later. Another reason for the V_{OC} decrease is a non–radiative energy loss arising from the quenching of perovskite excited states with oxygen. Nandayapa *et al*. revealed that oxygen could receive an electron from the perovskite and quench its excited state.[17]

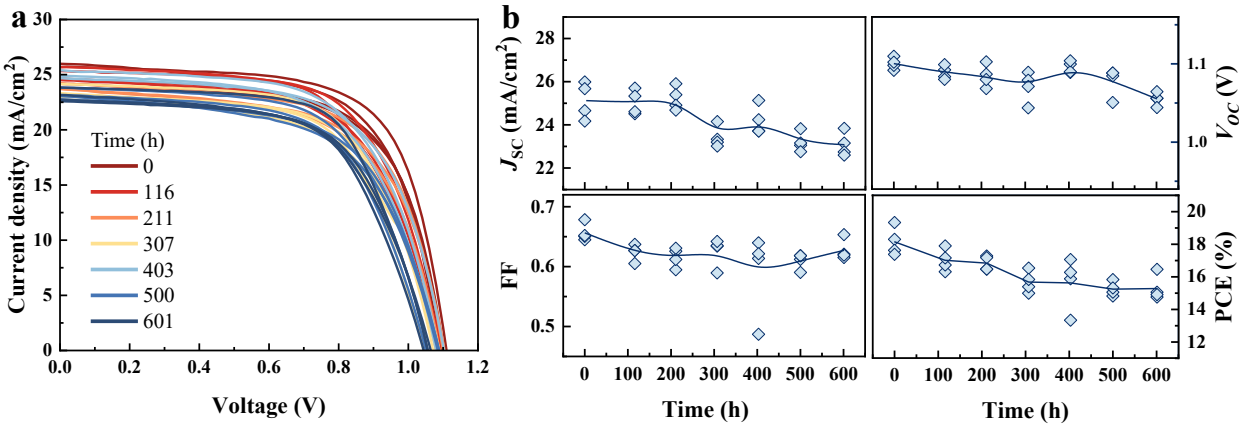

Figure 2–3. (a) *J–V* curves of PSCs. PSCs were stored in ambient air without light exposure, and their *J–V* curves were periodically measured under the 1 sun condition in the forward scan from negative to positive voltages. (b) Evolution of J_{SC}, V_{OC}, FF, and PCE of PSCs, which were obtained from (a), as a function of air exposure duration of time. The solid lines in (b) correspond to the mean values.

To clarify the reduced performance of the devices in air, transient photovoltage (TPV) decay curves of PSCs were measured under the irradiation of 337–nm pulsed excitation light, with a pulse width of 3.5 ns and a power of 170 μJ pulse^{-1}, from a nitrogen laser using an oscilloscope in the form of voltage across a resistor with 100 kΩ (**Figure 2-4**). With this high resistance, the operation condition of PSCs is close to the open circuit (no current flow), so obtained TPV signals could provide information on the recombination of the electrons and holes in the PSCs. Normally, slower TPV decays mean suppressed charge recombination in PSCs and *vice versa*.

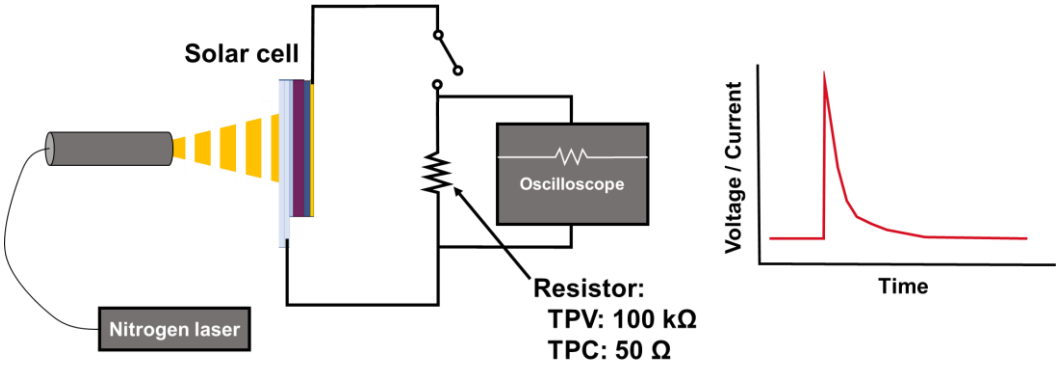

Figure 2-4. Schematic diagram of TPV and TPC measurements.

The TPV results are shown in **Figure 2–5a**. The TPV lifetimes, at which the photovoltage decreases to 1/e of the initial value, are plotted in **Figure 2–5b**. The figure shows the almost independent relationship between the TPV lifetimes and the air exposure. This indicates that the charge recombination remains nearly unchanged, which, however, does not agree with the V_{OC} decrease mentioned earlier. In general, the increased charge recombination decreases the quasi–Fermi level splitting and, therefore, makes V_{OC} lower.[18] Unknown mechanisms that affect the V_{OC}

decrease still exist and need to be clarified in the future. Therefore, it can only be speculated that carrier recombination has little impact on the PSC performance even after the air exposure since the V_{OC} decrease is small and the TPV lifetimes are similar. As will be discussed later, the perovskite layer itself does not degrade seriously in air, which seems consistent with the unchanged charge recombination behavior observed here.

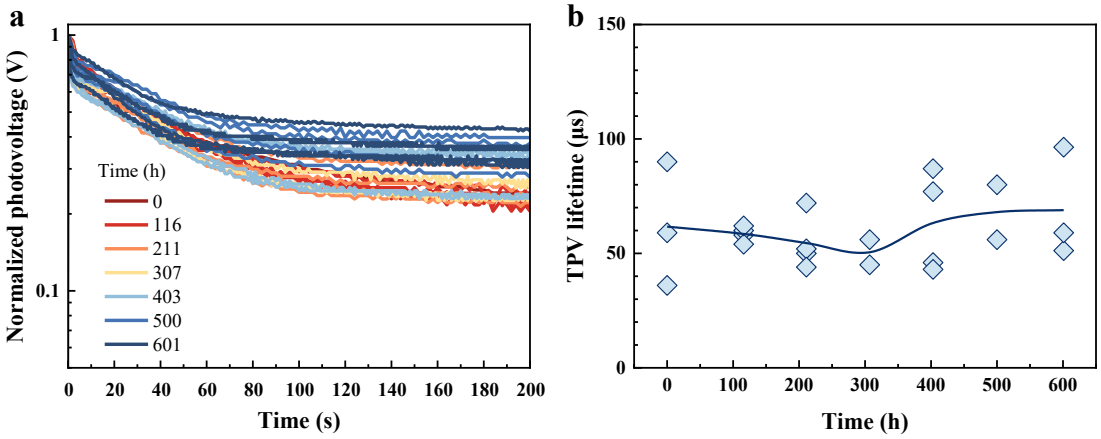

Figure 2–5. (a) TPV decay curves and (b) TPV lifetimes of PSCs when stored in ambient air. The solid lines in (b) correspond to the average values.

Next, transient photocurrent (TPC) measurements were carried out on the same PSCs at each degradation level (**Figure 2-6a**) using the same setup except the resistance was low at 50 Ω (**Figure 2–4**). With this low resistance, PSCs are nearly under the short–circuit condition. TPC lifetimes, which were calculated in the same way that was used for the TPV lifetimes estimation (1/e of the initial value), likely increased as the air exposure duration was increased as shown in **Figure 2–6b**. This corresponds to a reduction of carrier extraction for air–stored devices. Therefore, I believe that the PSC degradation in air originates from the reduced carrier extraction.

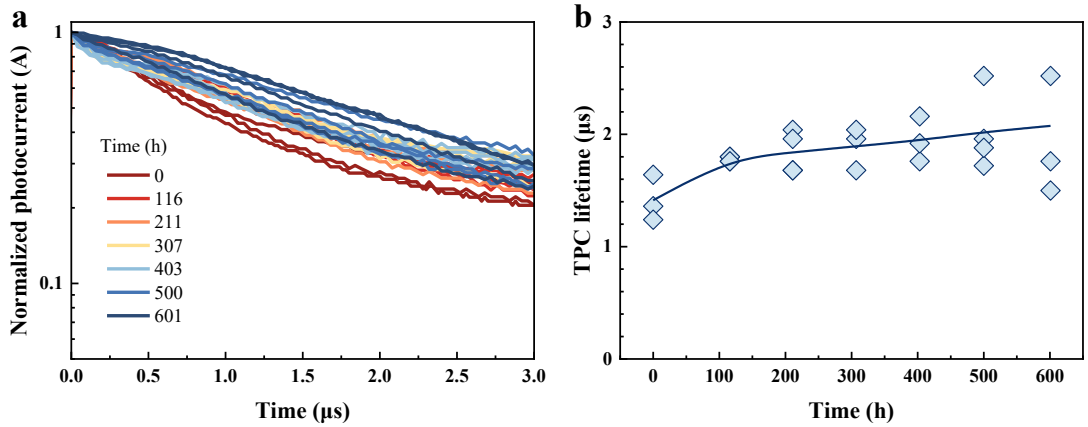

Figure 2–6. (a) TPC decay curves and (b) TPC lifetimes of PSCs when stored in ambient air. The solid lines in (b) correspond to the mean values.

There are several possible reasons for the reduced carrier extraction: water–induced phase segregation of spiro–OMeTAD, accumulation of Li salt in spiro–OMeTAD, halide ions, or oxygen doping into spiro–OMeTAD.[19–24] Among them, oxygen plays a key role in the degradation in air, and several papers describing the relationship between spiro–OMeTAD and oxygen have been reported.[20,21,25] To prove that, the charge carrier transport studies were carried out on doped spiro–OMeTAD–based hole–only devices (HODs) with and without MoO_3 as an interlayer. Here, the HODs have the following architectures: glass substrate / ITO (100 nm) / chemically doped spiro–OMeTAD (~150 nm) / Au (~70 nm) and glass substrate / ITO (100 nm) / chemically doped spiro–OMeTAD (~150 nm) / MoO_3 (~10 nm) / Au (~70 nm). The detailed HOD fabrication conditions are mentioned in the experimental section. It is noted that a resulting oxide film prepared by vacuum deposition reportedly contains many oxygen vacancy defects (x = 2.7 in MoO_x).[26]

J–V curves of HODs without and with MoO_3, where the holes were injected into spiro–OMeTAD from the Au side, are shown in **Figures 2–7a** and **b,** respectively. Inserting MoO_3 between the spiro–OMeTAD layer and the Au layer increased the current densities. The Fermi level of Au is –4.76 eV (**Figure 2–8a**) and the hole transport levels of the doped spiro–OMeTAD layers range from –5.24 eV and –5.63 eV, which are dependent upon the oxygen doping levels as will be discussed later.

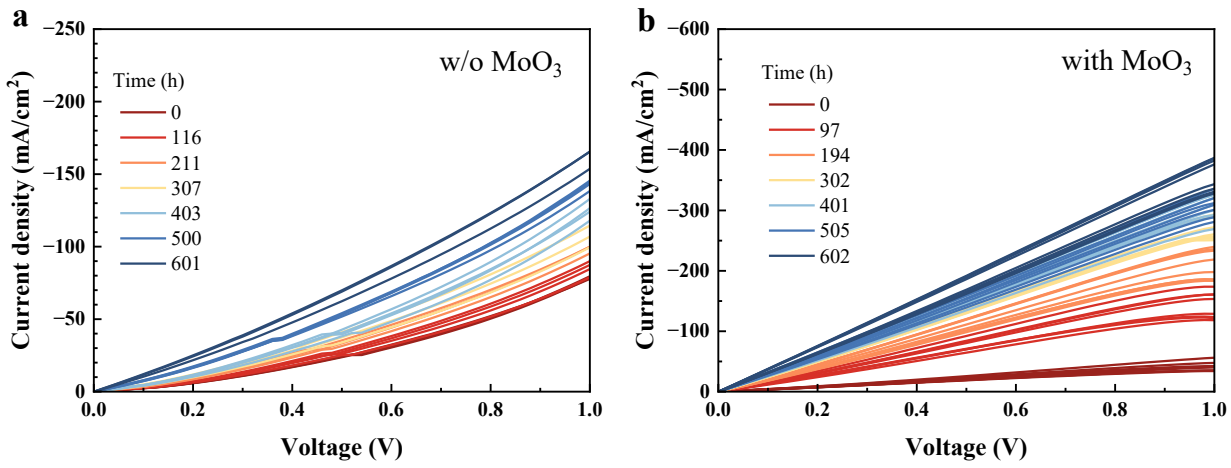

Figure 2–7. *J–V* curves of spiro–OMeTAD–based HODs without (a) and with (b) MoO_3. These *J–V* curves were measured under the dark condition.

There is a hole injection barrier between the Au layer and the doped spiro–OMeTAD layer in HODs. This hole injection barrier may be reduced by using MoO_3, which has a high work function of 5.94 eV (**Figure 2–8b**) and is known as an excellent hole injection layer in organic devices.[26] This high work function might be the reason behind the higher current densities with

MoO_3. Note that the energy levels of Au, doped spiro–OMeTAD, and MoO_3 were measured using photoelectron yield spectroscopy (PEYS). The ITO layer was electrically grounded to avoid the sample layer from surface charge–up.

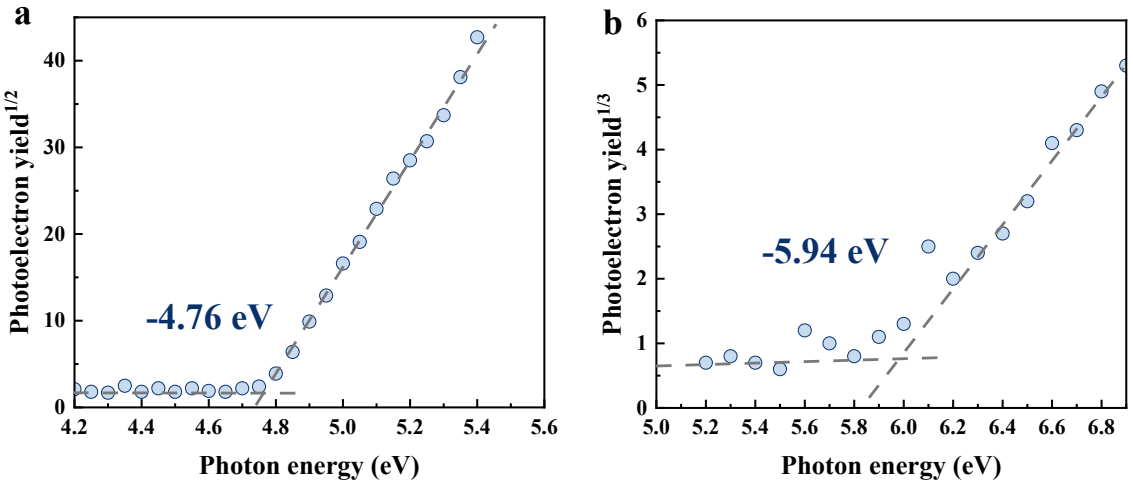

Figure 2-8. PEYS result of the (a) Au layer and (b) MoO_3 layer.

The σ was roughly estimated from the slope of each *J–V* curve between 0 and 1 V although a bend was somewhat observed in the *J–V* curves. An increase in σ in both HODs was confirmed as the air exposure duration was extended (**Figure 2–9**). I believe that the electrical conductivities measured from HODs with MoO_3 correspond to more intrinsic bulk carrier transport in the doped spiro–OMeTAD layer. As reported previously, the observed σ increase after the air exposure would be due to oxygen doping into spiro–OMeTAD.[27] LiTFSI is a commonly used dopant in spiro-OMeTAD to increase the concentration of oxidized spiro-OMeTAD$^+$, which shifts its Fermi level closer to the HOMO.[28] Hawash *et al*. also showed that the concentration of oxidized spiro-OMeTAD$^+$ in LiTFSI-doped films increases over time when exposed to air.[5] However, Wang *et al*. demonstrated that spiro–OMeTAD is oxidized by oxygen with assistance of photons in a short wavelength range. Consequently, superoxide radical O_2^- reacts with Li^+ to form Li_xO_y and finally spiro–O MeTAD$^{\cdot+}$TFSI$^{\cdot-}$ is generated.[27] The reaction is described as follows:

$$\text{Spiro} - \text{OMeTAD} + \text{O}_2 \xrightarrow{h\nu\ (380-450\ \text{nm})} \text{Spiro} - \text{OMeTAD}^{\cdot+}\ \text{O}_2^{\cdot-}$$

$$\text{Spiro} - \text{OMeTAD}^{\cdot+}\ \text{O}_2^{\cdot-} + \text{LiTFSI} \rightarrow\ \text{Spiro} - \text{OMeTAD}^{\cdot+}\ \text{TFSI}^{\cdot-} + \text{Li}_x\text{O}_y$$

Therefore, photodoping and exposure to oxygen are commonly used to promote the oxidation of spiro–OMeTAD, enhancing the performance of PSCs.[29,30] However, those methods are difficult to control, leading to poor reproducibility in device performance. Therefore, in this research, FK209 dopant was used alongside LiTFSI and 4*t*BP, as it has been shown to significantly oxidize

spiro–OMeTAD even under dark conditions.[31] I believe an increase in σ of HODs indicates that oxygen further increases the concentration of oxidized spiro-OMeTAD$^+$, even when a strong combination of LiTFSI, FK209, and 4*t*BP dopants is used for p-doping in the spiro-OMeTAD film.

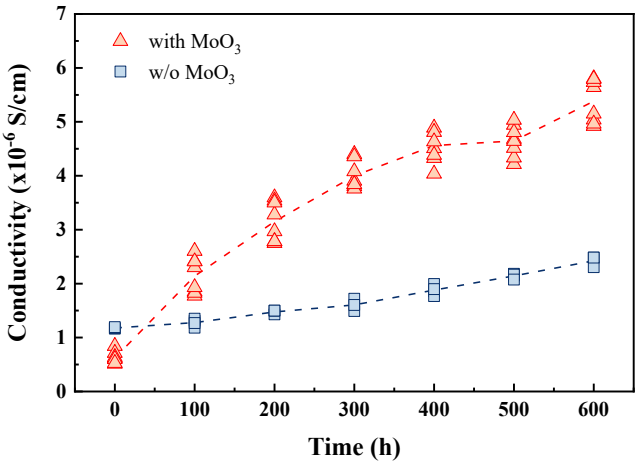

Figure 2–9. Plots of the electrical conductivities of HODs with and without MoO_3 as a function of air exposure duration.

To further investigate the effect of air exposure on the spiro–OMeTAD HTL, I measured the hole transport energy levels of the chemically doped spiro–OMeTAD layers fabricated on top of an ITO–coated glass substrate by using PEYS. Additionally, the VB edge level of perovskite thin film was measured as –5.33 eV with the same method as mentioned above (**Figure 2–10**).

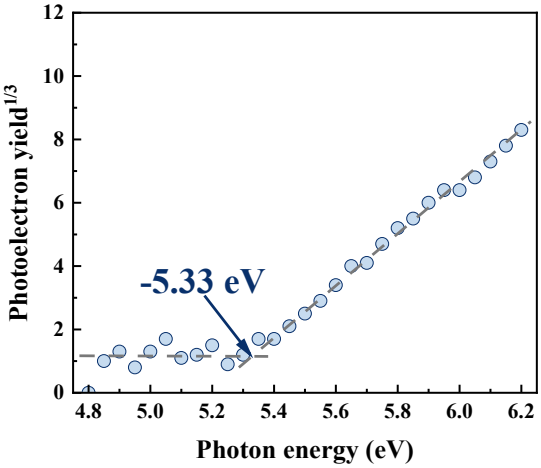

Figure 2–10. PEYS result of the perovskite layer.

The initial hole transport energy level of the chemically doped spiro–OMeTAD layer just after the fabrication was −5.24 eV (**Figure 2–11a**). This value is consistent with the literature[2] and closer to the VB of the perovskite layer, which is beneficial to the hole extraction from the perovskite layer to the spiro–OMeTAD HTL. However, their hole transport levels deepened to –

5.46 eV, –5.50 eV, –5.53 eV, –5.87 eV, –5.6 eV, and −5.63 eV after storing spiro–OMeTAD in air at room temperature for 116 h, 211 h, 307 h, 403 h, 500 h, and 601 h, respectively (**Figure 2–11b–g**). **Figure 2–11h** summarizes a change of the hole transport levels of spiro–OMeTAD. A similar energy–level deepening by chemical or oxygen doping has been reported by other groups.[32,34,47,48] The deeper hole transport level of spiro–OMeTAD leads to the formation of an energy barrier for the hole extraction. The energy–level alignment between the perovskite layer and the HTL is crucial to achieving better performance and long–term durability.[33] A larger discrepancy between the VB level of the perovskite and the hole transport level of the HTL decreases the V_{OC} in PSCs because of a hole transport loss.[34] Thus, It can be concluded that the degradation of the PSC performances observed in **Figure 2–3** originates from the decreased hole extraction from the perovskite layer to the spiro–OMeTAD layer. The negative influence of the decreased hole extraction outweighs the benefit of the increased σ for PSCs. The metal electrode diffusion into the spiro–OMeTAD HTL and the Li ions migration into the perovskite layer reportedly affect the PSC performance.[35,36] However, the hole transport levels shown in **Figure 2-11** were measured from the samples without the metal electrode and the perovskite layer.

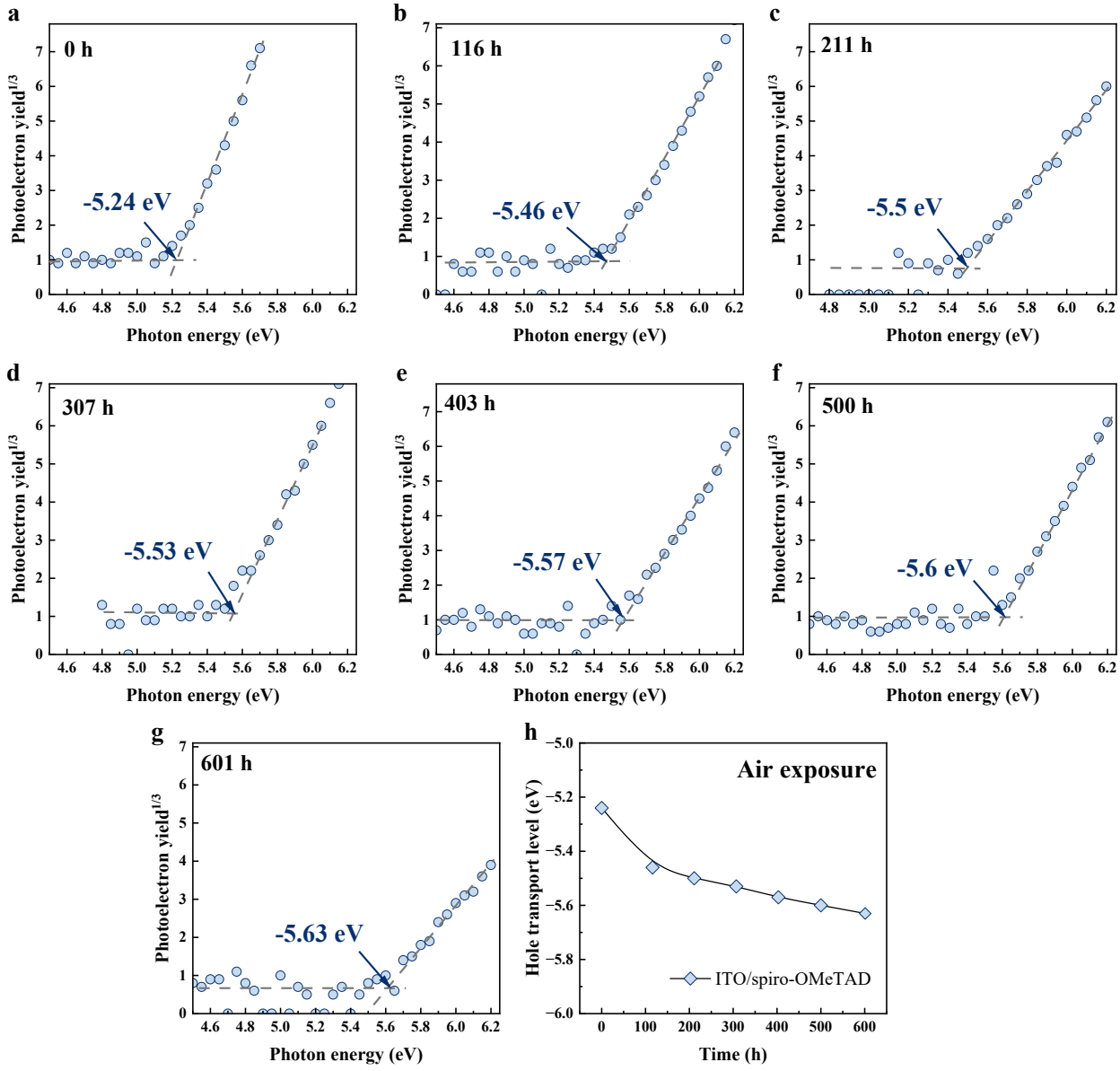

Figure 2–11. PEYS results of spiro–OMeTAD films (a) before and (b−g) after 116, 211, 307, 403, 500, or 601 h of the air exposure. (h) Plot of the hole transport levels of spiro–OMeTAD as a function of air exposure duration of time.

To investigate the effect of water on the hole transport level of spiro–OMeTAD, a chemically doped spiro–OMeTAD layer was fabricated on top of an ITO–coated glass substrate and stored in humid nitrogen at a relative humidity of ~30% and a temperature of ~25 °C. As shown in **Figure 2–12**, hole transport energy levels of these samples became deeper by ~0.1 eV after 600 h of the humid nitrogen storage, indicating that H_2O interacts with the spiro–OMeTAD HTL. For example, hygroscopic LiTFSI attracts water molecules, which leads to agglomeration of LiTFSI and results in HTL degradation.[5,37] Additionally, the incorporation of water drastically affects the oxidation and electronic structure of spiro–OMeTAD.[19,20,37]

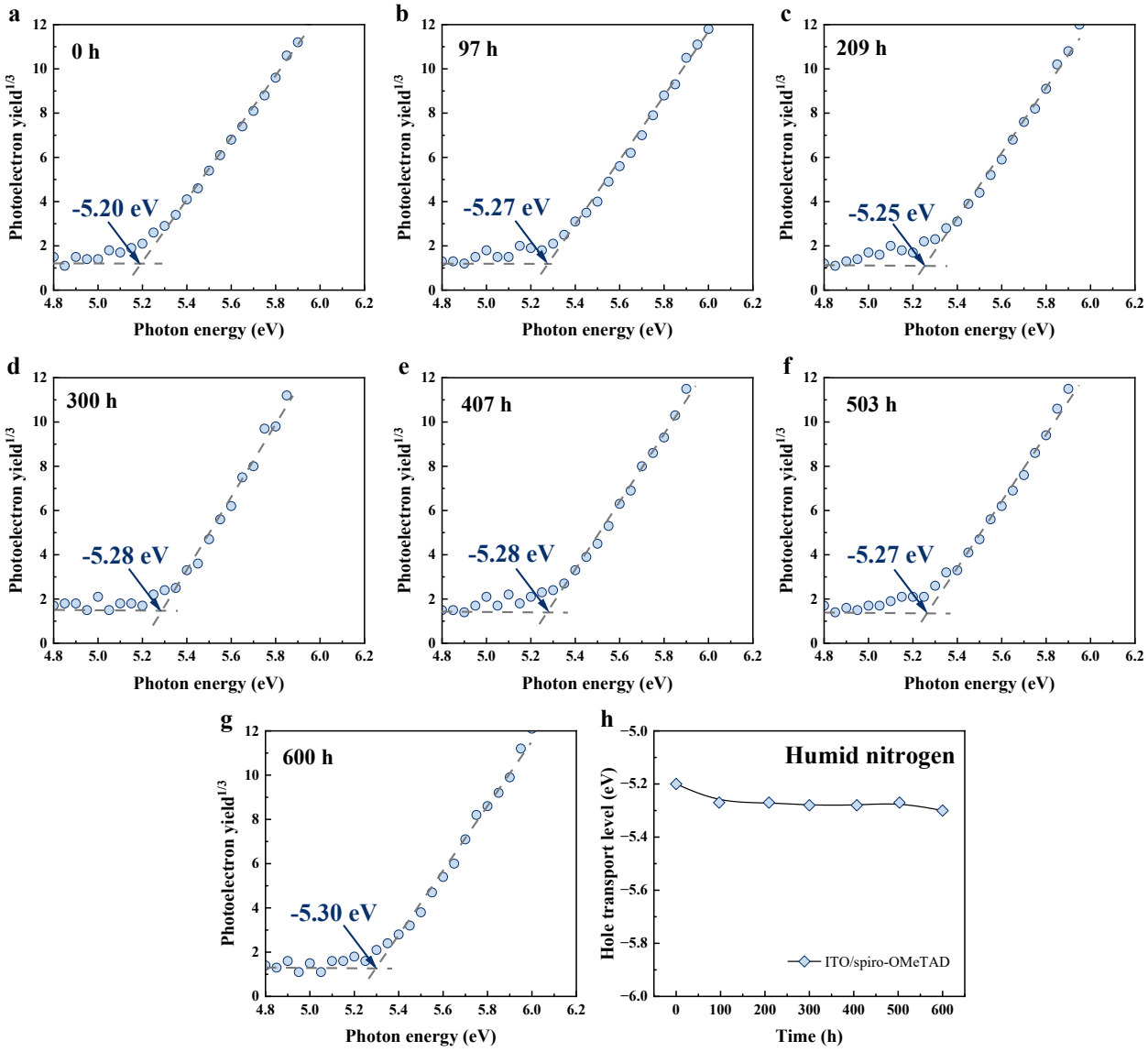

Figure 2–12. PEYS results of samples with an architecture of glass substrate / ITO / chemically doped spiro–OMeTAD (a) before and (b−g) after 97, 209, 300, 407, 503, or 600 h of the exposure to humid nitrogen. (h) Summary plot of hole transport levels as a function of humid nitrogen exposure duration of time.

Samples with an architecture of glass substrate / ITO / perovskite / chemically doped spiro–OMeTAD were fabricated and stored in pure nitrogen to clarify how iodine coming from the perovskite layer affects the electronic state of spiro–OMeTAD. The results showed that hole transport energy levels deepened by ~0.15 eV after ~600 h of the pure nitrogen storage (**Figure 2–13**). Several reports have shown that halide ions (iodine in this case) from the perovskite layer can permeate through the HTL, which facilitates the generation of spiro–OMeTAD^{+} cations.[22,38,39] The iodine doping process affects the energy level and interfacial charge collection yield, which

then decreases the charge extraction. Therefore, the energy level shift observed here indicates the iodine migration into spiro–OMeTAD.

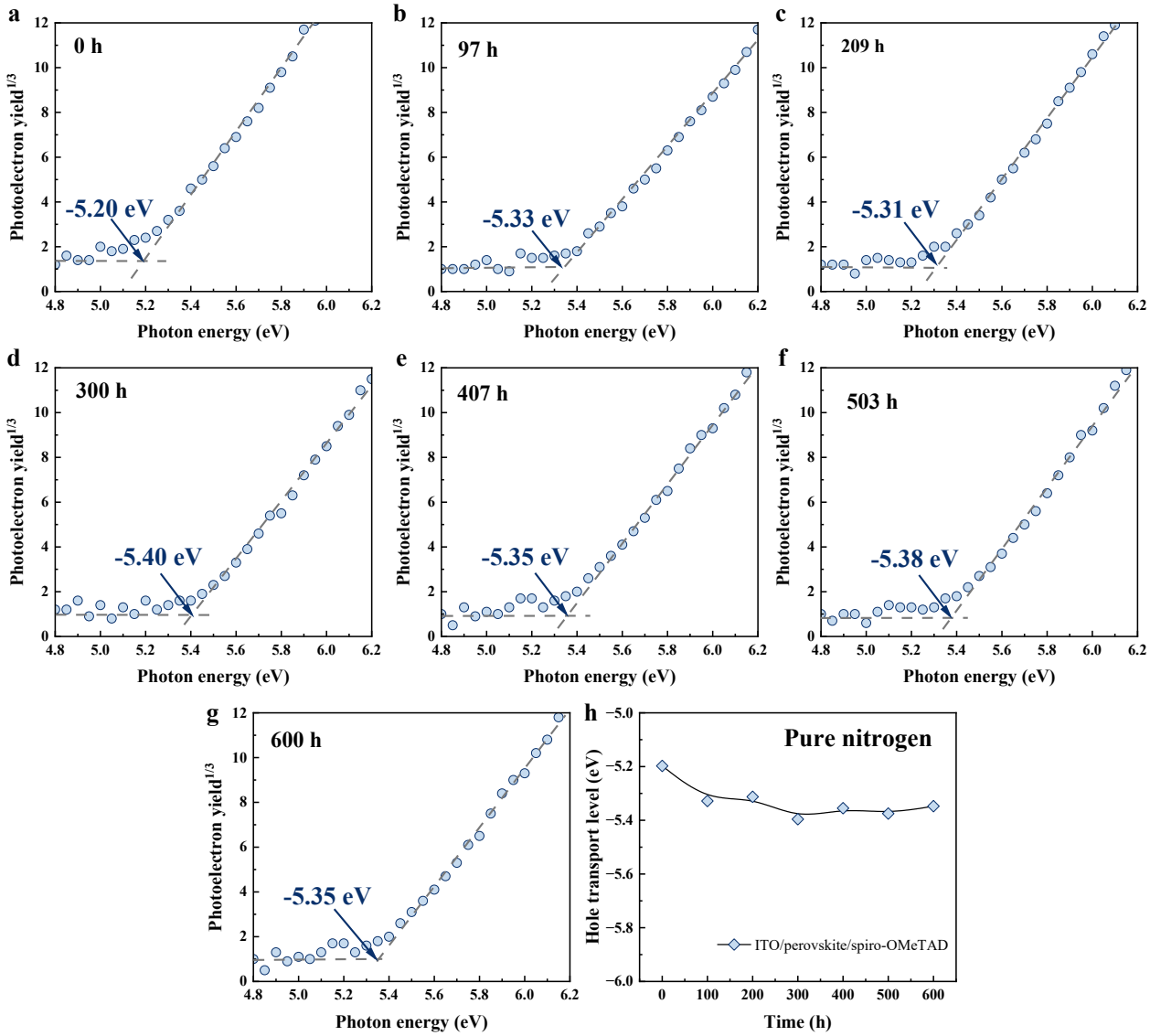

Figure 2–13. PEYS results of samples with an architecture of glass substrate / ITO / perovskite / chemically doped spiro–OMeTAD (a) before and (b−g) after 97, 209, 300, 407, 503, or 600 h of the exposure to pure nitrogen. (h) Summary plot of hole transport levels as a function of pure nitrogen exposure duration of time.

Next, I stored samples with an architecture of glass substrate / ITO / perovskite / chemically doped spiro–OMeTAD in humid nitrogen with a relative humidity of ~30%. A slightly larger shift in the hole transport energy level of spiro–OMeTAD by ~0.17 eV was observed (**Figure 2–14**), indicating that both water and iodine make the hole transport level deeper. Based on the aforementioned results, it is concluded that not only oxygen but also water and iodine cause the energy–level shifts. However, oxygen is more influential for the energy–level shifts than water and iodine.

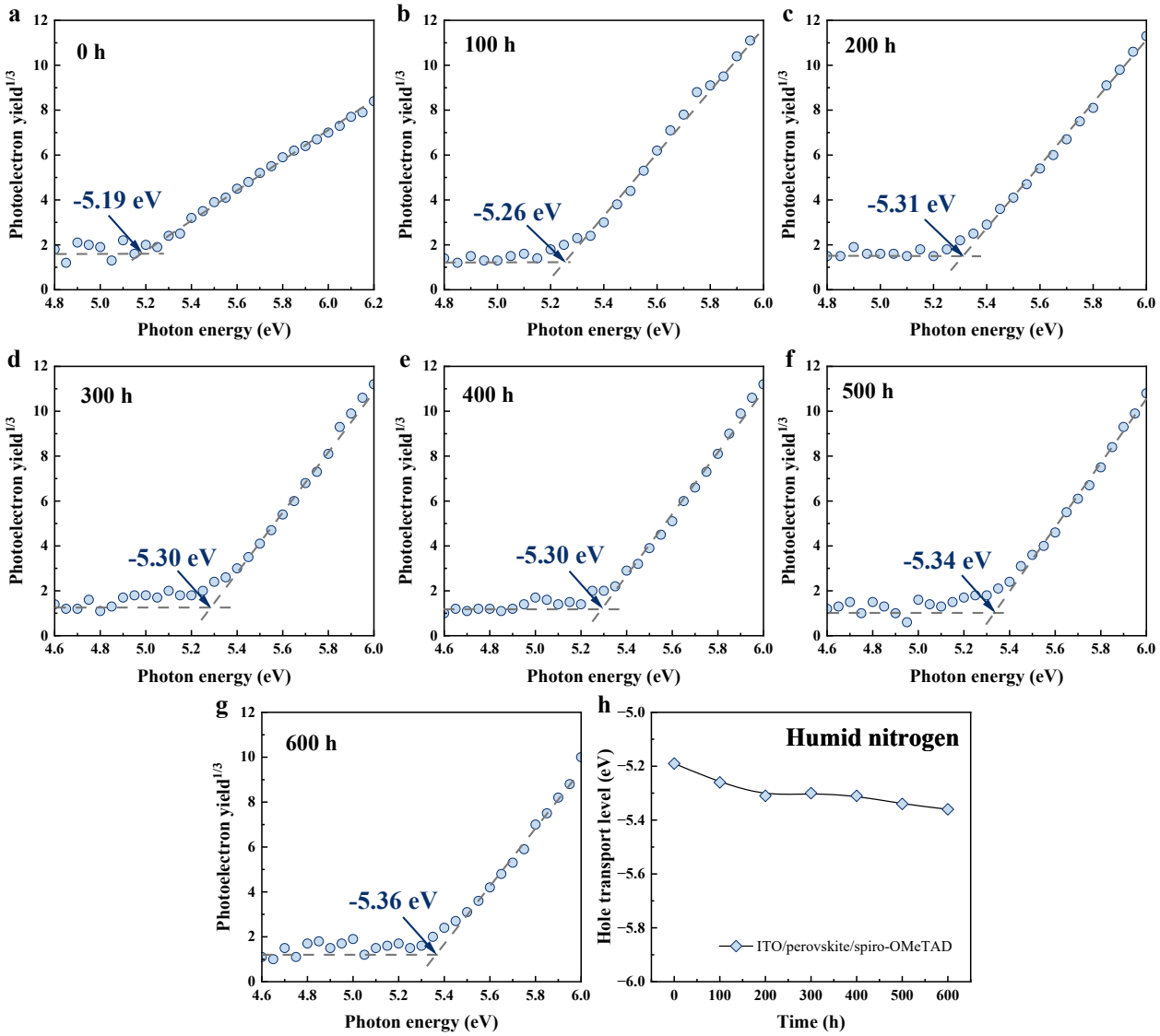

Figure 2–14. PEYS results of samples with an architecture of glass substrate / ITO / perovskite / chemically doped spiro–OMeTAD (a) before and (b−g) after 100, 200, 300, 400, 500, or 600 h of the exposure to humid nitrogen. (h) Summary plot of hole transport levels as a function of humid nitrogen exposure duration of time.

As mentioned earlier, the hole transport level of the doped spiro–OMeTAD HTL, which was fabricated directly on ITO without the perovskite layer and exposed to air for 600 h, was −5.63 eV while it was 5.24 eV before the air exposure. Surprisingly, the energy level became shallower at −5.48 eV by ~0.15 eV from −5.63 eV after the ~600 h air–exposed sample was stored in a vacuum overnight (**Figures 2–15a** and **b**). I mainly attribute this reversible behavior to the degasification of oxygen from the spiro–OMeTAD layer. However, the hole transport level of spiro–OMeTAD did not recover to the initial value (−5.24eV) because of the incomplete removal of the oxygen from the film interior.

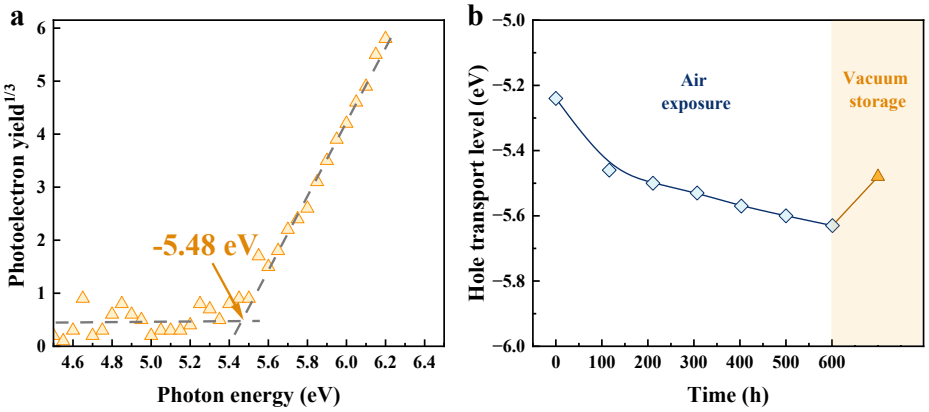

Figure 2–15. (a) PEYS results of vacuum–stored spiro–OMeTAD HTL. (b) Plot of the hole transport levels of spiro–OMeTAD as a function of air exposure duration of time. The yellow triangle symbol in (b) indicates the recovered hole transport level by storing the sample in a vacuum overnight.

Additionally, highly volatile 4–tBP may evaporate during the vacuum storage, which might induce an energy–level change in spiro–OMeTAD. Therefore, I measured a hole transport energy level of spiro–OMeTAD films doped with LiTFSI and FK209 only (without 4–tBP). Its hole transport energy level was very deep at −5.7 eV as shown in **Figure 2–16**, which is contrary to the energy level shallowing after the vacuum storage. Hence, the 4–tBP evaporation is not so influential. It has been reported that a LiTFSI/4–tBP complex is formed in spiro–OMeTAD films, which may make the chemical doping of spiro–OMeTAD with LiTFSI difficult.[40] Therefore, in films without 4–tBP, a stronger chemical doping may happen, leading to a very deep energy level as shown in **Figure 2-16**.

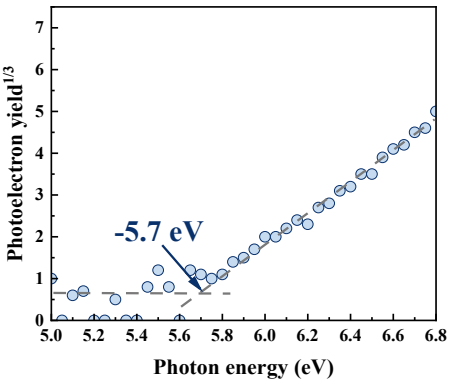

Figure 2–16. PEYS result of LiTFSI– and FK209–doped spiro–OMeTAD films (without 4–tBP).

To see how the degasification of oxygen affects the PSC performance, I placed the PSCs, which were stored in air for 600 h, in a vacuum overnight. *J–V* curves of PSCs before and after the vacuum storage are shown in **Figure 2–17**. The inset of this figure summarizes individual device performance parameter values obtained. Storing air–exposed PSCs in a vacuum increased J_{SC}, V_{OC}, and FF. Therefore, the overall PCEs also increased from ~15.3% to ~16.9%. However, this PCE

(~16.9%) was lower than that of fresh PSCs (~18.2%). This incomplete performance recovery again indicates the incomplete removal of oxygen and the existence of other degradation mechanisms in PSCs.

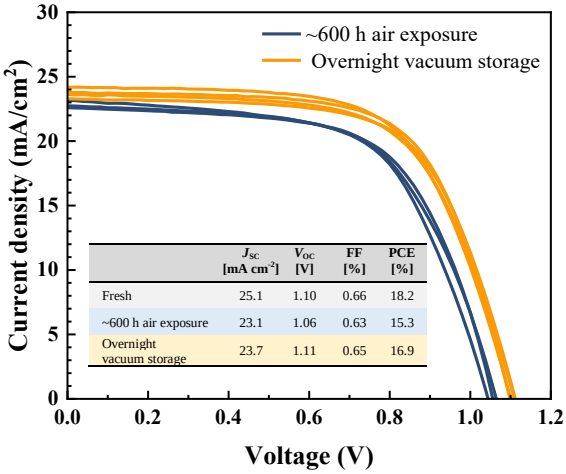

	J_{SC} [mA cm^{-2}]	V_{OC} [V]	FF [%]	PCE [%]
Fresh	25.1	1.10	0.66	18.2
~600 h air exposure	23.1	1.06	0.63	15.3
Overnight vacuum storage	23.7	1.11	0.65	16.9

Figure 2–17. *J–V* curves of PSCs before and after the overnight vacuum storage. The inset is a table summarizing the mean photovoltaic parameters. The mean parameters of fresh PSCs are also shown in the inset for comparison.

The question here is how oxygen or water molecules can reach the spiro–OMeTAD HTL, which is covered with the Au electrode. As can be seen in an SEM image shown in **Figure 2–18**, vacuum–deposited Au films have a grain structure. I assume that the oxygen molecules can penetrate through the Au grain boundaries, followed by the oxygen doping into the HTL. Additionally, the oxygen doping likely proceeds from the HTL surface to the HTL interior. Therefore, the hole transport levels discussed earlier and measured from the HTL surfaces using PEYS would be deeper than those near the perovskite surface of the opposite side.

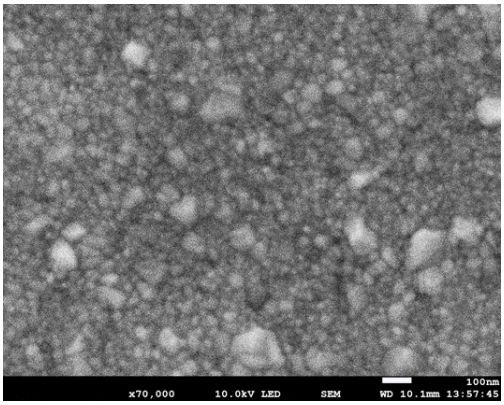

Figure 2–18. Top–view SEM image of an 80–nm–thick Au layer evaporated on the spiro–OMeTAD layer.

To observe the presence of oxygen in the spiro–OMeTAD HTL, X–ray photoelectron spectroscopy or secondary ion mass spectrometry might be a useful method. However, these

methods use an ultra–high vacuum condition to detect atoms, which is not suitable for my samples because oxygen may be released from the film in the vacuum, as discussed earlier. Therefore, to confirm if the oxygen doping happens, the hole transport energy levels were simply measured on spiro–OMeTAD films when stored in pure nitrogen. As shown in **Figure 2–19**, the hole transport levels were unchanged after 600 h of pure nitrogen storage. This is indirect evidence that the oxygen doping deepens the hole transport levels.

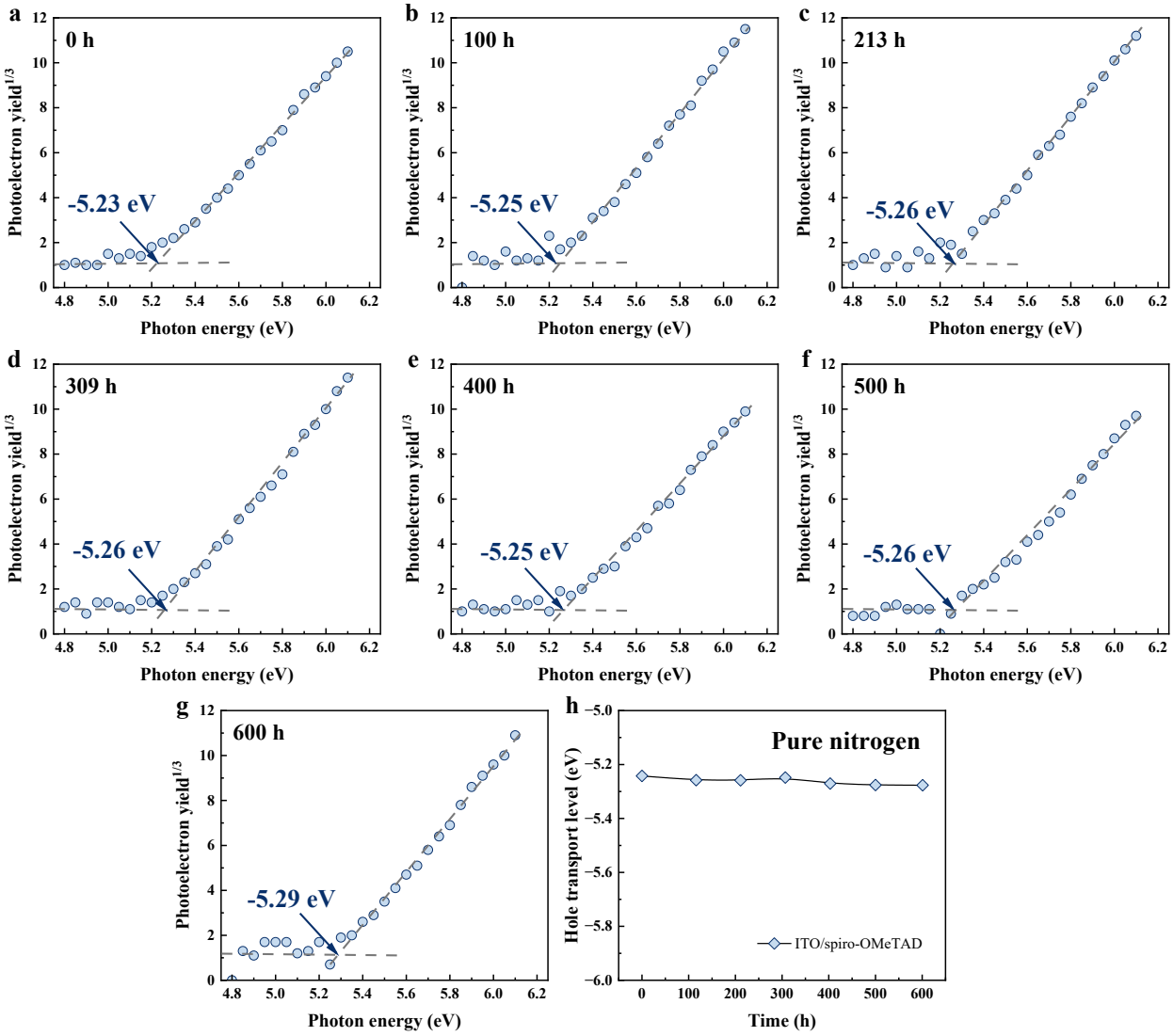

Figure 2–19. PEYS results of samples with an architecture of glass substrate / ITO / chemically doped spiro–OMeTAD (a) before and (b−g) after 100, 213, 309, 400, 500, or 600 h of the exposure to pure nitrogen. (h) Summary plot of hole transport levels as a function of nitrogen exposure duration of time.

Additionally, Fourier transform infrared (FTIR) spectroscopy was used to investigate the oxygen doping into spiro–OMeTAD. Unfortunately, no change was observed in FTIR spectra of chemically doped spiro–OMeTAD films before and after the 600 h air storage (**Figure 2–20**). From the electrical conductivities shown in **Figure 2–8**, the ratios of the spiro–OMeTAD^{+} cation number to the neutral spiro–OMeTAD species number were calculated to be ~0.005% for films before the

air storage and ~0.011% for films after the 600 h air storage (see details in Appendix **A–1**). These ratio values may be underestimated because such devices frequently suffer from the presence of contact resistance. Based on the calculated ratios, I assume that the number of spiro–OMeTAD^{+} cations formed by the oxygen doping is too small to detect with FTIR measurements.

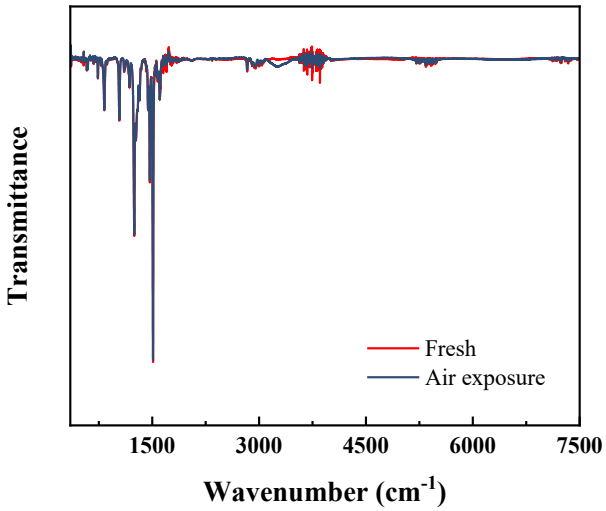

Figure 2–20. FTIR spectra of chemically doped spiro–OMeTAD films, which were measured before and after 600 h air exposure.

Moreover, I used a quartz crystal microbalance (QCM) method to prove the oxygen doping into spiro–OMeTAD films. A chemically doped spiro–OMeTAD film was prepared on a gold–coated quartz crystal plate and then stored in a vacuum overnight to remove the chlorobenzene (CB) solvent used for the spiro–OMeTAD spin–coating. The initial frequency of the QCM without the film was ~9 MHz, and the frequency was decreased by ~6,800 Hz after the spiro–OMeTAD film fabrication (**Table 2–2**). Then, frequency changes were measured when the spiro–OMeTAD films were stored in pure nitrogen or dry air. **Figure 2–21** shows the plots of (f–f_0) as a function of exposure duration in pure nitrogen or dry air. Here f and f_0 are the frequencies at each exposure time and 0 h (just after the spin–coating and vacuum storage), respectively. The (f–f_0) values increased monotonically in pure nitrogen. This increase in (f–f_0) may correspond to the CB evaporation from the film. The overnight storage in the vacuum is not sufficient to completely remove the CB solvent molecules from the spiro–OMeTAD film. On the other hand, the sample stored in dry air showed a different behavior; the (f–f_0) values increased during the first ~50 h and then decreased gradually with time. The first increase in (f–f_0) is also attributed to the CB solvent evaporation from the film, and the next (f–f_0) decrease may arise from the oxygen doping into the film. Therefore, I assume that a difference in (f–f_0) between the two samples stored in nitrogen and dry air at each exposure time corresponds to the amount of oxygen molecules doped into the spiro–

OMeTAD film. The (f–f_0) difference between the two samples at 600 h was ~130 Hz. For the oxygen doping level estimation, I assume that the spin–coated film on the QCM contains spiro–OMeTAD molecules only. Considering the frequency decrease caused by the spiro–OMeTAD film fabrication (~6,800 Hz), the aforementioned (f–f_0) difference (~130 Hz), and the molecular weights of spiro–OMeTAD (1225) and O_2 (32), It can be estimated that one spiro–OMeTAD molecule had ~0.73 oxygen molecule when the film was stored in dry air for ~600 h. This doping level seems high but all oxygen molecules are not used for the hole doping considering the previously calculated spiro–OMeTAD$^+$/spiro–OMeTAD ratio (~0.011%).

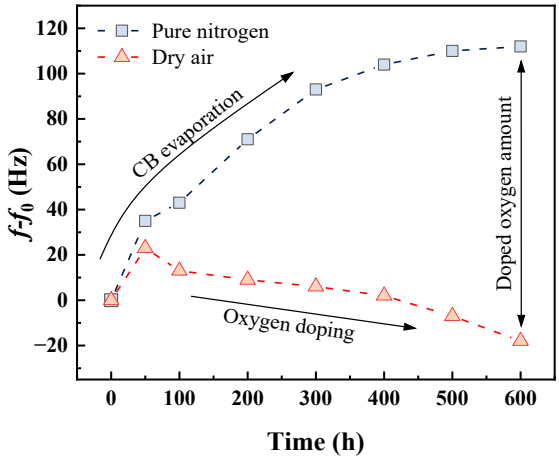

Figure 2–21. Plots of (f–f_0) values as a function of exposure duration of time (CB: chlorobenzene). Chemically doped spiro–OMeTAD films were exposed to pure nitrogen or dry air.

Table 2–2. Frequencies of the QCM coated with a chemically doped spiro–OMeTAD layer. The spiro–OMeTAD samples were stored in pure nitrogen or dry air.

Time (h)	Pure nitrogen		Dry air	
	f	f−f_0	f	f−f_0
Before deposition	9,002,954	6,806	9,005,245	6,807
0 (after deposition)	8,996,148 (= f_0)	0	8,998,438 (= f_0)	0
50	8,996,183	35	8,998,461	23
100	8,996,191	43	8,998,451	13
200	8,996,219	71	8,998,447	9
300	8,996,241	93	8,998,444	6
408	8,996,252	104	8,998,440	2
504	8,996,258	110	8,998,431	−7
605	8,996,260	112	8,998,420	−18

Furthermore, UV–VIS absorption spectra of chemically doped and undoped spiro–OMeTAD films were measured (**Figures 2–22a** and **b**). Both films had absorption peaks originating from the neutral spiro–OMeTAD species in a wavelength range below 400 nm. A new absorption appeared around 500 nm in doped spiro–OMeTAD films, which has already been observed in previous work and reflects the oxidation of the neutral spiro–OMeTAD to form the radical cations spiro–OMeTAD^{+}.[13,21] Most of the reported works on these observations demonstrated that the formation of the radical cations is attributed to the additives, chemical dopants, or oxygen.[21,41,42] To further verify the oxygen doping in spiro–OMeTAD, I stored doped spiro–OMeTAD films in air for 600 h. The absorbance of the radical cation peak at ~500 nm increased after the air storage as shown in **Figures 2–22a** and **b**, indicating that oxygen–induced doping in spiro–OMeTAD occurs over a period. Therefore, I conclude that oxygen further promotes the oxidation of spiro–OMeTAD to spiro–OMeTAD^{+} radical cation, despite the presence of the strong dopant combination. The product spiro–OMeTAD^{+} O_2^{-} is a weakly bounded complex as shown below:

$$\text{Spiro} - \text{OMeTAD} + O_2 \rightarrow \text{Spiro} - \text{OMeTAD}^{\cdot +} \; O_2^{\cdot -}$$

However, the absorbance of the radical cation peak decreased after storing the sample in a vacuum overnight, indicating that oxygen was removed from spiro–OMeTAD. Similar reversible doping of spiro–OMeTAD with halide anions migrating from the perovskite layer has been reported.[39]

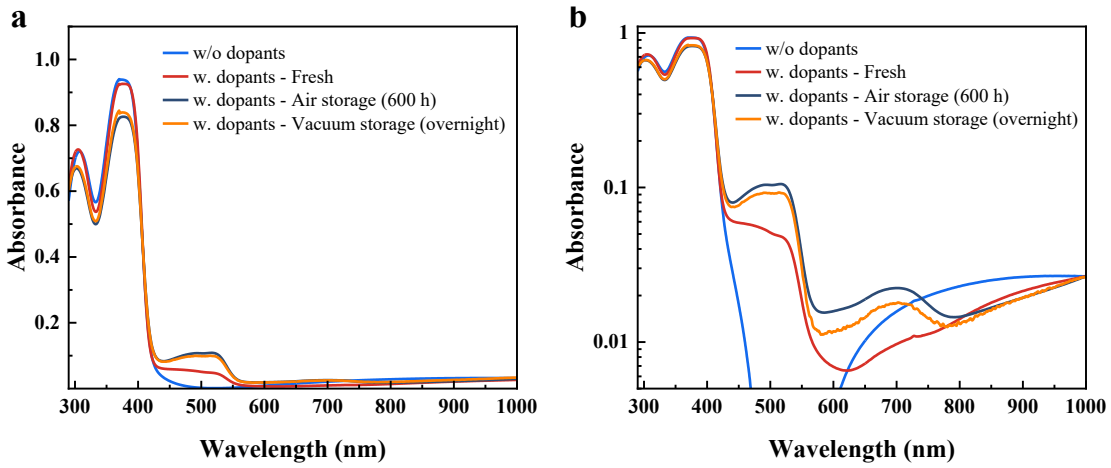

Figure 2–22. (a) Linear– and (b) logarithmic–scale UV–VIS absorption spectra of undoped and doped spiro–OMeTAD films. The doped films were exposed to air for ~600 h and then placed in a vacuum overnight.

I carried out the same air exposure test on undoped spiro–OMeTAD films. Even after 600 h of air exposure, I could not observe a radical cation absorption peak in undoped films at all

(**Figure 2–23**). Compared with chemically doped films, doped films are denser, without pinholes, so oxygen penetration into undoped films is unlikely. Therefore, the air durability of PSCs will be significantly enhanced if dopant–free HTL materials with high performance can be developed. Unfortunately, PCSs with the undoped spiro–OMeTAD HTL had a lower PCE value of ~6%.

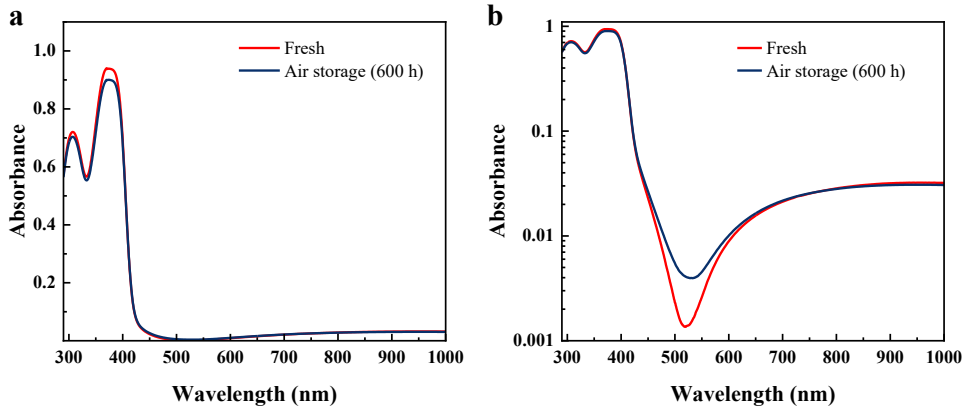

Figure 2–23. (a) Linear– and (b) logarithmic–scale UV–VIS absorption spectra of undoped spiro–OMeTAD films before and after air exposure.

It has been reported that a decrease in PCE of PSCs is related to the decomposition occurring inside perovskite materials in an oxygen environment.[43–45] Therefore, a series of additional experiments were performed to investigate the impact of oxygen on the perovskite layer. To this end, the Au electrode and spiro–OMeTAD layers were removed from PSCs before and after 600 h of air exposure and measured their UV–VIS absorption and steady–state PL spectra, SEM images, and X–ray diffraction (XRD) patterns.

UV–VIS absorption spectra of the perovskite films before and after the air exposure test were measured to investigate their optical degradation (**Figure 2–24a**). The spectral shapes agree with the literature.[46] The absorption spectra were independent of the air exposure, despite the reduced PCE after the air exposure test. Furthermore, no detectable change was observed in the PL spectra of perovskite films before and after the air exposure (**Figure 2–24a**). The red and blue curves in **Figure 2–24b** show XRD patterns measured from fresh and 600 h–air exposed samples, respectively. Both samples had similar XRD patterns.

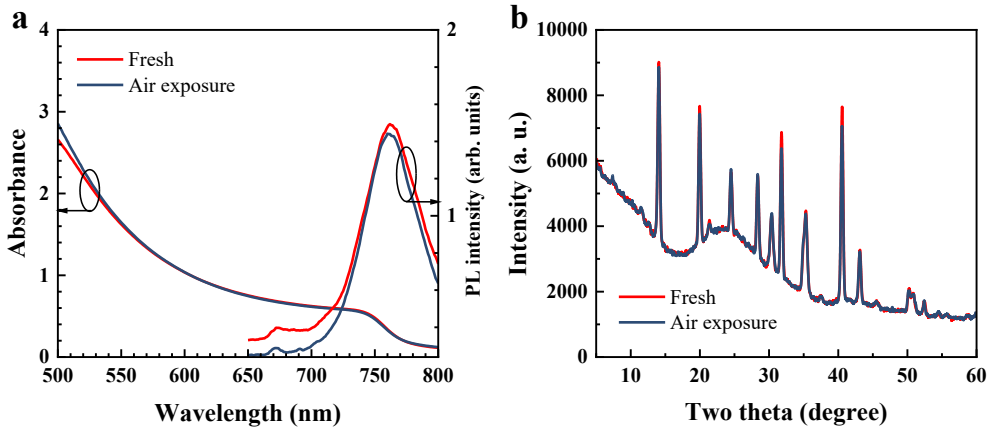

Figure 2–24. (a) UV–VIS absorption and stead–state PL spectra and (b) XRD patterns of fresh and air–exposed perovskite films. The XRD peaks at 14, 20, 28.4, and 32° can be assigned to the cubic perovskite structure.[47]

Furthermore, **Figures 2–25a** and **b** present SEM images of perovskite films before and after air exposure. There was no large difference in the surface morphologies of perovskite films before and after air exposure. These results indicate that the oxygen–induced degradation in device performance is not directly related to the degradation of the perovskite films. Therefore, it can be concluded that one of the possible reasons for the decreased PSC performance in air is the hole transport level deepening in the spiro–OMeTAD HTL and not the perovskite light absorber degradation.

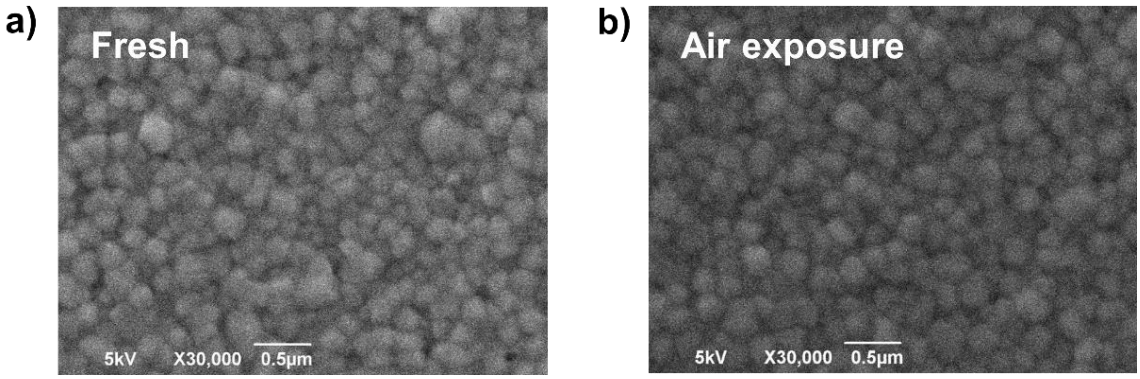

Figure 2–25. Top–view SEM images of (a) fresh and (b) air–exposed perovskite films.

It has been reported that the increased σ of spiro–OMeTAD in air is motivated by the oxygen doping, which results in the performance enhancement in PSCs[25]. It is common to obtain higher PSC performance by exposing the spiro–OMeTAD HTL to ambient air for several hours for the oxygen doping.[29,30] On the other hand, a reduction in device performance is also observed after longer air exposure.[27] In PSCs fabricated in this work, a performance improvement at the beginning of the air exposure was not observed. It supposes that, even without the oxygen doping,

the chemical doping of our spiro–OMeTAD HTL with LiTFSI and FK209 is sufficient in terms of the σ and hole transport level. Although short air exposure may be advantageous to device performance in some PSCs, conclusion of this study is that long air exposure for hundreds of hours causes PSC performance to decrease. This is because of the formation of the too deep hole transport level of spiro–OMeTAD, which is caused by oxygen doping. Note that the water and iodine also affect the hole transport level. Additionally, no degradation of perovskite films was not observed as the results of the optical, structural, and morphological measurements. However, even longer air exposure for >1,000 h might degrade the perovskite films.

2.3 Conclusion

In this study, the reason for the degradation of PSCs in air were investigated. It was found that oxygen doping into the spiro–OMeTAD HTL was one of the mechanisms of the air–induced PSC degradation. This oxygen doping deepens the hole transport level of spiro–OMeTAD, which increases the energy barrier for hole extraction over time and gradually makes PCEs lower. Although PCEs of air–exposed PSCs were reduced by ~20% of the initial value after 600 h of the air exposure, storing these air–exposed devices in a vacuum overnight recovered half of the efficiency loss because of the oxygen removal from the devices. Therefore, I believe that the oxygen–induced degradation is reversible to some extent. No detectable degradation of the perovskite light absorber was not observed after 600 h of air exposure. To improve long–term device durability, exposure of devices to air should be minimized. Developing a reliable encapsulation technology or a more durable HTL material is an important step toward the realization of air–stable PSCs in the future.

2.4 Experimental Section/Methods

2.4.1 Materials

A SnO_2 colloidal precursor solution [15% tin(IV) oxide in water] was purchased from Alfa Aesar. All the precursor materials, such as cesium iodide (CsI), formamidinium iodide (FAI), methylammonium bromide (MABr), lead iodide (PbI_2), and lead bromide ($PbBr_2$) for the perovskite layer fabrication were purchased from Tokyo Chemical Industry. Spiro–OMeTAD was purchased from Merck. Chlorobenzene (CB), dimethylformamide (DMF), dimethyl sulfoxide (DMSO), acetonitrile, and dopant materials, such as bis(trifluoromethane)–sulfonimide lithium salt (LiTFSI), 4–tert–butylpyridine (4–tBP) and tris(2–(1Hpyrazol–1–yl)–4–*tert*–butylpyridine)cobalt(III)tris–(bis(trifluoromethane)sulfonimide) (FK–209), for the spiro–OMeTAD HTL fabrication were purchased from Sigma–Aldrich. These purchased materials were used without further purification.

2.4.2 Device Fabrication

Glass substrates coated with a 100–nm–thick ITO layer (Atsugi Micro; a sheet resistance of ~10 Ω sq^{-1}) were cleaned sequentially in detergent, pure water, acetone, and isopropanol with ultrasonication each for 10 min. Then, the ITO–coated substrates were subjected to UV–ozone treatment for 15 min. After the substrate cleaning, a SnO_2 ETL was deposited on the ITO layer by spin–coating at 3,000 rpm for 30 s from an aqueous SnO_2 colloidal solution, which was diluted in water at a ratio of SnO_2 : water = 1 : 3 in volume. Then, the SnO_2 layer was annealed at 150 °C for 30 min and treated with UV–ozone for 15 min. The perovskite precursor solution was prepared by mixing FAI (1.10 M), PbI_2 (1.12 M), MABr (0.2 M), and $PbBr_2$ (0.2 M) in a solvent mixture (DMF : DMSO = 4 : 1 in volume). CsI (0.08 M) was added to the aforementioned precursor solution from a stock solution of CsI (1.5 M) in DMSO. The precursor solution was stirred at 70 °C for 3 h and then filtered through a PTFE membrane with a 0.2 μm pore size before use. A perovskite layer was spin–coated from the precursor solution on the substrate coated with ITO and SnO_2. The first spin–coating was performed at 1,000 rpm for 10 s, followed by 6,000 rpm for 30 s. During the second phase, 150 μL of chlorobenzene was dropped on the substrate, 10 s before the substrate rotation was stopped. The film was then annealed at 100 °C for 30 min. A spiro–OMeTAD HTL was spin–coated from a solution, which was prepared by mixing 1 ml of a spiro–OMeTAD solution (73 mg ml^{-1} in CB), 30 μl of a 4–tBP solution, 18 μl of a LiTFSI solution (520 mg ml^{-1} in

acetonitrile), and 29 µl of an FK–209 solution (300 mg ml^{-1} in acetonitrile), at 4,000 rpm for 30 s. Finally, a 70–nm–thick gold electrode was thermally deposited in a vacuum to complete the devices. The vacuum pressure was on the order of 10^{-4} Pa and the gold evaporation rate was ~0.1 nm s^{-1}. All the film fabrication was carried out in nitrogen, except the spin–coating and annealing of SnO_2 in the air with a relative humidity of ~20%. For the PSCs, a moth eye–type antireflective film (MOSMITE™, Mitsubishi Chemical) was attached on the glass surface.

2.4.3 Characterizations and Measurements

J–V measurements were carried out on PSCs using a computer–controlled Keithley 2400 source unit under the AM1.5G simulated solar illumination from a Xe lamp–based solar simulator (SRO–25 GD, Bunkokeiki). The *J–V* scans were performed at a rate of 0.2 V s^{-1}. PCSs were masked for each *J–V* scan to ensure the same active area for all measured devices. The active area was defined to be 3.24 mm^2 (1.8 × 1.8 mm^2) while the original device area defined by an overlap of the ITO and Au electrodes was 4 mm^2 (2 × 2 mm^2). Before each measurement, the lamp power was carefully calibrated at 100 mW cm^{-2} (1 sun) using a crystalline Si reference cell with an amorphous Si optical filter (Bunkokeiki), which was certificated by the National Institute of Advanced Industrial Science and Technology of Japan. IPCE curves of PSCs were measured with the same system used for the *J–V* measurements. For TPV and TPC measurements, a nitrogen laser (NL100, SRS) and oscilloscope (DS–510B, IWATSU) were used.

For σ measurements of hole–only devices, a doped spiro–OMeTAD layer was deposited on an ITO–coated glass substrate using the same conditions mentioned earlier. A 10 nm–thick MoO_3 interlayer and a 70 nm–thick gold electrode were thermally deposited onto the doped spiro–OMeTAD layer in the vacuum. The thermal evaporation rate was ~0.05 nm s^{-1} for MoO_3 and ~0.1 nm s^{-1} for gold. *J–V* curves of hole–only devices were measured under the dark with the same system used for the solar cell measurements.

For the hole transport energy level measurements, a doped spiro–OMeTAD layer was fabricated on an ITO–coated glass substrate using the same conditions mentioned earlier. Photoelectron yield spectroscopy (AC–3, Rikenkeiki), which enables energy–level measurements in air, was carried out on the spiro–OMeTAD samples. The FT–IR spectra of the undoped and doped spiro–OMeTAD films, which were fabricated on an Au–deposited glass substrate, were measured with an FT–IR spectrometer (FT/IR–4200, JASCO) before and after ~600 h of the air exposure. Additionally, UV–VIS absorption spectra of the undoped and doped spiro–OMeTAD

films, which were spin–coated on a quartz substrate, were measured with an absorption spectrometer (V–730, JASCO).

For optical, structural, and morphological characterization of the perovskite films, the SnO_2 / perovskite / doped spiro–OMeTAD / Au samples were prepared on a fused silica substrate using the same conditions mentioned earlier. Then, these samples were exposed to air for ~600 h. For comparison, fresh samples with the same layer sequence were used, without the air exposure. The top Au layer was peeled off with scotch tape from the fresh and ~600 h–air–exposed samples. Then, washing with chlorobenzene was used to remove the spiro–OMeTAD layer from the perovskite surface. Steady–state PL spectra of the perovskite layers were obtained using a JASCO FP–8300 spectrofluorometer, with a measurement wavelength range from 650 nm to 800 nm, a measurement step of 0.2 nm, and an excitation wavelength of 460 nm. UV–VIS absorption spectra and SEM images of the perovskite layers were measured with an absorption spectrometer (V–730, JASCO) and SEM machine (JCM–5700, JEOL), respectively. The structural properties of the perovskite layers were analyzed with an XRD system using a typical 2 θ/θ technique [λ = 1.54 Å (CuKα)] (SmartLab, Rigaku). For the QCM measurements, a QCM TRIAL KIT (PIEZO PARTS) was used.

References

[1] J. Hagen, W. Schaffrath, P. Otschik, R. Fink, A. Bacher, H. W. Schmidt, D. Haarer, *Synth. Met.* **1997**, *89*, 215.

[2] H.-S. Kim, C.-R. Lee, J.-H. Im, K.-B. Lee, T. Moehl, A. Marchioro, S.-J. Moon, R. Humphry-Baker, J.-H. Yum, J. E. Moser, M. Grätzel, N.-G. Park, *Sci. Rep.* **2012**, *2*, 591.

[3] J. Burschka, A. Dualeh, F. Kessler, E. Baranoff, N. L. Cevey-Ha, C. Yi, M. K. Nazeeruddin, M. Grätzel, *J. Am. Chem. Soc.* **2011**, *133*, 18042.

[4] B. Tan, S. R. Raga, A. S. R. Chesman, S. O. Fürer, F. Zheng, D. P. McMeekin, L. Jiang, W. Mao, X. Lin, X. Wen, J. Lu, Y. B. Cheng, U. Bach, *Adv. Energy Mater.* **2019**, *9*, 1901519.

[5] Z. Hawash, L. K. Ono, S. R. Raga, M. V. Lee, Y. Qi, *Chem. Mater.* **2015**, *27*, 562.

[6] T. A. Berhe, W. N. Su, C. H. Chen, C. J. Pan, J. H. Cheng, H. M. Chen, M. C. Tsai, L. Y. Chen, A. A. Dubale, B. J. Hwang, *Energy Environ. Sci.* **2016**, *9*, 323.

[7] K. Domanski, E. A. Alharbi, A. Hagfeldt, M. Grätzel, W. Tress, *Nat. Energy* **2018**, *3*, 61.

[8] N. Aristidou, C. Eames, I. Sanchez-Molina, X. Bu, J. Kosco, M. Saiful Islam, S. A. Haque, *Nat. Commun.* **2017**, *8*, 15218.

[9] N. Aristidou, I. Sanchez-Molina, T. Chotchuangchutchaval, M. Brown, L. Martinez, T. Rath, S. A. Haque, *Angew. Chemie - Int. Ed.* **2015**, *54*, 8208.

[10] F. T. F. O'Mahony, Y. H. Lee, C. Jellett, S. Dmitrov, D. T. J. Bryant, J. R. Durrant, B. C. O'Regan, M. Graetzel, M. K. Nazeeruddin, S. A. Haque, *J. Mater. Chem. A* **2015**, *3*, 7219.

[11] R. Schölin, M. H. Karlsson, S. K. Eriksson, H. Siegbahn, E. M. J. Johansson, H. Rensmo, *J. Phys. Chem. C* **2012**, *116*, 26300.

[12] Y. Wang, J. Wu, X. Wang, S. Wang, Z. Yan, C. Wang, F. Cao, Z. Wu, C. Ke, Z. Lan, W. Sun, *Electrochim. Acta* **2022**, *429*, 141038.

[13] X. Wang, J. Wu, Y. Yang, X. Liu, Q. Guo, Z. Song, G. Li, Z. Lan, M. Huang, *J. Mater. Chem. A* **2019**, *7*, 13256.

[14] S. Moghadamzadeh, I. M. Hossain, M. Jakoby, B. A. Nejand, D. Rueda-delgado, J. A. Schwenzer, S. Gharibzadeh, T. Abzieher, R. Khan, A. A. Haghighirad, I. A. Howard, B. S. Richards, U. W. Paetzold, *J. Mater. Chem. A* **2020**, *8*, 670.

[15] Y. Zhang, Y. Zhu, M. Hu, N. Pai, T. Qin, Y. Cheng, U. Bach, A. N. Simonov, J. Lu, *J. Phys. Chem. Lett.* **2022**, *13*, 2792.

[16] G. Tumen-Ulzii, M. Auffray, D. Klotz, G. F. Harrington, X. K. Chen, U. Balijapalli, V. Vediyappan, N. Nakamura, Z. Feng, K. Takekuma, Y. Fujita, P. Wang, S. Yamada, K. Tamada, M. Batmunkh, Y. L. Zhong, F. Mathevet, H. Salway, M. Anaya, S. D. Stranks, T. Matsushima, C. Adachi, *ACS Appl. Energy Mater.* **2022**, *5*, 15819.

[17] E. R. Nandayapa, K. Hirselandt, C. Boeffel, E. L. Unger, E. J. W. List-Kratochvil, *Adv. Opt. Mater.* **2021**, *9*, 2001317.

[18] P. Caprioglio, M. Stolterfoht, C. M. Wolff, T. Unold, B. Rech, S. Albrecht, D. Neher, *Adv. Energy Mater.* **2019**, *9*, 1901631.

[19] C. Ding, R. Huang, C. Ahläng, J. Lin, L. Zhang, D. Zhang, Q. Luo, F. Li, R. Österbacka, C. Q. Ma, *J. Mater. Chem. A* **2021**, *9*, 7575.

[20] L. K. Ono, P. Schulz, J. J. Endres, G. O. Nikiforov, Y. Kato, A. Kahn, Y. Qi, *J. Phys. Chem. Lett.* **2014**, *5*, 1374.

[21] U. B. Cappel, T. Daeneke, U. Bach, *Nano Lett.* **2012**, *12*, 4925.

[22] G. Du, L. Yang, J. Zhang, *Laser Photonics Rev.* **2023**, *17*, 2200475.

[23] C. Eames, J. M. Frost, P. R. F. Barnes, B. C. O'Regan, A. Walsh, M. S. Islam, *Nat. Commun.* **2015**, *6*, 7497.

[24] J. Haruyama, K. Sodeyama, L. Han, Y. Tateyama, *J. Am. Chem. Soc.* **2015**, *137*, 10048.

[25] Z. Hawash, L. K. Ono, Y. Qi, *Adv. Mater. Interfaces* **2016**, *3*, 1600117.

[26] H. Kanno, N. C. Giebink, Y. Sun, S. R. Forrest, *Appl. Phys. Lett.* **2006**, *89*, 2004.

[27] S. Wang, W. Yuan, Y. S. Meng, *ACS Appl. Mater. Interfaces* **2015**, *7*, 24791.

[28] R. Schölin, M. H. Karlsson, S. K. Eriksson, H. Siegbahn, E. M. J. Johansson, H. Rensmo, *J. Phys. Chem. C* **2012**, *116*, 26300.

[29] Y. Cho, H. Do Kim, J. Zheng, J. Bing, Y. Li, M. Zhang, M. A. Green, A. Wakamiya, S. Huang, H. Ohkita, A. W. Y. Ho-Baillie, *ACS Energy Lett.* **2021**, *6*, 925.

[30] N. Aida, N. Ouedraogo, G. O. Odunmbaku, B. Guo, S. Chen, X. Lin, T. Shumilova, K. Sun, *Cite This ACS Appl. Mater. Interfaces* **2022**, *14*, 34303.

[31] J. H. Noh, N. J. Jeon, Y. C. Choi, M. K. Nazeeruddin, M. Grätzel, S. Il Seok, *J. Mater. Chem. A* **2013**, *1*, 11842.

[32] Y. Yang, J. Wu, X. Liu, Q. Guo, X. Wang, L. Liu, Y. Ding, S. Dai, J. Y. Lin, *ACS Appl. Energy Mater.* **2019**, *2*, 2188.

[33] N. J. Jeon, H. Na, E. H. Jung, T.-Y. Yang, Y. G. Lee, G. Kim, H.-W. Shin, S. Il Seok, J. Lee, J. Seo, *Nat. Energy* **2018**, *3*, 682.

[34] C. M. Wolff, P. Caprioglio, M. Stolterfoht, D. Neher, *Adv. Mater.* **2019**, *31*, 1902762.

[35] K. Domanski, J.-P. Correa-Baena, N. Mine, M. K. Nazeeruddin, A. Abate, M. Saliba, W. Tress, A. Hagfeldt, M. Grätzel, *ACS Nano* **2016**, *10*, 6306.

[36] Z. Li, C. Xiao, Y. Yang, S. P. Harvey, D. H. Kim, J. A. Christians, M. Yang, P. Schulz, S. U. Nanayakkara, C. S. Jiang, J. M. Luther, J. J. Berry, M. C. Beard, M. M. Al-Jassim, K. Zhu, *Energy Environ. Sci.* **2017**, *10*, 1234.

[37] I. Lee, J. H. Yun, H. J. Son, T. S. Kim, *ACS Appl. Mater. Interfaces* **2017**, *9*, 7029.

[38] Y. Wang, T. Wu, J. Barbaud, W. Kong, D. Cui, H. Chen, X. Yang, L. Han, *Science (80-.).* **2019**, *365*, 687.

[39] B. Tan, S. R. Raga, K. J. Rietwyk, J. Lu, S. O. Fürer, J. C. Griffith, Y. Cheng, U. Bach, *Nano Energy* **2021**, *82*, 105658.

[40] S. Wang, Z. Huang, X. Wang, Y. Li, M. Günther, S. Valenzuela, P. Parikh, A. Cabreros, W. Xiong, Y. S. Meng, *J. Am. Chem. Soc.* **2018**, *140*, 16720.

[41] U. Bach, Y. Tachibana, J. E. Moser, S. A. Haque, J. R. Durrant, M. Grätzel, D. R. Klug, *J. Am. Chem. Soc.* **1999**, *121*, 7445.

[42] A. Abate, T. Leijtens, S. Pathak, J. Teuscher, R. Avolio, M. E. Errico, J. Kirkpatrik, J. M. Ball, P. Docampo, I. McPherson, H. J. Snaith, *Phys. Chem. Chem. Phys.* **2013**, *15*, 2572.

[43] G. Liu, X. Xi, R. Chen, L. Chen, G. Chen, *J. Renew. Sustain. Energy* **2018**, *10*, 043702.

[44] Q. Sun, P. Fassl, D. Becker-Koch, A. Bausch, B. Rivkin, S. Bai, P. E. Hopkinson, H. J. Snaith, Y. Vaynzof, *Adv. Energy Mater.* **2017**, *7*, 1700977.

[45] S. Pont, D. Bryant, C. T. Lin, N. Aristidou, S. Wheeler, X. Ma, R. Godin, S. A. Haque, J. R. Durrant, *J. Mater. Chem. A* **2017**, *5*, 9553.

[46] M. M. Lee, J. Teuscher, T. Miyasaka, T. N. Murakami, H. J. Snaith, *Science (80-.).* **2012**, *338*, 643.

[47] M. Saliba, T. Matsui, J. Y. Seo, K. Domanski, J. P. Correa-Baena, M. K. Nazeeruddin, S. M. Zakeeruddin, W. Tress, A. Abate, A. Hagfeldt, M. Grätzel, *Energy Environ. Sci.* **2016**, *9*, 1989.

CHAPTER 3

Suppressed Gold Penetration with Molybdenum Oxide Interlayer to Increase Power Conversion Efficiency of Perovskite Solar Cells

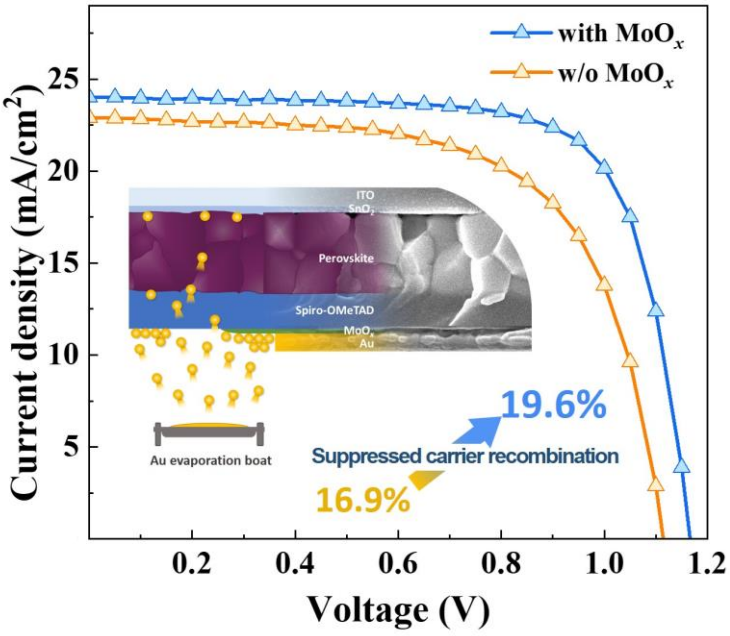

Chapter 3: Suppressed Gold Penetration with Molybdenum Oxide Interlayer to Increase Power Conversion Efficiency of Perovskite Solar Cells

3.1 Introduction

Among various reported interface materials, molybdenum oxide (MoO_x) is a promising interlayer or HTL because of its efficient hole extraction and effective hole transport *via* oxygen vacancies-related energy channels[1] as well as it can also be paired with conventional electrode metals in perovskite solar cells.[2–4] The MoO_x interlayer is typically achieved through vacuum deposition. The source material used for the deposition has $x = 3$. However, vacuum-deposited MoO_x films tend to exhibit an x value smaller than 3 due to the presence of numerous oxygen vacancy defects[5]. Recent efforts have focused on inserting MoO_x as an interlayer between the HTL and the metal electrode to improve the performance of PSCs.[6–10] However, it is still unclear why PSC performances are improved with MoO_x.

On the other hand, Au is widely used as the top electrode for hole extraction in PSCs because of its very high chemical stability and high work function. However, I observed that Au penetrates into the perovskite light absorber when Au is vacuum-deposited on top of the chemically doped HTL of spiro-OMeTAD. Therefore, in this chapter, the effect of Au penetration on the performance of PSCs was investigated. The penetrated Au component induced the carrier recombination in the perovskite layer, decreasing the PCEs of PSCs. Although the Au migration into the perovskite layer during long-term operation is reportedly one source of the PSC degradation[11,12], the penetration of Au through the spiro-OMeTAD HTL into the perovskite layer in fresh samples has never been reported to date. To mitigate this Au penetration, a MoO_x interlayer was inserted between the spiro-OMeTAD HTL and the Au electrode, increasing PCEs. In addition to the suppressed Au penetration, energy level matching at the HTL/MoO_x/Au interfaces is likely another reason for the increased PCEs. This is an encouraging finding that provides an effective way to suppress the failure of PSCs by clarifying the reason for efficiency limitation.

3.2 Results and Discussion

The PSCs' architecture investigated in this study was glass substrate / ITO (~100 nm) / SnO_2 (~30 nm) / perovskite (~650 nm) / chemically doped spiro–OMeTAD (~170 nm) / MoO_x / Au (~70 nm). The perovskite absorber layer was based on the mixed–cation mixed–halide composition $Cs_{0.05}(FA_{0.85}MA_{0.15})_{0.95}Pb(I_{0.85}Br_{0.15})_3$ as same as Chapter 2. Discrepantly, the perovskite layer is treated with pyridine–carbazole (PyCz) to passivate the surface defects.[13] **Figure 3–1a** represents the architecture of PSCs, wherein the thickness of the MoO_x layer inserted between the spiro–OMeTAD HTL and the Au electrode varied from 5 to 30 nm. PSCs without the MoO_x interlayer were also fabricated as a reference. SnO_2, perovskite, and spiro–OMeTAD layers were spin–coated (see the details in Experimental section). The MoO_x interlayer was thermally deposited at a slow evaporation rate of ~0.05 nm s^{-1}, allowing precise control of the thin film thickness from 5 nm to 30 nm. Oxygen vacancies were formed in resulting films (MoO_x) during the vacuum deposition although molybdenum trioxide (MoO_3) was a source material. Finally, a 70–nm–thick Au electrode was thermally deposited to complete the devices at the evaporation rate of ~0.1 nm s^{-1}. A cross–sectional SEM image of PSCs with the optimized MoO_x thickness of 15 nm is shown in **Figure 3–1b**, showing that the individual layers were properly stacked to form PSCs.

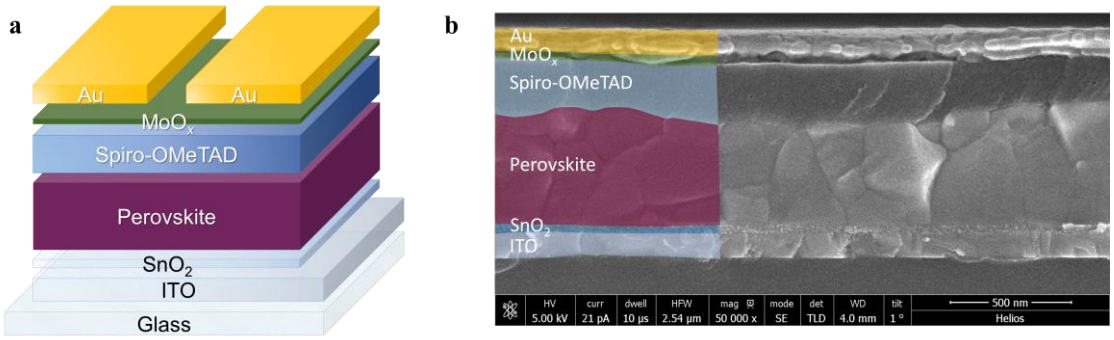

Figure 3–1. (a) Schematic of the PSC architecture used in this study. (b) Cross–sectional SEM image of the completed device with the 15–nm–thick MoO_x interlayer.

Figure 3–2a shows the *J*−*V* curves of PSCs with the different thicknesses of the MoO_x interlayers. As shown in **Figure 3–2b**, J_{SC}, V_{OC}, and FF of PSCs increased as the MoO_x thickness increased from 0 to 15 nm. Overall, all the parameter enhancements led to an improvement in average PCE from 16.9% to 19.6%. However, as the thickness of the MoO_x interlayer was further increased to 20 nm and 30 nm, the device performance deteriorated. This was mainly due to a

decrease in FF, implying an increase in series resistance, which will be discussed later. Thus, the optimized MoO_x thickness was found to be 15 nm, which can provide the highest PCE.

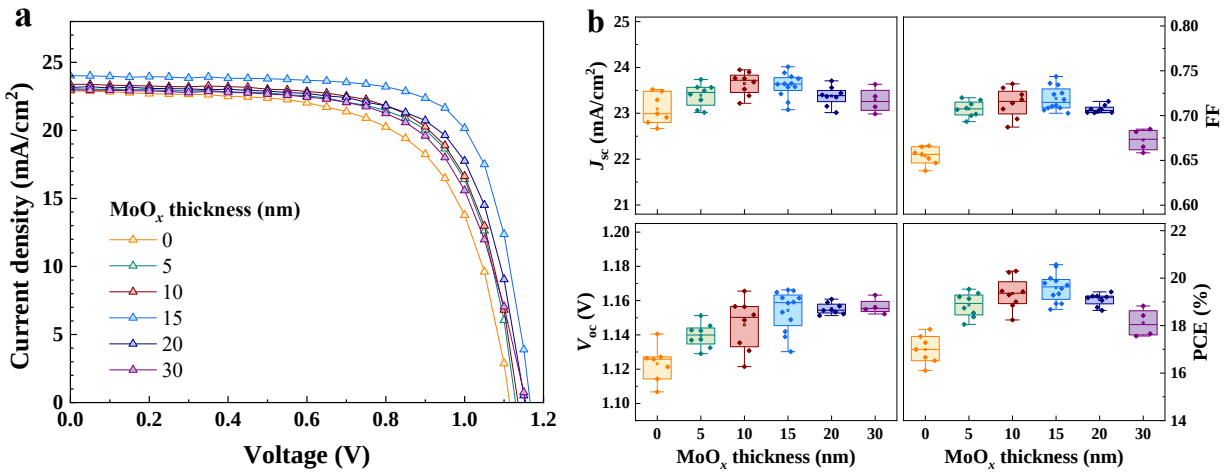

Figure 3–2. (a) Representative *J–V* curves of PSCs with different thicknesses of MoO_x, which were measured under the 1 sun condition in the reverse scan from the positive to negative voltages. (b) Box plots of the J_{SC}, V_{OC}, FF, and PCE of PSCs, which were obtained from (a), as a function of MoO_x thickness.

Figure 3–3a shows representative IPCE curves of PSCs with MoO_x of different thicknesses. The IPCE values at ~700 nm were different depending on the samples, the reason of which is still unclear and needs further investigation. Integration of the IPCE curves gave J_{SC} values (**Figure 3–3b**). Median values of J_{SC} are in agreement with those estimated from the *J–V* measurements. Additionally, the bandgap value was estimated at ~1.57 eV from the onsets of the IPCE curves (**Figure 3–3c**), which agrees with the literature.[13]

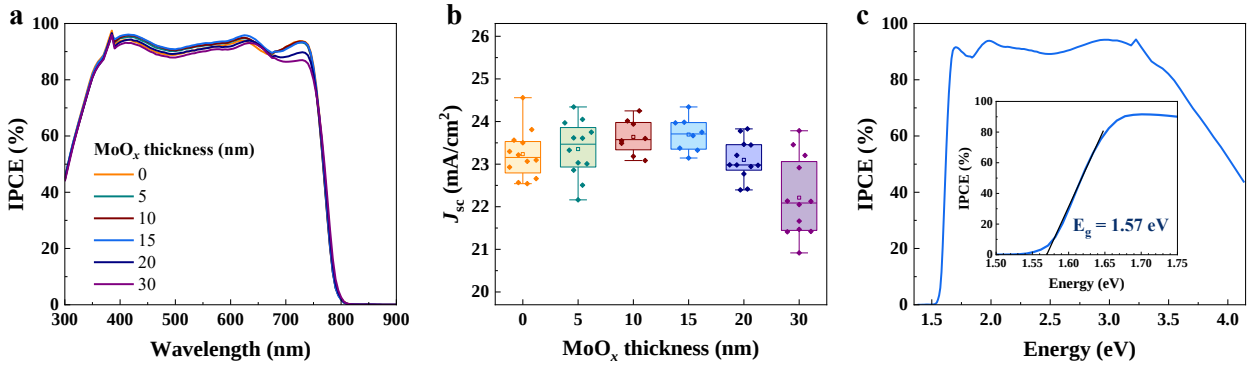

Figure 3–3. (a) Representative IPCE curves of PSCs with MoO_x of different thicknesses. (b) Box plots of the J_{SC} calculated over the IPCE integration as a function of MoO_x thickness. (c) IPCE curve of PSCs with the 15–nm–thick MoO_x interlayer, in which the *x*–axis scale is energy. The bandgap calculated from the IPCE onset was ~1.57 eV [see the inset of (c)].

PSCs with the optimized MoO_x thickness of 15 nm had PCEs of 18.02% and 19.79%, which were respectively measured in the forward and reverse bias scans. (**Figure 3–4a**). In the forward

scan, the J_{SC} was 23.05 mA cm^{-2}, the V_{OC} was 1.14 V, the FF was 0.68, and the PCE was 18.02%. In the reverse scan, the J_{SC} was 23.08 mA cm^{-2}, the V_{OC} was 1.16 V, the FF was 0.74, and the PCE was 19.79%. The reverse scan was slightly better than the forward scan in terms of the device performance; thus, the reverse scan was used for the discussion in this study. The migration of ionic species in the perovskite layers frequently causes the *J*–*V* hysteresis in PSCs.[14,15] Furthermore, the maximum power point tracking method was used to obtain **Figure 3–4b**. PCEs increased rapidly and stabilized just after the light illumination began. The stabilized PCE was ~19%, which is similar to those obtained from the *J*–*V* curves shown in **Figure 3–2a**.

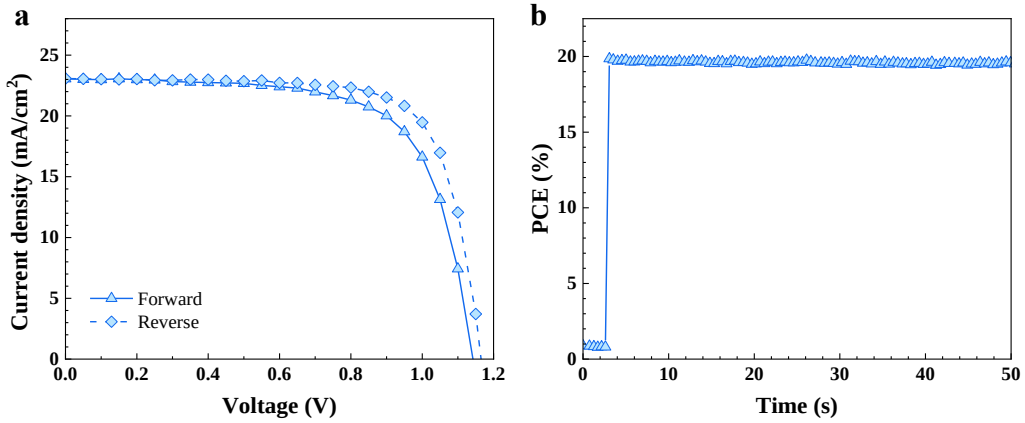

Figure 3–4. (a) *J*–*V* curves and (b) PCE evolution of PSCs with the 15–nm–thick MoO_x interlayer. The *J*–*V* curves in (a) were measured in the consecutive forward and reverse voltage scans.

Suemori *et al.* observed the deep penetration of Au atom into perylene pigment organic films, used for organic solar cells, during the vacuum deposition.[16] This issue is particularly problematic for organic solar cells, as they typically use polycrystalline materials with grain boundaries, facilitating metal electrode penetration. In PSCs, however, an amorphous organic HTL is commonly used between the active perovskite polycrystalline layer and the metal electrode. Without the HTL, the direct contact between the metal electrode and the perovskite layer in PSCs induces significantly high charge carrier recombination, in consequence; V_{OC} and J_{SC} are decreased considerably.[17] However, the low film density and pinhole formation in the solution–processed organic HTL pose issues because they serve as channels for the diffusion of gas molecules and the migration of ions and metal electrode components.[18] If Au with high incident kinetic energy during vacuum evaporation penetrates through the spiro–OMeTAD HTL and reaches the perovskite layer, it will work as a carrier recombination center, thereby reducing PCEs. To confirm if the Au penetration happens in PSCs, the elemental depth profiling was performed using time–of–flight secondary ion mass spectroscopy (ToF–SIMS). This analytical technique offers greater

sensitivity and can more easily detect organic, inorganic, and metal species of perovskite–based devices.[11,19]

Figures 3–5a and **b** show depth profiles of as–fabricated PSCs without and with the 15–nm–thick MoO_x interlayer, respectively. The Au^- ion trace is associated with the gold electrode. The CN^- ion trace corresponds to either the spiro–OMeTAD HTL or the perovskite layer (MA and FA). The I^- and MoO_3^- ion traces are attributed to the perovskite layer and MoO_x interlayer, respectively. The Au^- trace was observed inside the perovskite layer of devices without the MoO_x interlayer; Au is accumulated near the perovskite/SnO_2 interface. Spin–coating SnO_2 colloidal solution onto ITO–coated glass substrates provides uniform, dense, and pinhole–free films.[20] Therefore, the Au component penetrated through the soft spiro–OMeTAD layer and the grain boundaries of the perovskite layer and finally accumulated at the interface with the SnO_2 ETL or the ITO electrode. However, the intensity of the Au^- trace inside the perovskite layer was decreased in the PSCs with the MoO_x interlayer, which indicates that the Au penetration was suppressed to some extent by introducing the MoO_x interlayer. The considerable amount of metal migrating into the perovskite layer has been observed previously in aged PSCs at an elevated temperature condition.[11,21] Moreover, Snaith *et al.* have demonstrated the migration of Au into the perovskite layer for PSCs aged even at room temperature under light illumination, resulting in electronic shunts.[12] This study presents the first direct evidence of Au penetration into the perovskite layer in as–prepared PSCs. Moreover, a higher intensity trace of Au^- was observed in the spiro–OMeTAD HTL of the PSCs with the MoO_x interlayer. This discrepancy could be attributed to the robust nature of the MoO_x interlayer which may have hindered the uniformity of the etching during ToF–SIMS depth profiling. Consequently, the non–uniform etching of the MoO_x interlayer could lead to a higher intensity trace of Au^- detected in the spiro–OMeTAD layer. However, it is essential to note that the exact reason behind this observation is currently under investigation. Additionally, I would like to emphasize that while the presence of Au in the HTL may be notable, it may not have a significant impact on carrier recombination compared to the Au presence in the perovskite layer.

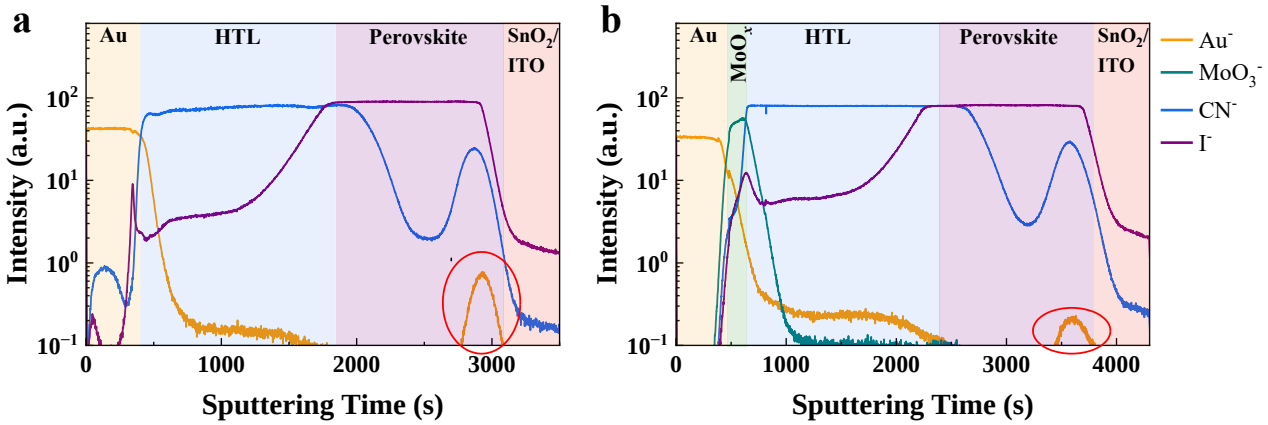

Figure 3–5. ToF–SIMS depth profiles of PSCs (a) without and (b) with the 15–nm–thick MoO_x interlayer. The red circles in (a) and (b) indicate the Au penetrated from the top electrode and accumulated near the perovskite / SnO_2 interface.

To clarify the effect of the Au penetration into the perovskite layer, steady–state PL and time–resolved transient PL measurements were performed on perovskite samples with the architecture of fused silica / perovskite and fused silica / perovskite / Au. The samples were fabricated with the conditions used for the PSC fabrication. **Figure 3–6a** shows the PL spectra of perovskite samples, where the spectral shape agrees with the literature.[22] The steady–state PL intensity was largely decreased by an order of magnitude in the perovskite film coated with an Au layer. This large decrease in PL intensity was attributed to the shortened PL lifetime as seen in **Figure 3–6b**. The PL decay curves exhibited multiexponential dynamics because of the presence of multiple carrier recombination processes.[23,24] For simplicity, the PL lifetime is defined as the time at which PL intensity decays to 1/e of the initial value. With the direct evaporation of Au on top of the perovskite layer, the PL lifetime was decreased from ~4.93 ns to ~3.26, which surely indicates the charge carrier recombination by Au.

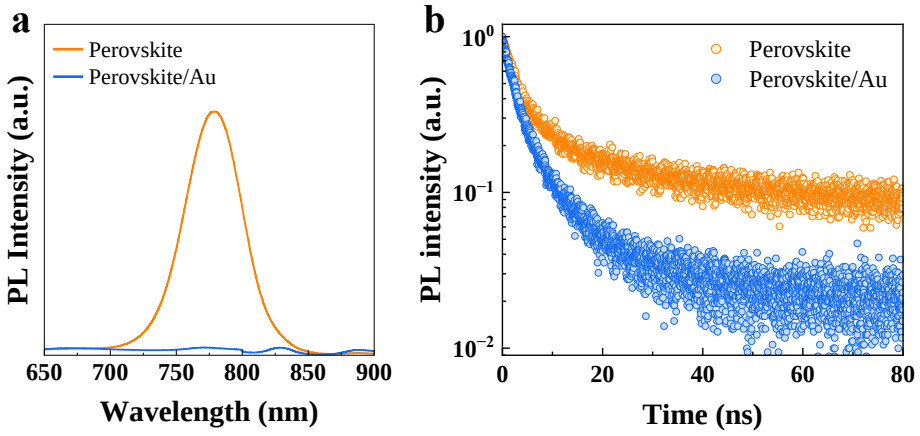

Figure 3–6. (a) Steady–state PL spectra and (b) transient PL decays of perovskite films coated without and with Au.

Furthermore, PL measurements were performed on perovskite samples mimicking the device structure to confirm if Au penetrates through the HTL and works as the carrier recombination center in the perovskite light absorber. The samples with the architecture of fused silica / perovskite / chemically doped spiro–OMeTAD / Au and fused silica / perovskite / chemically doped spiro–OMeTAD / MoO_x / Au were fabricated with the conditions used for the PSC fabrication. Then, the Au and MoO_x layers were removed with scotch tape and the spiro–OMeTAD layer was also removed by rinsing with chlorobenzene by spin–coating. **Figures 3–7a** and **b**, respectively, show steady–state PL spectra and transient PL decays of perovskite films after removing the spiro–OMeTAD, MoO_x, and Au layers. When no interlayer was used before the Au deposition, PL intensity decreased by ~3–fold, which indicates carrier recombination induced by the Au penetration in the perovskite absorber layer. The PL lifetimes were calculated from **Figure 3–7b** in the same way. An increase in PL lifetime from ~3.96 ns to ~6.09 ns was observed in the case of using the MoO_x interlayer. This prolonged PL lifetime is attributed to the suppression of the Au–induced carrier recombination. These results are in good agreement with the reduced Au^- trace in devices with MoO_x. It is noted here that the PL lifetime was longer for perovskite films after removing spiro–OMeTAD, MoO_x, and Au (~6.09 ns) than for bare perovskite films without the fabrication of any overlying layers (~4.93 ns). The one of the dopants, 4–tBP, is known to passivate surface defects of perovskite films.[25] Therefore, it is speculated that a small amount of 4–tBP is still left for the former samples, resulting in a longer PL lifetime.

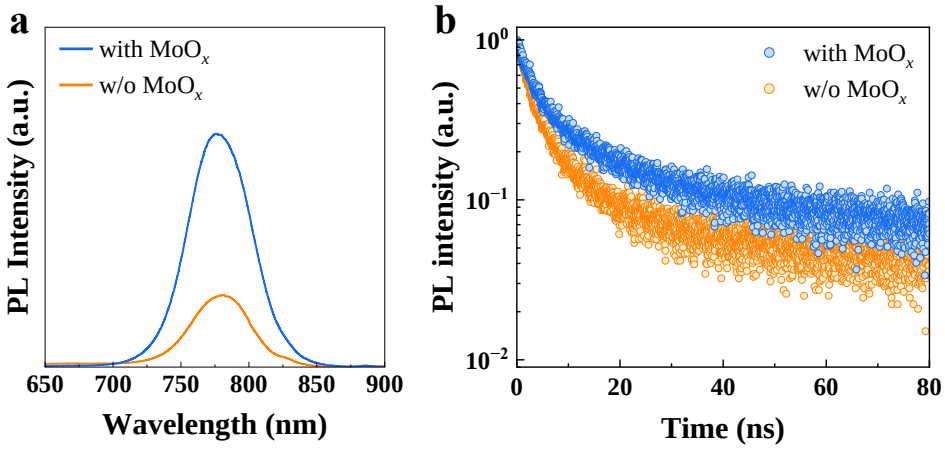

Figure 3–7. (a) Steady–state PL spectra and (b) transient PL decays of perovskite films after removing the overlying layers.

To further study the carrier recombination in the perovskite light absorber, TPV decay curves of PSCs without and with the 15–nm–thick MoO_x interlayer were measured by using a previously mentioned technique in Chapter 2. The TPV lifetimes and TPC lifetimes discussed later

are defined times, at which TPV or TPC intensity decays to 1/e of the initial value. As can be seen in **Figure 3–8a**, the TPV lifetimes were longer with MoO_x (~0.37 ms) than without MoO_x (~0.21 ms), which again indicates the carrier recombination caused by the Au penetration being suppressed with MoO_x. Based on the above results, I believe that the MoO_x interlayer mitigates the Au penetration into the perovskite layer, thereby minimizing the carrier recombination. The soft properties of organic materials allow metal penetration even through non–porous and amorphous films, especially solution–processed organic films, which are not capable enough of blocking Au from going through. Therefore, the initial device performance could be improved by increasing the thickness of the MoO_x interlayer, reaching its maximum at 15 nm.

In several reports, it has been evidenced that the MoO_x interlayer contributes to the effective hole extraction due to the upward movement of the vacuum level (VL) caused by a charge transfer at the interface.[26,27] Electrons are transferred between the very low–lying conduction band of the *n*–type MoO_x and the HOMO of organic HTL molecules. Therefore, the interfacial electronic structures and the energy level matching at the spiro–OMeTAD / MoO_x / Au interface would also affect the improvements in the performance of PSCs. Schulz *et al*. demonstrated a VL shift at the interface of perovskite / spiro–OMeTAD / MoO_x in PSC architectures on the basis of ultraviolet photoelectron spectroscopy.[8] The HOMO onset of spiro–OMeTAD, initially ~1.0 eV below its E_F, was subsequently shifted to 0.6 eV below E_F, indicating that the spiro–OMeTAD layer is *p*–doped by a charge transfer to MoO_x.[8]

Therefore, the carrier extraction can be improved with the MoO_x interlayer, as a result of the charge transfer from Au to MoO_x and from spiro–OMeTAD to MoO_x. To confirm improved charge extraction, TPC measurements were simply carried out on PSCs. **Figure 3–8b** shows the increased TPC lifetime in PSCs with the MoO_x interlayer, demonstrating improved carrier extraction.[28–30] Accordingly, the improved initial device performance could be attributed to the combined positive effects offered by the MoO_x interlayer, including the suppressed Au penetration into the perovskite active layer and the enhanced hole extraction.

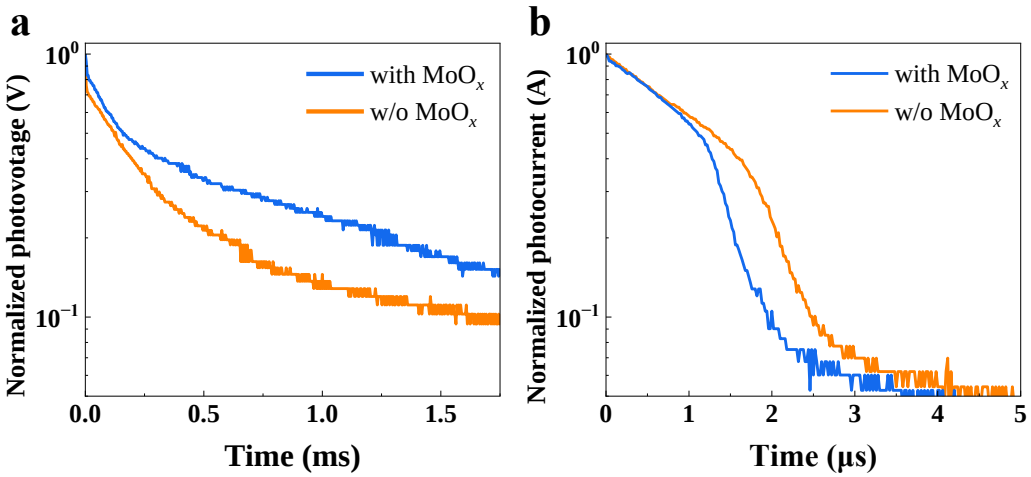

Figure 3–8. (a) TPV and (b) TPC decay curves of PSCs with and without the 15–nm–thick MoO_x interlayer.

To gain deeper insight into the change in charge carrier transport with MoO_x, *J*–*V* curves of spiro–OMeTAD–based hole–only devices (HODs) with different thicknesses of MoO_x were compared in **Figure 3–9a**. Here, HODs had the following configuration: glass substrate / ITO (~100 nm) / chemically doped spiro–OMeTAD (~170 nm) / MoO_x / Au (~70 nm) as depicted in the inset of **Figure 3–9a**. **Figure 3–9b** shows a plot of current densities as a function of MoO_x thickness. The current densities were roughly constant in a MoO_x layer thickness range between 5 nm and 15 nm. However, this behavior changed as the MoO_x layer thickness further increased in HODs. The decreased current density above the 15 nm thickness of the interlayer implies an increased electrical resistance of the thick MoO_x interlayer, which is consistent with a reduction in FF (**Figures 3–2a** and **b**). Furthermore, a similar change was observed in series resistance estimated from the *J*–*V* curves of PSCs (**Figure 3–9c**). I believe that the introduction of the above 15–nm–thick MoO_x decreases device performance, mainly due to the increased resistance.

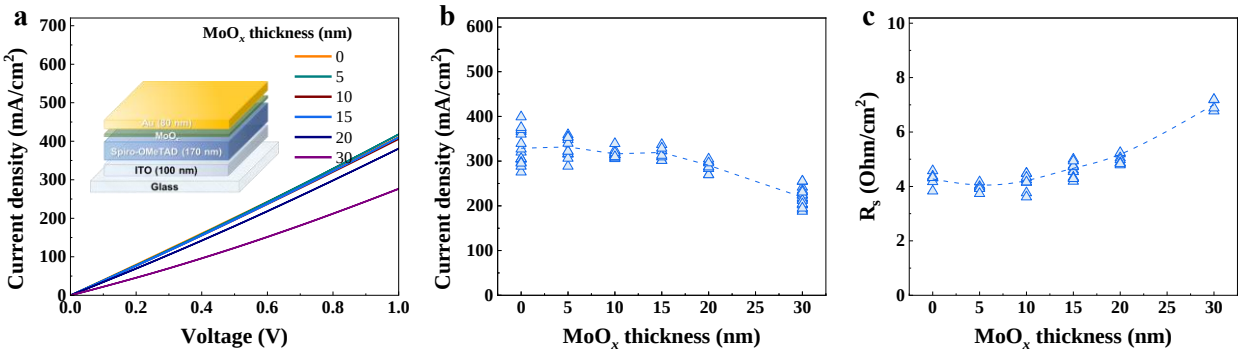

Figure 3–9. (a) Representative *J*–*V* curves of chemically doped spiro–OMeTAD–based HODs without and with MoO_x interlayers of different thicknesses. These *J*–*V* curves were measured under the dark condition. (b) Plots of current densities of HODs at 0.8 V and (c) series resistance of PSCs as a function of MoO_x thickness. The dashed lines in (b and c) correspond to the mean values.

The long–term stability characterization was conducted under continuous light illumination at room temperature (RT) for 1,000 h. **Figures 3–10a** and **b** show the PCE, J_{SC}, $V_{OC,}$ and FF evolution of PSCs, which were fabricated in the same batch with different thicknesses of MoO_x. PCE of control PSCs without MoO_x decreased to ~70 % of their initial values after 1000 h of continuous light illumination. Even though there is a variation in stability improvement, all PSCs with the 5–30–nm–thick interlayers retained ~90 % of the initial PCE. Long–term stability variations were observed in PSCs, even when employing the same device architectures (**Figure A1**, Appendix **A–2**).

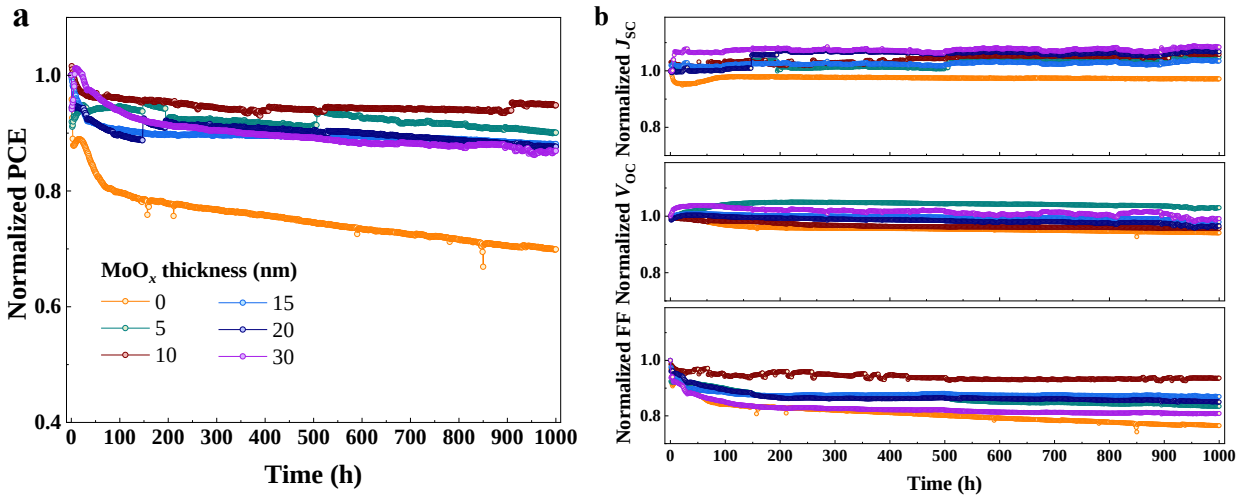

Figure 3–10. Time evolution of normalized (a) PCE and (b) J_{SC}, $V_{OC,}$ and FF of PSCs with different thicknesses of the MoO_x interlayers.

MoO_x interlayers have been used to improve the stability of different types of solar cells in ambient atmospheres with the presence of humidity and oxygen effects.[9,31] However, the stability test was performed on fully encapsulated devices to eliminate the stress from H_2O and O_2. See Appendix **A–3** for the detailed encapsulation conditions. Successful encapsulation of organic light–emitting diode (OLED), which was also used for PSCs fabricated in this study, did not result in any changes in $J-V$ and luminance−current density ($L-J$) curves of OLEDs even after ~3000 h of storage at a relative humidity of 85% and a temperature of 85 ºC (**Figure A2**, Appendix **A–3**). Although the operating condition of photovoltaics often reaches a temperature ranging from 65 ºC to 85 ºC, it is known that the degradation of perovskite materials is serious at high temperatures due to the volatilization and loss of various organic and iodine species.[32,33] However, OLEDs with encapsulation showed excellent durability even in such harsh environmental conditions. Therefore, that reliable encapsulation technology made it able to study only the intrinsic stability of PSCs, regardless of extrinsic factors such as water and oxygen. Moreover, Changzeng *et al.* reported that

the corrosion of Ag metal electrodes intrinsically induced by reactive species from the perovskite active layer was suppressed by the MoO_x interlayer.[34] In this study, the Au electrode was used, which is considered to be the most stable, probably ruling out the electrode corrosion.

ToF–SIMS depth profile measurements were performed before and after the long–term PSC stability characterization without MoO_x to try to clarify the degradation mechanisms. However, no observable changes were detected in the depth profiles, as shown in **Figure 3–11**. Au penetration was observed in the perovskite layer of PSCs without the interlayer just after the fabrication (**Figure 3–5a**). However, the intensity of Au^- remained nearly unchanged after the long–term durability measurements. Previous studies have reported the migration of Au into the perovskite layer of PSCs aged under light illumination.[12] Nevertheless, the consistent intensity of Au^- indicates that Au migration did not occur during the stability measurement. Moreover, mobile iodine ions easily migrate in the device and limit the stability of PSCs.[35] Even though the trace of I^- was detected near the interface between the HTL and the Au electrode in as–fabricated PSCs (**Figure 3–5a** and **Figure 3–11a**), there was no notable change in I^- intensity after the long–term durability measurement (**Figure 3–11b**). The reason for the degradation in PSCs, which was diminished with the MoO_x interlayer, may be an interaction between the Au electrode and the ions migrating from the perovskite layer or the deteriorated interface between the HTL and the Au electrode. Therefore, these unidentified degradation mechanisms need to be clarified in the future.

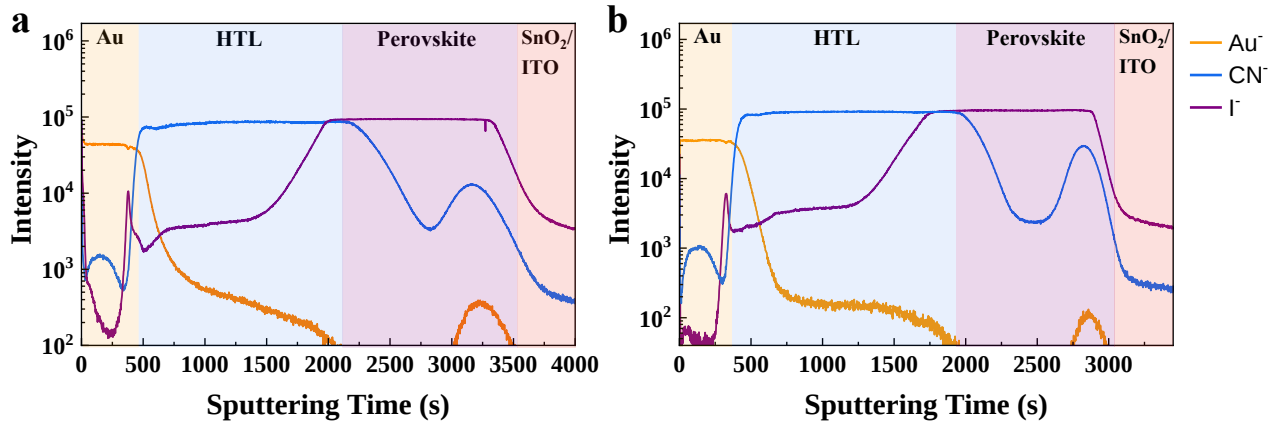

Figure 3–11. Full ToF–SIMS depth profiles of PSCs (a) before and (b) after the long–term durability characterization.

3.3 Conclusion

In conclusion, the effect of MoO_x introduced between the spiro–OMeTAD HTL and the Au electrode on the PSC performance was investigated. PSCs with the 15–nm–thick MoO_x interlayer achieved a PCE of 19.6% compared to that of 16.9% in a control device without the interlayer. This improvement was mainly attributed to the suppression of the carrier recombination induced by Au penetration into the perovskite layer as well as increased charge extraction. It was further demonstrated that the insertion of the MoO_x interlayer improved the long–term stability of PSCs. To further improve the PCEs of PSCs, the influence of metal migration into perovskite active layers must be eliminated by altering the evaporation method of the metal electrode or inserting a more robust interlayer.

3.4 Experimental Section/Methods

3.4.1 Materials

All materials (except MoO_3) used in this study were purchased from the same companies as those mentioned in Chapter 2. MoO_3 was purchased from Mitsuwa Chemical. All materials were used without further purification.

3.4.2 Device Fabrication

Glass substrates coated with a pre–patterned 100–nm–thick ITO layer (Atsugi Micro; a sheet resistance of ~10 Ω sq^{-1}) were cleaned sequentially in detergent, pure water, acetone, and isopropanol with ultrasonication each for 10 min. Then, the substrates were subjected to UV–ozone treatment for 15 min. After the substrate cleaning, a SnO_2 ETL was deposited on the ITO substrate by spin–coating at 3,000 rpm for 30 s from an aqueous SnO_2 colloidal solution, which was diluted by water with a ratio of 1:3 in volume. Then, the SnO_2 layer was annealed at 150 °C for 30 min and treated with UV–ozone for 20 min. To treat the surface of SnO_2 films[36], 1 mM of potassium hydroxide (KOH) solution in water was spin–coated on the top of the SnO_2 layer at a speed of 3,000 rpm for 30 sec and annealed at 100 °C for 10 min. The perovskite precursor solution was prepared by dissolving FAI (1.10 M), PbI_2 (1.12 M), MABr (0.2 M), and $PbBr_2$ (0.2 M) in a solvent mixture (DMF:DMSO = 4:1 in volume). CsI (0.08 M) solution in DMSO was added to the aforementioned precursor solution. The precursor solution was stirred at 70 °C for 3 h and filtered through a 0.2 μm PTFE membrane before use. A perovskite layer was spin–coated from the precursor solution on the KOH–treated SnO_2 surface at 1,000 rpm for 10 s, followed by 6,000 rpm for 30 s. During the second phase, 150 μL of chlorobenzene was dropped on the substrate at 10 s before the end of the substrate rotation, and then the perovskite layer was annealed at 100 °C for 30 min. To passivate the surface defects of perovskite films, 20 mM of pyridine– carbazole (Py–Cz) solution in CB was spin–coated on top of the perovskite layer at a speed of 3,000 rpm for 30 sec.[13] Then, a spiro–OMeTAD HTL was deposited at 4,000 rpm for 30 sec from a solution of 73 mg spiro–OMeTAD in 1 ml CB. This solution was mixed with 30 μl of a 4–tBP solution, 18 μl of a Li–TFSI solution (520 mg ml^{-1} in acetonitrile), and 29 μl of an FK–209 solution (300 mg ml^{-1} in acetonitrile). A MoO_x interlayer was thermally deposited with an evaporation rate of ~0.05 nm s^{-1} under a vacuum pressure of 10^{-4} Pa. Finally, a 70–nm–thick gold electrode was thermally deposited in a vacuum to complete the devices. The vacuum pressure was on the order of 10^{-4} Pa

and the gold evaporation rate was ~0.1 nm s^{-1}. All the film fabrication processes were carried out in a nitrogen–filled glove box, except the spin–coating, annealing, and treatment of SnO_2 in a dry glove box filled with air with a relative humidity of ~0%. The fabricated PSCs were encapsulated using a glass lid and UV–cured sealant in the nitrogen–filled glove box, without exposure to air. For HODs, a chemically doped spiro–OMeTAD layer, a MoO_x interlayer, and 70 nm–thick gold electrode were deposited sequentially on an ITO–coated glass substrate using the same conditions mentioned earlier.

3.4.3 Characterization and Measurements

J–V curve measurements were performed on the PSCs using a computer–controlled Keithley 2400 source unit under the AM1.5G simulated solar illumination from an Xe lamp–based solar simulator (SRO–25 GD, Bunko–keiki). The *J–V* scans were performed at a rate of 200 mV s^{-1}. PCSs were masked for each *J–V* scan to ensure the same active area for all measured devices. The illuminated area was defined at 3.24 mm^2 (1.8 × 1.8 mm^2) by using a shadow mask while the original device area defined by an overlap of the ITO and Au electrodes was 4 mm^2 (2 × 2 mm^2). The lamp power was carefully calibrated at 100 mW cm^{-2} (1 sun) using a crystalline Si reference cell with an amorphous Si optical filter (Bunko–keiki), which was certificated by the National Institute of Advanced Industrial Science and Technology of Japan. IPCE curves of the PSCs were measured with the same Bunko–Keiki SRO–25 GD system. For TPV and TPC measurements, a nitrogen laser (NL100, SRS) and oscilloscope (DS–510B, IWATSU) were used.

Cross–sectional SEM images of PSCs were measured by using a Helios NanoLab 600i (Thermo Fisher Scientific Inc.) system at an acceleration voltage of 5 kV with a magnification of ×50,000. For the operational stability measurements, white light from an LED with an intensity of 100 mW cm^{-2} was used to illuminate the PSCs continuously at 25 °C. V_{OC}, J_{SC}, FF, and PCE were periodically measured automatically using a lifetime measurement system (System Engineers) every 60 minutes for 1,000 h. *J–V* curves on the HODs were measured in the dark using the same system used for the solar cell measurements. The ToF–SIMS depth profiles for the Au^-, MoO_3^-, CN^-, and I^- ions were measured using a TOF–SIMS5, ION–TOF system with a Bi^+ primary beam (30 keV and 3 pA) and a Cs^+ sputter beam (1 keV and 75 nA). The sputter size was 500 × 500 μm. The analysis size was 100 μm × 100 μm for the depth profiling.

For the optical characterization, fused silica/ perovskite and fused silica/perovskite/Au samples were fabricated using the same conditions mentioned earlier. Fused silica / perovskite /

chemically doped spiro–OMeTAD / Au and fused silica / perovskite / chemically doped spiro–OMeTAD / MoO_x / Au samples were also fabricated. For the latter two samples, the top Au layer was peeled off with scotch tape. Then, CB was used to remove the spiro–OMeTAD layer from the perovskite surface by spin–coating. Steady–state PL spectra of the perovskite films were obtained using a JASCO FP–8600 spectrofluorometer, with a measurement wavelength range from 650 nm to 900 nm, a measurement step of 0.2 nm, and an excitation wavelength of 460 nm. Time–resolved PL decay was measured on the same samples using a compact fluorescence lifetime spectrometer (C16361, Hamatsu) with an excitation wavelength of 340 nm.

References

[1] J. Meyer, S. Hamwi, M. Kröger, W. Kowalsky, T. Riedl, A. Kahn, *Adv. Mater.* **2012**, *24*, 5408.

[2] Y. Zhao, A. M. Nardes, K. Zhu, *Appl. Phys. Lett.* **2014**, *104*, 213906.

[3] L. Liang, Z. Huang, L. Cai, W. Chen, B. Wang, K. Chen, H. Bai, Q. Tian, B. Fan, *ACS Appl. Mater. Interfaces* **2014**, *6*, 20585.

[4] E. Della Gaspera, Y. Peng, Q. Hou, L. Spiccia, U. Bach, J. J. Jasieniak, Y. B. Cheng, *Nano Energy* **2015**, *13*, 249.

[5] H. Kanno, N. C. Giebink, Y. Sun, S. R. Forrest, *Appl. Phys. Lett.* **2006**, *89*, 2004.

[6] Y. Hou, X. Du, S. Scheiner, D. P. McMeekin, Z. Wang, N. Li, M. S. Killian, H. Chen, M. Richter, I. Levchuk, N. Schrenker, E. Spiecker, T. Stubhan, N. A. Luechinger, A. Hirsch, P. Schmuki, H. P. Steinrück, R. H. Fink, M. Halik, H. J. Snaith, C. J. Brabec, *Science* **2017**, *358*, 1192.

[7] K. Jiang, F. Wu, G. Zhang, L. Zhu, H. Yan, *Sol. RRL* **2019**, *3*, 1900061.

[8] P. Schulz, J. O. Tiepelt, J. A. Christians, I. Levine, E. Edri, E. M. Sanehira, G. Hodes, D. Cahen, A. Kahn, *ACS Appl. Mater. Interfaces* **2016**, *8*, 31491.

[9] E. M. Sanehira, B. J. Tremolet De Villers, P. Schulz, M. O. Reese, S. Ferrere, K. Zhu, L. Y. Lin, J. J. Berry, J. M. Luther, *ACS Energy Lett.* **2016**, *1*, 38.

[10] J. Tao, J. Xue, H. Guo, Y. Wang, J. Shen, T. Wang, T. He, G. Fu, S. Yang, *Chem. Eng. J.* **2023**, *463*, 142445.

[11] K. Domanski, N. Mine, M. G. Nazeeruddin, Mohammad Khaja Nazeeruddin, Antonio abate, Michael Saliba, Wolfgang Tress, Anders Hagfeldt, **2016**, *10*, 6306.

[12] S. Guarnera, A. Abate, W. Zhang, J. M. Foster, G. Richardson, A. Petrozza, H. J. Snaith, *J. Phys. Chem. Lett.* **2015**, *6*, 432.

[13] G. Tumen-Ulzii, M. Auffray, D. Klotz, G. F. Harrington, X. K. Chen, U. Balijapalli, V. Vediyappan, N. Nakamura, Z. Feng, K. Takekuma, Y. Fujita, P. Wang, S. Yamada, K. Tamada, M. Batmunkh, Y. L. Zhong, F. Mathevet, H. Salway, M. Anaya, S. D. Stranks, T. Matsushima, C. Adachi, *ACS Appl. Energy Mater.* **2022**, *5*, 15819.

[14] C. Eames, J. M. Frost, P. R. F. Barnes, B. C. O'Regan, A. Walsh, M. S. Islam, *Nat. Commun.* **2015**, *6*, 7497.

[15] W. Tress, N. Marinova, T. Moehl, S. M. Zakeeruddin, M. K. Nazeeruddin, M. Grätzel, *Energy Environ. Sci.* **2015**, *8*, 995.

[16] K. Suemori, M. Yokoyama, M. Hiramoto, *J. Appl. Phys.* **2006**, *99*.

[17] E. J. Juarez-Perez, M. Wußler, F. Fabregat-Santiago, K. Lakus-Wollny, E. Mankel, T. Mayer, W. Jaegermann, I. Mora-Sero, *J. Phys. Chem. Lett.* **2014**, *5*, 680.

[18] Z. Hawash, L. K. Ono, S. R. Raga, M. V. Lee, Y. Qi, *Chem. Mater.* **2015**, *27*, 562.

[19] F. Matteocci, Y. Busby, J. J. Pireaux, G. Divitini, S. Cacovich, C. Ducati, A. Di Carlo, *ACS Appl. Mater. Interfaces* **2015**, *7*, 26176.

[20] Q. Jiang, L. Zhang, H. Wang, X. Yang, J. Meng, H. Liu, Z. Yin, J. Wu, X. Zhang, J. You, *Nat. Energy* **2016**, *2*, 16177.

[21] S. Wu, R. Chen, S. Zhang, B. H. Babu, Y. Yue, H. Zhu, Z. Yang, C. Chen, W. Chen, Y. Huang, S. Fang, T. Liu, L. Han, W. Chen, *Nat. Commun.* **2019**, *10*, 1161.

[22] M. Saliba, T. Matsui, J. Y. Seo, K. Domanski, J. P. Correa-Baena, M. K. Nazeeruddin, S. M. Zakeeruddin, W. Tress, A. Abate, A. Hagfeldt, M. Grätzel, *Energy Environ. Sci.* **2016**, *9*, 1989.

[23] R. Wang, J. Xue, L. Meng, J. W. Lee, Z. Zhao, P. Sun, L. Cai, T. Huang, Z. Wang, Z. K. Wang, Y. Duan, J. L. Yang, S. Tan, Y. Yuan, Y. Huang, Y. Yang, *Joule* **2019**, *3*, 1464.

[24] J. W. Lee, Z. Dai, T. H. Han, C. Choi, S. Y. Chang, S. J. Lee, N. De Marco, H. Zhao, P. Sun, Y. Huang, Y. Yang, *Nat. Commun.* **2018**, *9*, 3021.

[25] G. Tumen-ulzii, M. Auffray, T. Matsushima, C. Adachi, *Appl. Phys. Lett.* **2021**, *118*, 241603.

[26] K. Kanai, K. Koizumi, S. Ouchi, Y. Tsukamoto, K. Sakanoue, *Org. Electron.* **2010**, *11*, 188.

[27] F. Wang, X. Qiao, T. Xiong, D. Ma, *Org. Electron.* **2008**, *9*, 985.

[28] J. Seifter, Y. Sun, H. Choi, B. H. Lee, T. L. Nguyen, H. Y. Woo, A. J. Heeger, *Adv. Mater.* **2015**, *27*, 4989.

[29] W. Xu, L. Zheng, X. Zhang, Y. Cao, T. Meng, D. Wu, L. Liu, W. Hu, X. Gong, *Adv. Energy Mater.* **2018**, *8*, 1703178.

[30] M. Yahiro, S. Sugawara, S. Maeda, Y. Shimoi, P. Wang, S. I. Kobayashi, K. Takekuma, G. Tumen-Ulzii, C. Qin, T. Matsushima, T. Isaji, Y. Kasai, T. Fujihara, C. Adachi, *ACS Appl. Energy Mater.* **2021**, *4*, 14590.

[31] E. Voroshazi, B. Verreet, A. Buri, R. Müller, D. Di Nuzzo, P. Heremans, *Org. Electron.* **2011**, *12*, 736.

[32] I. Deretzis, E. Smecca, G. Mannino, A. La Magna, T. Miyasaka, A. Alberti, *J. Phys. Chem. Lett.* **2018**, *9*, 3000.

[33] D. Wang, M. Wright, N. K. Elumalai, A. Uddin, *Sol. Energy Mater. Sol. Cells* **2016**, *147*, 255.

[34] C. Ding, L. Yin, L. Zhang, R. Huang, S. Fan, Q. Luo, J. Lin, F. Li, C. Zhao, R. Österbacka, C. Q. Ma, *Adv. Funct. Mater.* **2021**, *31*, 2103820.

[35] E. Bi, Z. Song, C. Li, Z. Wu, Y. Yan, *Trends Chem.* **2021**, *3*, 575.

[36] T. Bu, J. Li, F. Zheng, W. Chen, X. Wen, Z. Ku, Y. Peng, J. Zhong, Y. B. Cheng, F. Huang, *Nat. Commun.* **2018**, *9*, 1.

CHAPTER 4

Improvement of Electrical Conductivity in $CsSnI_3$ Perovskite for Thermoelectric Application

Chapter 4: Improvement of Electrical Conductivity in $CsSnI_3$ Perovskite for Thermoelectric Application

4.1 Introduction

While HPs have ultralow κ and high *S*, their PF and ZT values generally remain low due to their low σ. In comparison to state-of-the-art inorganic TE materials such as Bi_2Te_3, Cu_2S, SnSe, and lead chalcogenides, where ZT values typically exceed 1, HPs currently lag behind.[1–3] Organics and hybrids typically achieve ZT values between 0.4 and 0.6.[4,5] The highest ZT has currently been reported around ≈0.19 for $FASnI_3$ perovskite.[6] However, the instability of organic cation-based HPs poses a major hurdle for TE performances, requiring significant efforts to overcome. When compared with MA^+ or FA^+, Cs^+ is smaller in size which leads to rotation and tilt of BX_6 octahedral. This tilt influences the structural stability of the black orthorhombic (B-γ) $CsSnI_3$ at room temperature.[7] Therefore, the B-γ phase of $CsSnI_3$ perovskite is most suitable for device applications. In terms of B-site, Sn-based perovskites have relatively higher σ compared to other types of perovskites, which is achieved by the marginal crossing of Sn 5s and Sn 5p bands near the Brillouin zone boundary.[7] Additionally, the oxidation from Sn^{2+} to Sn^{4+} provides an additional advantage for p-type self-doping, thus enhancing their electronic properties.[8,9] This combination renders $CsSnI_3$ a particularly promising candidate for further exploration in TE applications. However, further improvements are required in the σ of $CsSnI_3$ to achieve a higher ZT value, consequently enhancing its overall TE performance. Therefore, I propose to dope molecular dopants into $CsSnI_3$ thin film to increase the carrier concentration of the $CsSnI_3$ perovskite in this study. With improved stability and decent performance, $CsSnI_3$ can be used as a p-type material for applications such as low-grade heat recovery and electronic devices with low power requirements. Low-temperature processed solution-based TE materials hold significant promise for wearable and household purposes.[10]

4.2 Results and Discussion

The solution-coating process is a suitable method for active film preparation due to its simplicity in fabrication and relatively low cost. The conventional mixture solvent of the DMSO and DMF was used to prepare the precursor solution. $CsSnI_3$ thin film was prepared by spin-coating from the precursor solution and was further annealed at 120°C to attain the crystallization. The crystallization of $CsSnI_3$ film was validated by the XRD pattern as shown in **Figure 4-1**. The orthorhombic *Pnma* space group of $CsSnI_3$ crystals in the thin films is confirmed through the 2θ peak positions from the XRD pattern.[11] The observed dominant diffraction patterns are located at 14.45°, 20.57°, 22.99°, 24.12°, and 29.15°, corresponding to the planes of (020)(101), (200)(121), (201)(102), (031)(211), (220)(022), and (202), respectively, which is accordance with the previously reported literature.[11] Notably, no secondary phase was detected in the XRD pattern.

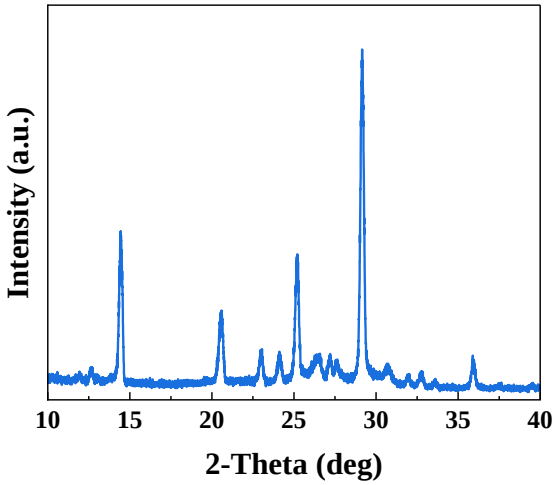

Figure 4-1. XRD pattern of a $CsSnI_3$ thin film.

Furthermore, the TE parameters, such as the Seebeck coefficient and thermal conductivity, of the $CsSnI_3$ thin film were measured. The Seebeck coefficient of the $CsSnI_3$ thin film was determined to be 45.8 μV K^{-1}. This value was obtained by averaging the values measured using alumel and chromel wires at room temperature (**Figure 4-2a**). The positive values indicate that carriers in $CsSnI_3$ are positively charged and the material exhibits a p-type conductivity. The value of thermal conductivity was estimated by the differential 3-w method (**Figure 4-2b**) and was found to be 0.6 μW $m^{-1}K^{-1}$. It is important to note that the thermal conductivity was measured out–of–plane while the Seebeck coefficient was measured in–plane direction of the film.

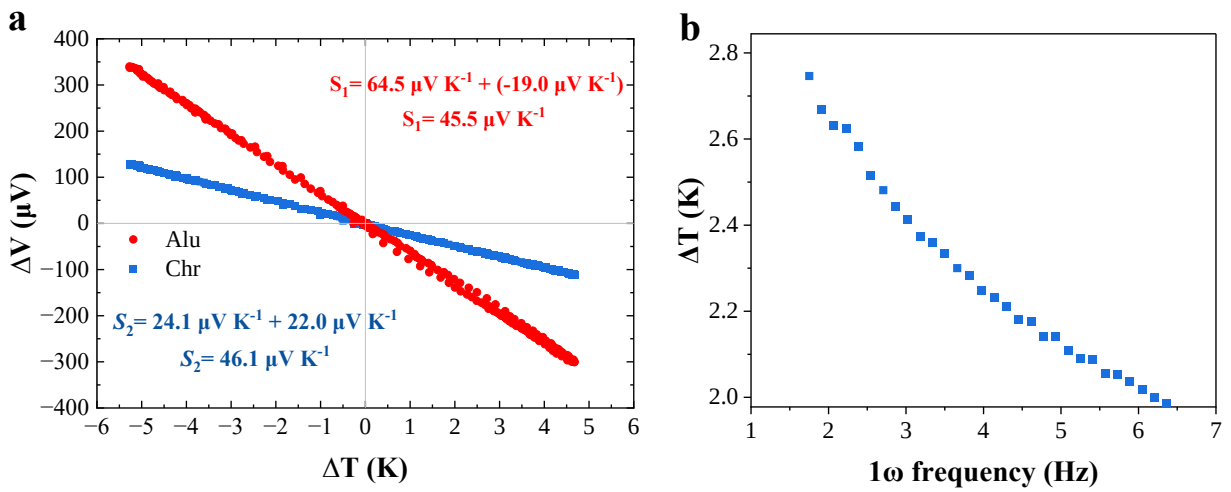

Figure 4-2. (a) TE voltage as a function of temperature difference for $CsSnI_3$ thin film. Red and blue curves are measured through alumel and chromel wires, respectively. (b) Temperature amplitude as a function of modulation frequency for $CsSnI_3$ thin film.

Current-voltage (*I*–*V*) curves of $CsSnI_3$ thin films are shown in **Figure 4-3**. The σ was calculated as 2.46 S cm^{-1} from the *I*–*V* curves of the thin film prepared from the precursor solution stirred for 2 h in the nitrogen–filled glove box (orange *I*–*V* curve in **Figure 4-3**), which was significantly lower than the previously reported value.[12] It has been reported that DMSO solvent conventionally used in fabrication of perovskite film can oxidize Sn^{2+} to Sn^{4+} in solution even in an inert atmosphere.[16] Saidaminov *et al.* found that the DMSO / Sn^{2+} pair undergoes an irreversible redox reaction forming dimethylsulfide (DMS) and Sn^{4+} as shown below.

$$2SnI_2 + 2(CH_3)_2SO \rightarrow SnO_2 + SnI_4 + 2(CH_3)_2S$$

Moreover, Fan *et al.* detected the higher amount of Sn^{4+} in perovskite films fabricated with precursor solution placed in glovebox for two weeks compared to that in films fabricated with fresh solution.[17] Therefore, there is a possibility that very low amount of oxygen even in a glove box could also induce oxidation of Sn^{2+} to Sn^{4+}. Therefore, I increased the aging time of the precursor solution from 2 h to 12 h to promote the oxidation of Sn^{2+} to Sn^{4+}. As a result, longer aging of the precursor solution led to a notable increase in σ, reaching 80 S cm^{-1} (blue *I*–*V* curve in **Figure 4-3**). Therefore, the precursor solution aged for 12 h was used for further experiments.

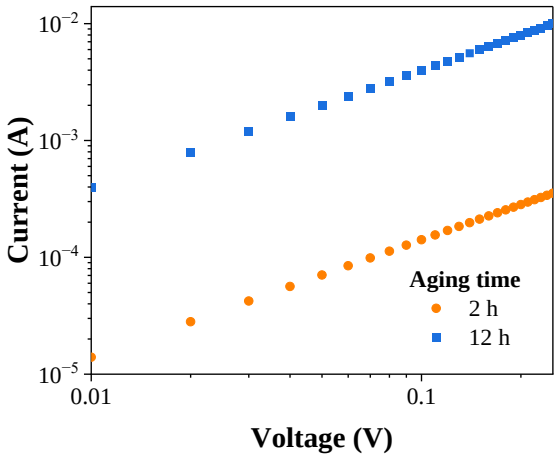

Figure 4-3. *I–V* curves of $CsSnI_3$ perovskite thin films prepared from precursor solution aged for different durations.

Furthermore, the VB edge level of a $CsSnI_3$ perovskite thin film was measured as –4.9 eV as shown in **Figure 4-3a**. The molecular dopants with high electron affinity, such as F_4–TCNQ and 1,3,4,5,7,8-hexafluoro-tetracyanonaphthoquinodimethane (F_6–TCNNQ), were utilized to facilitate charge transfer between the molecular dopant and the perovskite host (**Figure 4-3b**). F_4–TCNQ and F_6–TCNNQ are common molecular dopants used to boost the electrical conductivities of organic materials.[13,14] The same concentration of the molecular dopants (0.01 mg ml^{-1}) were directly introduced into the precursor solution of perovskite.

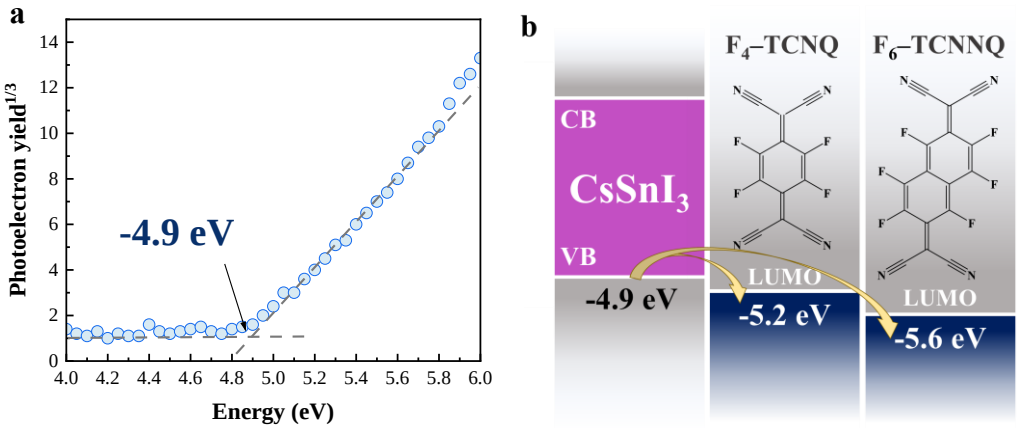

Figure 4-3. (a) PEYS result of $CsSnI_3$ perovskite films. (b) Energy diagram of the $CsSnI_3$ perovskite host and molecular p-dopants, illustrating charge transfer from the top of the perovskite VB to the LUMO of the dopants.

Figure 4-4a displays the *I–V* curves of the $CsSnI_3$ thin films doped with F_4–TCNQ and F_6–TCNNQ. Several samples have been measured for each dopant. The corresponding σ values, derived from the *I–V* curves, are presented in **Figure 4-4b**. With the introduction of F_4–TCNQ and F_6–TCNNQ dopants, the σ showed an increase to some extent from an average value of ~50.75 S

cm^{-1} to ~60.46 S cm^{-1} and ~71.91 S cm^{-1}, respectively. The notable enhancement in σ with F_6–TCNNQ could be attributed to its combination of higher charge carrier mobilities and higher doping strength compared to F_4–TCNQ, resulting in a higher charge carrier concentration.[15] However, this improvement was still insufficient.

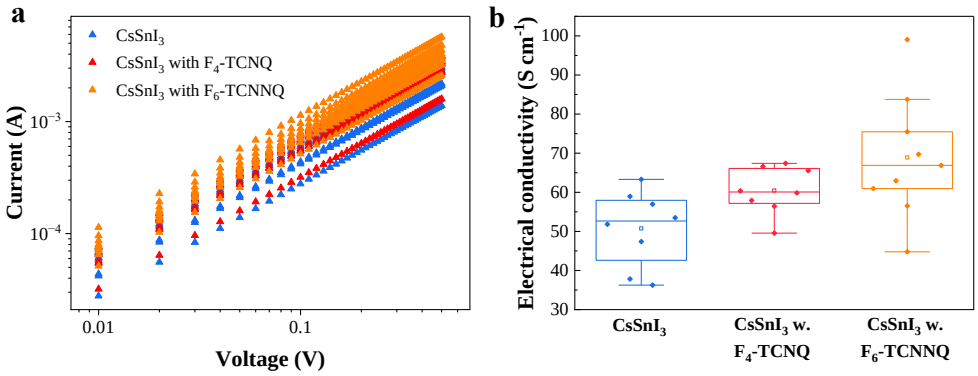

Figure 4-4. (a) *I–V* curves and (b) box plots of the pristine and F_4–TCNQ and F_6–TNNQ doped $CsSnI_3$ perovskite thin films. The box plots from (b) indicate the maximum and minimum values (whiskers), the upper quartile and lower quartile (box), and the mean value (median line).

Furthermore, σ measurements were conducted on $CsSnI_3$ thin films with a higher concentration of F_6–TCNNQ dopant (**Figure 4-5**). However, no notable difference was observed in enhancement with increasing the dopant concentration. The improvement remained almost consistent across all concentrations tested. I assumed that dopants predominantly get enriched at the grain boundaries and surround grains since their molecular size is too large to enter within the grains of the perovskite films. Therefore, it becomes imperative to design the molecular structure of the dopant to facilitate its entry into the grain interior, thereby promoting enhanced charge transfer between the dopant and the perovskite host.

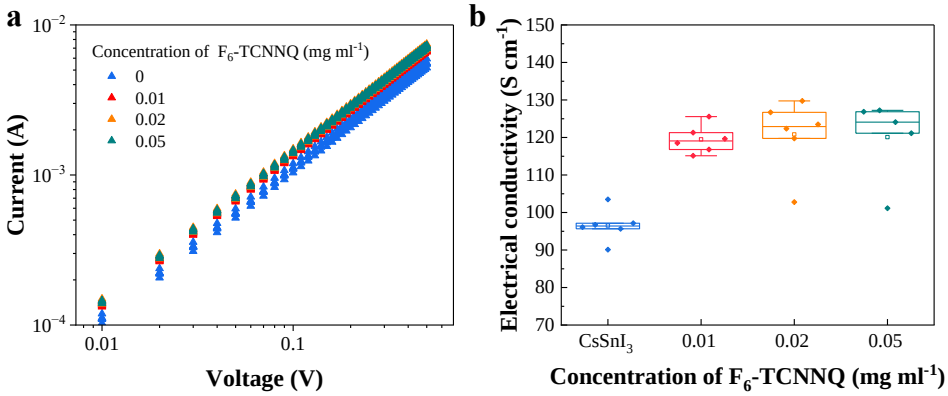

Figure 4-5. (a) *I–V* curves and (b) box plots of the pristine $CsSnI_3$ perovskite thin films and those doped with different concentrations of F_6–TNNQ.

4.3 Conclusion

The longer aging of the $CsSnI_3$ precursor solution led to a significant increase in σ due to the oxidation of Sn^{2+} to Sn^{4+}. The F_6-TCNNQ dopant improved the σ of $CsSnI_3$ more compared to F_4-TCNQ. However, this improvement remained almost consistent across various concentrations and was still insufficient. I hypothesized that dopants located at grain boundaries due to their large molecular size, hindered their entry into the interior of perovskite grains. Thus, it is essential to design the molecular structure of dopants to facilitate their penetration into the grain interior.

4.4 Experimental Section/Methods

4.4.1 Materials

The precursor materials, such as CsI and tin iodide (SnI_2) for the perovskite thin film fabrication, were purchased from Sigma-Aldrich. F_4-TCNQ and F_6-TCNNQ dopants were purchased from Tokyo Chemical Industry. DMF, DMSO, and toluene solvents were purchased from Fujifilm Wako Chemicals. These purchased materials were used without further purification.

4.4.2 Film Fabrication

Glass substrates were cleaned sequentially in detergent, pure water, acetone, and isopropanol with ultrasonication each for 15 min. Then, the substrates were subjected to UV–ozone treatment for 15 min. The perovskite precursor solution was prepared by dissolving CsI (0.5 M) and SnI_2 (0.5 M) in a solvent mixture (DMF:DMSO = 4:1). F_4-TCNQ (0.01 mg ml^{-1}) and F_6-TCNNQ (0.01–0.05 mg ml^{-1}) solution in DMF was added to the aforementioned precursor solution. The precursor solution was stirred at 70 °C for 2 h and 12 h and filtered through a 0.2 μm PTFE membrane before use. A perovskite layer was spin–coated from the precursor solution on a glass substrate at 4,000 rpm for 50 s. 250 μL of toluene was dropped on the substrate at 10 s after starting substrate rotation, and then the perovskite layer was annealed at 130 °C for 20 min. The film crystallization growth was confirmed following the annealing, where the $CsSnI_3$ color change was observed from initial yellow to dark brown. The film fabrication was carried out in a nitrogen–filled glove box. Finally, 70–nm–thick gold electrode was thermally deposited through metal shadow masks in a vacuum for *I–V* curve measurements. The vacuum pressure was on the order

of 10^{-4} Pa and the gold evaporation rate was ~0.1 nm s^{-1}. The shadow mask with a 3 mm gap and 23 mm width was used for the electrode evaporation.

4.4.3 Characterization and Measurements

The *I–V* curve measurements were performed on the samples using a 2-probe method under vacuum with forward and reverse scans (semiconductor parameter analyzer, B1500A or 4156C, Agilent Technologies) in a vacuum. The thickness of the perovskite film measured with a surface profilometer (DektakXT, Bruker) was ~150 nm.

The structural properties of the perovskite layers were analyzed with an XRD system using a typical 2 θ/θ technique [λ = 1.54 Å (CuKα)] (SmartLab, Rigaku). The energy level measurements were carried out on the $CsSnI_3$ perovskite layer fabricated on an ITO–coated glass substrate using the same conditions mentioned earlier with photoelectron yield spectroscopy (AC–3, Rikenkeiki).

For thermal conductivity measurement, a 150 nm MoO_3 insulating layer was thermally deposited on a glass/perovskite sample. The vacuum pressure was on the order of 10^{-4} Pa and the evaporation rate was ~0.1 nm s^{-1}. Further 70 nm thick Au was thermally grown over MoO_3 in a pattern to make the conducting contact. The cross-plane thermal conductivity was measured on the sample using a differential 3ω method.

References

[1] I. T. Witting, T. C. Chasapis, F. Ricci, M. Peters, N. A. Heinz, G. Hautier, G. J. Snyder, *Adv. Electron. Mater.* **2019**, *5*, 1800904.

[2] Y. He, T. Day, T. Zhang, H. Liu, X. Shi, L. Chen, G. J. Snyder, *Adv. Mater.* **2014**, *23*, 3974.

[3] L.-D. Zhao, S.-H. Lo, Y. Zhang, H. Sun, G. Tan, C. Uher, C. Wolverton, V. P. Dravid, M. G. Kanatzidis, *Nature* **2014**, *508*, 373.

[4] G.-H. Kim, L. Shao, K. Zhang, K. P. Pipe, *Nat. Mater.* **2013**, *12*, 719.

[5] L. Wang, Z. Zhang, Y. Liu, B. Wang, L. Fang, J. Qiu, K. Zhang, S. Wang, *Nat. Commun.* **2018**, *9*, 3817.

[6] L. Zheng, T. Zhu, Y. Li, H. Wu, C. Yi, J. Zhu, X. Gong, *J. Mater. Chem. A* **2020**, *8*, 25431.

[7] T. H. Chowdhury, Y. Reo, A. R. B. M. Yusoff, Y. Y. Noh, *Adv. Sci.* **2022**, *9*, 1.

[8] S. Gupta, D. Cahen, G. Hodes, *J. Phys. Chem. C* **2018**, *122*, 13926.

[9] D. Ricciarelli, D. Meggiolaro, F. Ambrosio, F. De Angelis, *ACS Energy Lett.* **2020**, *5*, 2787.

[10] G. Schierning, *Nat. Energy* **2018**, *3*, 92.

[11] Y. Zhou, H. F. Garces, B. S. Senturk, A. L. Ortiz, N. P. Padture, *Mater. Lett.* **2013**, *110*, 127.

[12] S. Saini, A. K. Baranwal, T. Yabuki, S. Hayase, K. Miyazaki, *MRS Adv.* **2019**, *4*, 1719.

[13] T. Takenobu, T. Takano, M. Shiraishi, Y. Murakami, M. Ata, H. Kataura, Y. Achiba, Y. Iwasa, *Nat. Mater.* **2003**, *2*, 683.

[14] T. Takenobu, T. Kanbara, N. Akima, T. Takahashi, M. Shiraishi, K. Tsukagoshi, H. Kataura, Y. Aoyagi, Y. Iwasa, *Adv. Mater.* **2005**, *17*, 2430.

[15] V. Vijayakumar, P. Durand, H. Zeng, V. Untilova, L. Herrmann, P. Algayer, N. Leclerc, M. Brinkmann, *J. Mater. Chem. C* **2020**, *8*, 16470.

[16] M. I. Saidaminov, I. Spanopoulos, J. Abed, W. Ke, J. Wicks, M. G. Kanatzidis, E. H. Sargent, *ACS Energy Lett.* **2020**, *5*, 1153.

[17] F. Hu, C. H. Chen, Y. H. Lou, T. Y. Teng, Y. R. Shi, Y. Xia, K. L. Wang, J. Chen, Z. K. Wang, L. S. Liao, *J. Mater. Chem. A* **2023**, *11*, 4579.

CHAPTER 5

Conclusions and Perspectives

Chapter 5: Conclusions and Perspectives

5.1 Conclusions

Throughout this thesis, the primary focus has been twofold: understanding the obstacles hindering the performance of perovskite material–based solar cells and overcoming these challenges, followed by exploring the potential of HP materials in TE applications.

In Chapter 2, to elucidate the details of PSC degradation mechanisms, the effect of ambient air exposure on long–term device durability was investigated. I found that one of the critical reasons for the air–induced PSC degradation is the doping of the spiro–OMeTAD HTL with oxygen. The hole transport level of the spiro–OMeTAD layer became deeper by oxygen doping, increasing an energy barrier for hole extraction. In other words, decreased hole extraction at the perovskite / spiro–OMeTAD interface induced the degradation of PSCs in air. However, it was found that this oxygen–induced degradation of PSCs is reversible to some extent by storing PSCs in a vacuum. On the other hand, no detectable degradation of the perovskite light absorber was observed after ~600 h of air exposure from the results of morphological and structural characterizations. These aspects provide a deeper understanding of PSC degradation, giving insight into improving long–term durability in air in the future.

In Chapter 3, to improve the initial PCE of PSCs by suppressing carrier recombination, a robust MoO_x interlayer was introduced between the spiro–OMeTAD HTL and the Au electrode. It was found that the vacuum deposition of Au onto the organic HTL results in Au penetration into the perovskite layer. This Au penetration proved to be a limiting factor in PCE due to detrimental carrier recombination caused by the penetrated Au component inside the perovskite light absorber. Introducing a thin MoO_x interlayer between the HTL and the Au electrode, effectively reduced the Au penetration, suppressing the detrimental carrier recombination by Au. Consequently, this MoO_x introduction increased PCEs from ~16.9% to ~19.6% by ~2.7%. Furthermore, using the MoO_x interlayer improved the long–term durability of PSCs. These findings are crucial in elucidating a basic mechanism that limits initial PCEs and in advancing the fabrication of PSC products with even higher performance.

In Chapter 4, to improve the electrical conductivity of $CsSnI_3$ perovskite, the molecular dopants, such as F_6–TCNNQ and F_4–TCNQ dopants was introduced. While these dopants did contribute to an increase in electrical conductivity to some degree, their effectiveness was limited.

This limitation is due to the large molecular size of the dopants, which hindered their penetration into the interior of the perovskite grains, thereby restricting their ability to facilitate significant improvement in conductivity.

Overall, the investigations of PSCs delved into the complexities of their degradation mechanisms under various environmental conditions. By uncovering the critical effect of oxygen doping in the spiro-OMeTAD hole transport layer and its impact on long-term durability, the crucial insights were gained for developing more air-stable PSCs in the future. Moreover, there was no detectable degradation in perovskite films after a long time of air exposure. Furthermore, the exploration of strategies to mitigate Au penetration-induced carrier recombination, such as the introduction of a MoO_x interlayer, led to significant improvements in the initial PCEs of PSCs. These findings suggest that the perovskite material exhibits considerable stability on its own. The instability and low initial PCE of PSCs are not solely attributed to the properties of the perovskite material itself. Rather, they are influenced by the degradation of other functional layers or their interactions within the solar cell architecture. Building upon this foundation, I then turned my attention to the potential of HPs in TE applications. Despite their promising attributes, such as ultralow thermal conductivity and high Seebeck coefficient, HPs face challenges in overall TE performance due to their relatively low electrical conductivity. Through the investigation, I aimed at addressing these limitations by molecular doping and unlock the full TE potential of HPs. However, the improvement in the electrical conductivity was insufficient. Therefore, further exploration of different molecular structures is necessary.

5.2 Perspectives

5.2.1 Understanding the Degradation Mechanism in PSCs

In Chapter 3, although significant progress has been achieved in enhancing the PCE and long-term durability of PSCs through the incorporation of a MoO_x interlayer, the degradation mechanisms of encapsulated PSC devices under continuous light illumination remain inadequately understood. This gap in knowledge is crucial because understanding and mitigating these degradation pathways are essential for the development of PSCs with long-term operational stability. Therefore, it is necessary to focus on elucidating the unknown mechanisms behind the degradation, which was suppressed by the MoO_x interlayer. In Chapter 3, particularly in Figure 3-5, It was observed that in the absence of the MoO_x interlayer, I^- and CN^- traces were detected at

the interface between the HTL and the Au electrode. The presence of these species is a significant indicator of chemical interactions that could lead to device degradation. Interestingly, the MoO_x interlayer effectively blocked the migration of these ions, preventing their accumulation at the interface.

It is hypothesized that the suppression of ion migration by the MoO_x interlayer plays a crucial role in enhancing the long-term stability of PSCs. Specifically, the migration of I^- and FA^+ or MA^+ cations is likely a key factor influencing the degradation process. These ions may interact with the Au electrode or affect the contact between HTL and Au electrode, leading to the formation of deleterious compounds that degrade the device performance over time. By preventing this migration, the MoO_x interlayer helps maintain the integrity of the interfacial region, thereby enhancing the device's durability.

To further investigate these phenomena, it is necessary to employ advanced characterization techniques such as ToF-SIMS and X-ray photoelectron spectroscopy (XPS) to analyze the chemical composition and distribution of elements at the interfaces. The intermediate interfacial chemical and structural changes during the degradation cannot be completely detected by ex-situ characterizations, but in situ characterization techniques can achieve this goal. Therefore, more accurate in-situ studies will be conducted under continuous light illumination to trace the evolution of the interfacial chemistry based on ex-situ characterization techniques. These studies will help us understand the precise role of the MoO_x interlayer in inhibiting ion migration and elucidate the degradation pathways that occur in its absence. Ultimately, this research aims to provide a comprehensive understanding of the degradation mechanisms in PSCs and develop strategies to further enhance their long-term operational stability. By addressing these challenges, it is possible to pave the way for the commercialization of PSC technology, offering a viable solution for sustainable and efficient solar energy conversion.

5.2.2 Designing the Molecular Dopant

Given that the improvement in electrical conductivity induced by molecular dopants remains relatively consistent across various dopant concentrations, it becomes imperative to strategically design the molecular structure of these dopants to enhance their effectiveness. The current hypothesis is that the large molecular size of the dopants causes them to primarily localize at the grain boundaries of the perovskite material. This localization potentially impedes their penetration into the interior of the perovskite grains, limiting their overall efficacy in improving electrical conductivity.

To address this limitation, an approach is proposed to introduce the dopant molecules into the perovskite grains more effectively. This can be achieved by modifying the molecular structure of the dopants to facilitate their incorporation into the perovskite matrix. Specifically, I suggest substituting the amine group in the dopant molecule, as illustrated in **Figure 5.1**. The rationale behind this modification is that the amine group can be integrated into the inorganic skeleton of the perovskite structure through strong electrostatic and van der Waals interactions.[1] These interactions can provide a robust means for the dopant molecules to be embedded within the perovskite grains rather than merely residing at the grain boundaries. The incorporation of dopant molecules into the grains themselves could significantly enhance the electrical properties of the perovskite material. By being uniformly distributed throughout the grain structure, the dopants can contribute more effectively to charge transport. This uniform distribution is expected to result in a more substantial and consistent improvement in electrical conductivity across the material.

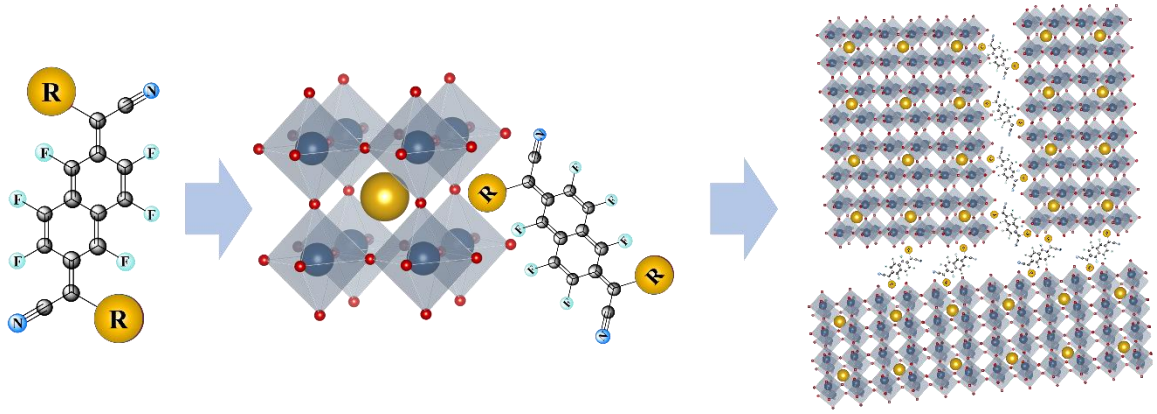

Figure 5.1 Schematic illustration of molecular doping.

Moreover, layer-structured low dimensional (2D or quasi 2D) HP, created by isolating the corner-sharing lead halide octahedra sheets ($[PbX_6]_4^-$) with long chain spacer organic cations,

possess ultra-low thermal conductivity and high Seebeck coefficient as well. Due to quantum confinement effects, these low-dimensional structures have a different density of states (DOS) distribution compared to 3D, which increases the Seebeck coefficient without decreasing electrical conductivity.[2] Additionally, bulkier and more hydrophobic organic spacers can better protect the perovskite sublayers from water and oxygen.[3] As a result, 2D and quasi-2D HPs typically exhibit greater environmental stability than their 3D counterparts.[4,5] However, low dimensional HP materials have not yet been extensively studied for TE applications. Therefore, it would be worthwhile to explore the thermoelectric properties of low dimensional HPs. Especially, by incorporation of bulky acceptor like organic moieties, charge transfer from the perovskite sublayers can be improved, thereby increasing the carrier concentration and mobility. The amine group substituted dopant molecules proposed above can be used as a spacer. In addition to acceptor moieties for p-type doping, this strategy can also be extended to n-type doping by incorporating donor-like organic spacers. By selecting appropriate donor molecules and integrating amine group, it is possible to inject electrons into the conduction band of the perovskite sublayers, thereby increasing electron concentration and improving n-type conductivity. This dual capability of using both acceptor and donor spacers expands the versatility of low dimensional HPs, enabling the development of both p-type and n-type materials tailored for specific TE applications.

To validate those hypotheses, a series of dopant molecules with varying molecular structures, particularly focusing on those with amine group substitutions, will be synthesized. The techniques such as XPS and XRD will be employed to analyze the incorporation of dopants and spacers in perovskite structure and to determine crystal structure. Additionally, the electrical conductivity measurements will be used to assess the performance improvements achieved through this modified structure. By advancing the understanding of dopant/spacer incorporation at the molecular level and developing more effective dopant/spacer designs, it is possible to achieve significant enhancements in the electrical properties of perovskite materials. This research has the potential to contribute to the development of more efficient and stable perovskite-based devices, paving the way for their widespread application in optoelectronics and renewable energy technologies.

References

[1] A. Oranskaia, U. Schwingenschlögl, *Adv. Energy Mater.* **2019**, *9*, 1.

[2] S. Hu, Z. Ren, A. B. Djurisic, A. L. Rogach, *ACS Energy Lett.* **2021**, *6*, 3882.

[3] S. Yang, Y. Wang, P. Liu, Y.-B. Cheng, H. J. Zhao, H. G. Yang, *Nat. Energy* **2016**, *1*, 1.

[4] I. C. Smith, E. T. Hoke, D. Solis-Ibarra, M. D. McGehee, H. I. Karunadasa, *Angew. Chemie Int. Ed.* **2014**, *53*, 11232.

[5] A. R. bin M. Yusoff, M. K. Nazeeruddin, *Adv. Energy Mater.* **2018**, *8*, 1702073.

Appendix

A–1. Calculation of Spiro–OMeTAD$^+$ Cations Concentration

The hole concentration (n) in chemically doped spiro–OMeTAD films was calculated using the following equation, $\sigma = nq\mu$, where σ is the electrical conductivity, q is the elementary charge ($1.60217663 \times 10^{-19}$ C), and μ is the hole mobility. To calculate n, I took the reported hole mobility μ of doped spiro–OMeTAD films (1.6×10^{-3} cm^2 V^{-1} s^{-1})[A1] and the σ from **Figure 2–8**. The calculated n values were 4.6×10^{16} cm^{-3} for fresh films and 9.5×10^{16} cm^{-3} for films exposed to air for ~600 h. The n values are roughly equivalent to the spiro–OMeTAD$^+$ cation concentration in films. Meanwhile, the molecular density of spiro–OMeTAD films was determined to be 8.9×10^{20} cm^{-3} from its film density (1.82 g cm^{-3})[A2] and molecular weight ($M_w = 1225$). Based on those values, the ratios of the spiro–OMeTAD$^+$ cation number to the neutral spiro–OMeTAD number were found to be ~0.005% for fresh films and ~0.011% for air–exposed films.

A–2. Long–Term Stability Variation

Figure A1 shows long–term stability variations in PSCs without and with the 15–nm–thick MoO_x interlayer, even when employing the same device architectures. Even though there is a variation in stability, all PSCs with the interlayer showed improved stability compared to reference PSCs without the interlayer.

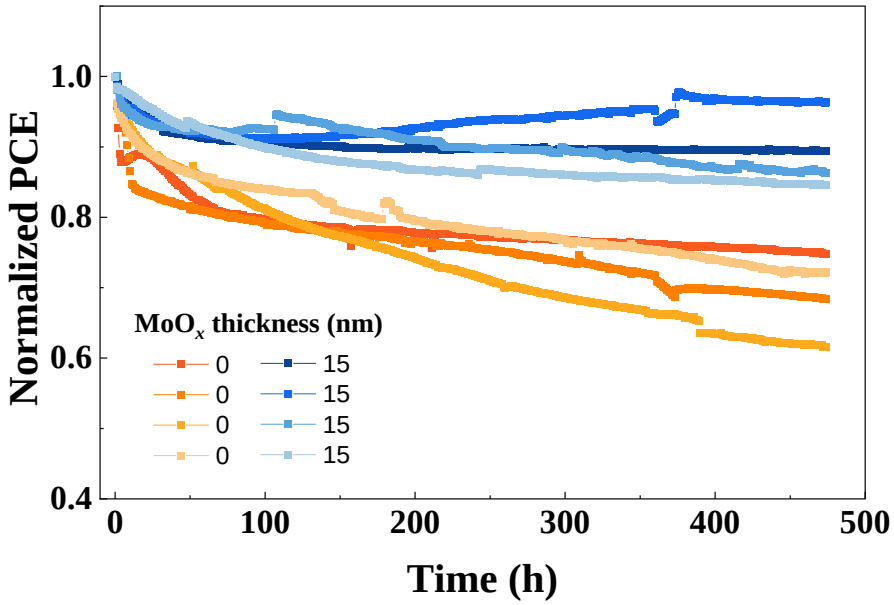

Figure A1. Time evolution of normalized PCE of PSCs without and with the 15–nm–thick MoO_x interlayer.

A–3. Encapsulation

For the encapsulation, a glass cap was used as a cover, while the epoxy resin was used as an edge sealant, and a desiccant sheet was also used. Even after the high–humidity high–temperature storage, the OLED performance degradation was negligible. This indicates that the encapsulation method used here is highly reliable even during the PSC operational durability measurements.

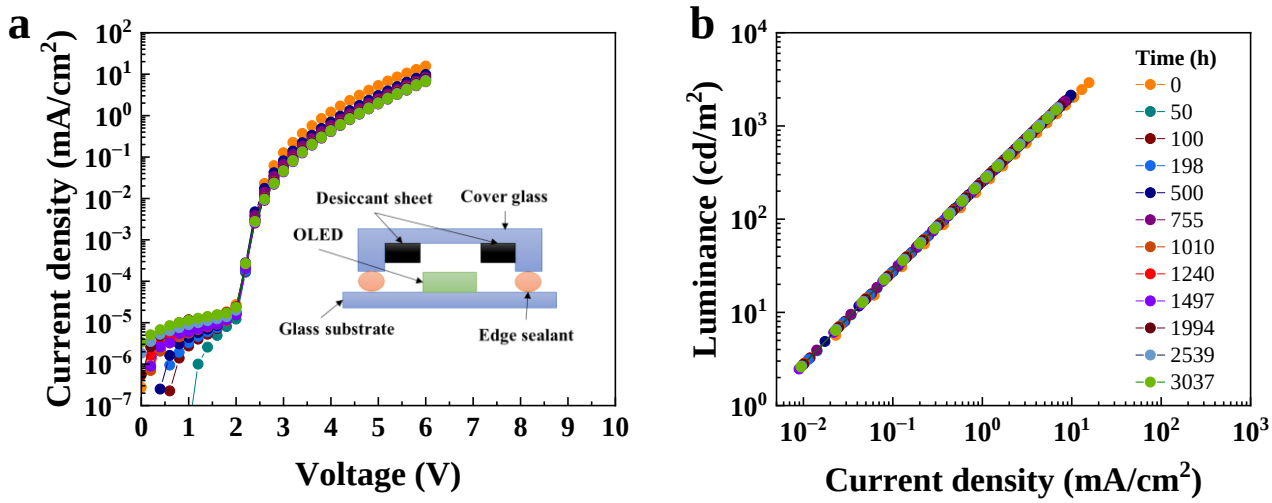

Figure A2. (a) $J-V$ and (b) $L-J$ curves of OLEDs with a certain structure when stored at a relative humidity of 85% and a temperature of 85ºC, and their $J-V$ and $L-J$ curves were periodically measured for ~3,000 hours. The inset of (a) is a schematic of the encapsulation used for OLEDs.

References (Appendix)

[A1] H. J. Snaith, M. Grätzel, Appl. Phys. Lett 2006, 89, 262114.

[A2] I. K. Ding, N. Tétreault, J. Brillet, B. E. Hardin, E. H. Smith, S. J. Rosenthal, F. Sauvage, M. Grätzel, M. D. McGehee, Adv. Funct. Mater. 2009, 19, 2431.

List of Chemical Compounds

Spiro–MeOTAD	2,2′,7,7′-tetrakis(*N*,*N*-di-*p*-methoxyphenylamine)-9,9′-spirobi-fluorene
4–tBP	4–tert–butylpyridine
LiTFSI	Bis(trifluoromethane)–sulfonimide lithium
FK–209	Tris(2–(1Hpyrazol–1–yl)–4–*tert*–butylpyridine) cobalt(III)tris–(bis(trifluoromethane)sulfonimide)
TCNQ	Tetracyanoquinodimethane
F_4–TCNQ	2,3,5,6–tetrafluorotetracyanoquinodimethane
F_6–TCNNQ	1,3,4,5,7,8-hexafluoro-tetracyanonaphthoquinodimethane
BQ	Benzoquinone
MoO_x	Molybdenum oxide
Au	Gold
SnO_2	Tin(IV) oxide
CsI	Cesium iodide
FAI	Formamidinium iodide
MABr	Methylammonium bromide
PbI_2	Lead iodide
$PbBr_2$	Lead bromide
DMF	Dimethylformamide
DMSO	Dimethyl sulfoxide
PyCz	Pyridine–carbazole
KOH	Potassium hydroxide
SnI_2	Tin iodide

List of Abbreviations

HPs	Halide perovskites
PV	Photovoltaic
TE	Thermoelectric
DOS	Density of states
VB	Valence band
CB	Conduction band
JDOS	Joint density of states
PL	Photoluminescence
FA	Formamidinium
MA	Methylammonium
V_{Sn}	Tin vacancies
V_{MA}	Vacancy of methylammonium
PCE	Power conversion efficiency
PSCs	Perovskite solar cells
ETL	Electron transport layer
HTL	Hole transport layer
HOMO	Highest occupied molecular orbital
LUMO	Lowest unoccupied molecular orbital
AM1.5G	Air mass 1.5 global
MPP	Maximum power point
DSSCs	Dye–sensitized solar cells
SEM	Scanning electron microscope
IPCE	Integration of an incident–photon–to–current efficiency
TPV	Transient photovoltage
TPC	Transient photocurrent

HODs	Hole–only devices
PEYS	Photoelectron yield spectroscopy
VL	Vacuum level
FTIR	Fourier transform infrared
QCM	Quartz crystal microbalance
CB	Chlorobenzene
XRD	X–ray diffraction
ToF–SIMS	Time–of–flight secondary ion mass spectroscopy
XPS	X-ray photoelectron spectroscopy
OLED	Organic light–emitting diode

List of Symbols

t	Tolerance factor
κ	Thermal conductivity
S	Seebeck coefficient
α	Absorption coefficient
σ	Electrical conductivity
J	Current density
V	Voltage
P	Output power
J_{SC}	Short–circuit current density
V_{OC}	Open-circuit voltage
MPP	Maximum power point
P_{max}	Maximum output power
FF	Fill factor
E_F	Fermi level
ZT	Figure of merit
T	Temperature
T_g	Glass transition temperature
q	Elementary charge
μ	Carrier mobility
M_w	Molecular weight

Publication List

Original Papers:

1) **Purev-Ochir B.**, Liu X., Fujita Y., Semba D., Raju T. B., Tumen-Ulzii G., Wachi A., Sato H., Matsushima T., Adachi C., "Oxygen-Induced Reversible Degradation of Perovskite Solar Cells", ***Solar RRL***, 7, 2300127 (2023).

2) **Purev-Ochir B.**, Song J. T., Wang P., Yahiro M., Yamada S., Nakanotani H., Matsushima T., Adachi C., "Suppressed Gold Penetration with The Molybdenum Oxide Interlayer to Increase Power Conversion Efficiency of Perovskite Solar Cells", ***Solar RRL***, 8, 2400029 (2024).

Joint paper:

1) Fujita Y., Tumen-Ulzii G., Semba D., **Purev-Ochir B.**, Nakamura N., Raju T. B., Matsushima T., Adachi C., "Greatly Improved High-Temperature Durability of Perovskite Solar Cells by Suppressing Dopant Evaporation with Fluoropolymer Coating", ***Solar RRL.*** (2024). (Submitted)

International Conference presentations:

1) **Purev-Ochir B.**, Song J. T., Wang P., Yahiro M., Yamada S., Nakanotani H., Matsushima T., Adachi C., *International Conference on Science and Technology of Synthetic Electronic Materials 2024*, Dresden, Germany (June 23, 2024). (Oral Presentation)

2) **Purev-Ochir B.**, Liu X., Fujita Y., Semba D., Raju T. B., Tumen-Ulzii G., Wachi A., Sato H., Matsushima T., Adachi C., *Asian Conference on Organic Electronic-2023*, Taipei, Taiwan (October 31, 2023). (Poster presentation)

3) **Purev-Ochir B.**, Liu X., Fujita Y., Semba D., Raju T. B., Tumen-Ulzii G., Wachi A., Sato H., Matsushima T., Adachi C., *KJF International Conference on Organic Materials for Electronics and Photonics 2023*, Fukuoka, Japan (August 30, 2023). (Oral presentation) **(Award winning presentation)**

Acknowledgements

First and foremost, I would like to express my deepest gratitude to my supervisor, Professor Chihaya Adachi, for his unwavering support, guidance and encouragement throughout my Ph.D. journey. His invaluable insights, expertise and continuous motivation were instrumental in the completion of this thesis. His constructive critiques and suggestions, which have pushed me to refine my arguments and methodologies. Professor Chihaya Adachi has been more than an advisor; he has been a mentor, a guide, and a source of inspiration. In particular, his inspirational words about the importance of taking risks resonate deeply with me: “Taking risks is challenging, but it can pave the way to a successful future.” This perspective has inspired me to embrace challenges and pursue my goals with confidence. His remarkable dedication, exceptional mentorship, and genuine care for their students have made a lasting impact on my life and career. I am incredibly fortunate to have had the opportunity to work under his mentorship.

I would like to extend my sincere gratitude to my co-supervisor, Associate Professor Toshinori Matsushima. He has provided invaluable support and guidance throughout my research. His meticulous attention to detail and rigorous approach to research have greatly enhanced the quality and depth of my work. From the very beginning of my Ph.D. journey, he guided me meticulously through every step, no matter how small. This careful direction was especially invaluable as a new student embarking on the challenging path of rigorous research. His detailed and thoughtful guidance helped me build a solid foundation and navigate the complexities of my research with confidence. His unwavering support and patience have been a source of great comfort, especially during challenging times. His ability to inspire and motivate has kept me focused and driven. I deeply appreciate his accessibility and willingness to help, whether it was through countless meetings and revisions, late-night emails, or quick, impromptu discussions. I am grateful for the opportunity to have worked with such a distinguished and caring supervisor.

I am also grateful to all the professors at Adachi Lab (OPERA), especially Associate Professor Hajime Nakanotani, whose assistance greatly aided my experiments and measurements. His kind supports and valuable advices have greatly enhanced the quality my work. I extend my gratitude to Associate Professor Youichi Tsuchiya, Associate Professor Fabrice Mathevet, Assistant Professor Kenichi Goushi, Assistant Professor Tang Xun, for their valuable suggestions and inspiring discussions during the meetings and dry runs and for kind supports on my research work. I also would like to express my gratitude to Dr. Sunbin Hwang for his invaluable support in

the thermoelectric measurement and setup. His expertise and assistance significantly streamlined my experimental process, saving me considerable time and effort.

I would like to thank Assistant Professor Jun Tae Song, Dr. Pangpang Wang, Dr. Ganbaatar Tumen-Ulzii, Dr. Telugu Bhim Raju, Dr. Xuelong Liu, Mr. Yuki Fujita, Mr. Dai Semba, Dr. Masayuki Yahiro and Professor Sunao Yamada for their collaboration on my research work.

I also would like to thank all of the members at Adachi lab (OPERA) for their kind support on my life, research and experiments. I am especially grateful to Ms. Sachiko Higashikawa, Ms. Chihiro Hino, Ms. Yuko Kawahara, Ms. Tomoko Nakamura, Ms. Noriko Ooga and Ms. Yoko Hara, for their invaluable assistance not only with my work but also my daily life in Japan. I am also grateful to Ms. Keiko Kusuhara and Mr. Nobuhiro Takeshi for their technical support. Additionally, a special thanks goes to Assistant Professor Kenichi Goushi, Mr. Yuki Fujita and Mr. Kentaro Imaoka for welcoming me at the airport when I first arrived in Japan. Their warm reception made me feel instantly at home in a new country. Their kindness and hospitality were deeply appreciated and helped me settle into my new environment with ease. I am especially appreciated to Mr. Yuki Fujita generously spent plenty of time teaching me every experiment and measurement details from the beginning. His patience, knowledge, and willingness to help were invaluable to me, and I am deeply grateful for his support. Moreover, I am immensely grateful to my batchmates, whose camaraderie and support have been invaluable throughout my academic journey. The shared experiences, discussions, and encouragement from my batchmates have made this journey enjoyable and less challenging.

Furthermore, I would like to thank Ministry of Education, Culture, Sports, Science and Technology (MEXT).

I am profoundly grateful to all of my family members and my precious friends for their continuous support, unconditional love, care and understanding throughout this long journey. My parents, Purev-Ochir Mulduu and Bulgan Dorjnamjim, have been my pillars of strength and motivation. My siblings and friends have always been there to cheer me on.

Thank you all for your unwavering support and belief in me.

Fukuoka
July 2024
Badamgarav Purev-Ochir